Università degli Studi di Torino
Scuola di Dottorato

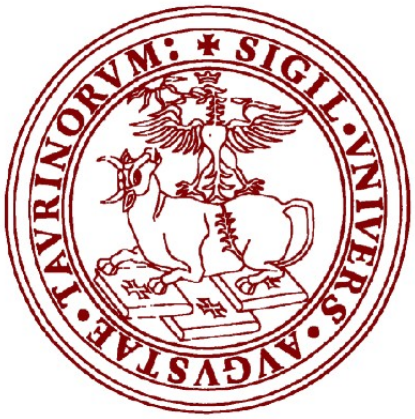

Developing a unified pipeline for large-scale structure data analysis with galaxy number count angular power spectra

Konstantinos TANIDIS

Università degli Studi di Torino
Scuola di Dottorato

Dottorato in Fisica ed Astrofisica

Developing a unified pipeline for large-scale structure data analysis with galaxy number count angular power spectra

Konstantinos TANIDIS

Tutor: Stefano CAMERA

"One, remember to look up at the stars and not down at your feet. Two, never give up work. Work gives you meaning and purpose and life is empty without it. Three, if you are lucky enough to find love, remember it is there and don't throw it away."

Stephen Hawking

UNIVERSITÀ DEGLI STUDI DI TORINO

Abstract

Physics Faculty
Department of Physics

Doctor of Philosophy

Developing a unified pipeline for large-scale structure data analysis with galaxy number count angular power spectra

by Konstantinos TANIDIS

In this PhD thesis, we set forth to develop a cosmological parameter estimation code for (tomographic) angular power spectra analyses of galaxy number counts in Limber approximation and linear scales. We deem this a worthwhile purpose, urged by the consideration that the range of scales and redshifts probed by forthcoming surveys likely calls for a change of paradigm in the treatment of the data and the theoretical modelling. As a starting point we include, for the first time, the full expression for the redshift-space distortions (RSD) correction in the Limber approximation. This allows for a speed-up in computation time, and we emphasise that only angular scales where the Limber approximation is valid are included in our analysis. We show that a correct modelling of RSD is crucial not to bias cosmological parameter estimation. This happens not only for spectroscopy-detected galaxies, but even in the case of galaxy surveys with photometric redshift estimates. Moreover we show that a correct implementation of RSD is especially valuable in alleviating the degeneracy between the amplitude of the underlying matter power spectrum and the galaxy bias. We argue that our findings are particularly relevant for present and planned observational campaigns, such as the Euclid satellite or the Square Kilometre Array, which aim at studying the cosmic large-scale structure and trace its growth over a wide range of redshifts and scales.

Then, we include the weak lensing effect of magnification bias on top of density fluctuations and RSD in our modular parameter estimation code. We thus forecast constraints on the parameters of the concordance cosmological model, dark energy, and modified gravity theories from galaxy clustering tomographic angular power spectra. We find that a correct modelling of magnification is crucial not to bias the parameter estimation, especially in the case of deep galaxy surveys. For this case study we adopt the specifications of the Evolutionary Map of the Universe, which is a full-sky, deep radio-continuum survey, expected to probe the Universe up to redshift $z \sim 6$. We also show that there is a trend for more biased parameter estimates from neglecting magnification when the redshift bins are very wide. We conclude that this result implies a strong dependence on the lensing contribution, which is an integrated effect and becomes dominant when wide redshift bins are considered. Additionally, we note that instead of being considered a contaminant, magnification bias encodes important cosmological information, and its inclusion leads to an alleviation of the degeneracy between the galaxy bias and the amplitude normalisation of the matter fluctuations.

In the last part of the thesis, we apply for first time the multi-tracer technique to angular power spectra with a likelihood-based approach. This goes beyond the usual Fisher matrix formalism hitherto implemented in this kind of analyses, opening up a window for future developments and direct application to available data sets. At the same time, we also release a fully-operational modified version of the publicly available code `CosmoSIS`, where we consistently include all the add-ons presented in the previous works. The result is a modular cosmological parameter estimation suite for galaxy number count angular power spectra, allowing for single and multiple tracers, and including density fluctuations, RSD, and weak lensing magnification. We demonstrate the improvement on parameter constraints enabled by the use of multiple tracers on a multi-tracing analysis of luminous red galaxies and emission line galaxies of the Dark Energy Spectroscopic Instrument. We obtain an enhancement of 44% on the 2σ upper bound of the sum of neutrino masses. The code is publicly available at `https://github.com/ktanidis/Modified_CosmoSIS_for_galaxy_number_count_angular_power_spectra`.

Contents

List of Figures

List of Tables

Chapter 1

Introduction

The establishment of Λ cold dark matter (ΛCDM) as the concordance cosmological model has been led by the unprecedented wealth of data obtained over the past decades. Undoubtedly, precise measurements of the cosmic microwave background (CMB) temperature and polarisation anisotropies (Durrer, 2008; Durrer, 2015; Ade et al., 2014; Ade et al., 2016; Ade et al., 2015) have given profound evidence for the validity of this model. However, several analyses and observations show a certain degree of tension among different data sets (Spergel, Flauger, and Hložek, 2015; Addison et al., 2016; Battye, Charnock, and Moss, 2015; Raveri, 2016; Joudaki et al., 2017a; Joudaki et al., 2017b; Pourtsidou and Tram, 2016; Charnock, Battye, and Moss, 2017; Camera, Martinelli, and Bertacca, 2019). To tackle this issue, and possibly to understand whether these are real hints at the necessity of a change of paradigm in our understanding of the cosmos, a better insight of structure formation and evolution is needed, both on linear and nonlinear scales.

One way to probe the cosmic large-scale structure (LSS) and its growth is by using galaxy catalogues. Galaxy surveys are going to become as powerful as the CMB in constraining cosmological parameters, thanks to the fact that they encode the full three-dimensional (3D) information about the distribution of density fluctuations in the Universe, whereas CMB is ultimately a two-dimensional (2D) surface. Therefore, if we want to study the distribution of galaxies on cosmological scales, we would in principle employ the Fourier-space galaxy power spectrum, $P_{\rm g}(\boldsymbol{k}, z)$(see section 3.8). It is often dubbed '3D' meaning that the wavevector $\boldsymbol{k}$ is the Fourier mode of the 3D separation $\boldsymbol{s} = |\boldsymbol{x}_1 - \boldsymbol{x}_2|$ between a pair of galaxies located at positions $\boldsymbol{x}_1$ and $\boldsymbol{x}_2$, at redshift z. However, to link the galaxy clustering data to the Fourier power spectrum we need to assume a background cosmology. This is due to the fact that what we actually measure is redshifts and angles (or, equivalently, line of sight directions $\hat{\boldsymbol{n}}$), meaning that to translate them to 3D positions $\boldsymbol{x}(z, \hat{\boldsymbol{n}})$ we need to assume a cosmological background. Furthermore, the matter power spectrum is a gauge-dependent quantity, and the arbitrariness on the choice of gauge shows up on the largest scales (Bonvin and Durrer, 2011; Yoo, 2010; Challinor and Lewis, 2011b) . On the contrary, the harmonic-space galaxy angular power spectrum, $C_\ell^{\rm g}$, is a more suitable tool. It represents a natural and gauge-invariant observable for the correlation of galaxy number counts (see e.g. Camera et al., 2018), and it is often referred to as

'2D' because it is a summary statistics for the correlation of two sky maps.

Forthcoming galaxy surveys like those that will be performed at optical/near-infrared wavelengths by the European Space Agency *Euclid* satellite (Laureijs et al., 2011; Amendola et al., 2013; Amendola et al., 2018), or in the radio band by the Square Kilometre Array (SKA) (Maartens et al., 2015; Abdalla et al., 2015; Bacon et al., 2018) will supplement us with information that will push further our knowledge of the Universe. Moreover, synergistic observations at different wavelengths covering large overlapping sky areas will provide us with independent measurements of the clustering and evolution of cosmic structures, thus allowing for valuable cross-correlation studies. This will be a major advantage to tackle systematic effects (see e.g. Camera et al., 2017), and possibly to mitigate cosmic variance (McDonald and Seljak, 2009b; Seljak, 2009; Fonseca et al., 2015). By doing so, multiple probes will achieve high precision and yield strengthened results on the evaluated cosmological model (Weinberg et al., 2013). Finally, let us emphasise that, besides galaxy clustering, other LSS observables like weak lensing cosmic shear can be employed simultaneously to take better advantage of their complementary information, and to lift degeneracies among cosmological parameters.

A starting point in the literature related to such a synergistic approach has been the combination of the galaxy clustering, galaxy-galaxy lensing and cosmic shear (e.g. Bernstein, 2009; Joachimi and Bridle, 2010; Yoo and Seljak, 2012; Mandelbaum et al., 2013; Cacciato et al., 2013; Kwan et al., 2017). Other sophisticated approaches were implemented, e.g. Liu, Ortiz-Vazquez, and Hill (2016) used cross-correlations of CMB lensing with galaxy overdensity and cross-correlations of galaxy overdensity and the shear field to probe the multiplicative bias for CFHTLenS. Such approaches are currently being extensively employed by the Dark Energy Survey Collaboration, (see e.g. Elvin-Poole et al., 2018; Abbott et al., 2018b; Abbott et al., 2018a). Furthermore, there have been thorough theoretical investigations using non-Gaussian covariances between galaxy clustering, weak lensing, galaxy-galaxy lensing, galaxy cluster number counts, galaxy clusters and photometric baryon-acoustic oscillations for photometric galaxies (Eifler et al., 2014; Krause and Eifler, 2017), also with the inclusion of CMB data (Nicola, Refregier, and Amara, 2016; Singh, Mandelbaum, and Brownstein, 2017).

In chapter 2 we describe the Standard Cosmological Model and introduce the basic concepts of modern Cosmology, while in chapter 3 we discuss about the Newtonian perturbation theory, the structure formation and the galaxy clustering probes as well as the correcting effects of the RSD and the weak lensing magnification bias.

The analyses part of the thesis starts with chapter 4 where we present a work that is the first of a series in which we aim to go beyond standard Fisher matrix analyses for the tomographic angular power spectrum of galaxy number counts. There, we focus only on forecasts for single probes using galaxy clustering, and leave multi-tracing for chapter 6. We consider two broad families of galaxy surveys, both of

which are used to probe the cosmic LSS. One of them is represented by the spectroscopic observations, where the redshift of the galaxies is inferred with high accuracy. The other deals with photometric surveys, where galaxies are binned into broad-band redshift slices, due to the large uncertainty in the determination of photometric redshifts. A noteworthy work is that of (Chaves-Montero, Hernández-Monteagudo, and Angulo, 2018) where they studied the effect of photo-z errors on the galaxy number counts using the Fourier-space power spectrum. We, on the other hand, aim to study galaxy number counts by measuring the tomographic angular power spectrum, $C_\ell^g(z_i, z_j)$, in different redshift bins, z_i and z_j. The importance of the tomographic approach in galaxy clustering using the density fluctuations with auto- and cross-spectra between photometric redshift bins, has been studied by (Balaguera-Antolínez et al., 2018) with the 2MPZ catalogue at the local universe. To this purpose, we adopt as proxies of the two aforementioned families of galaxy surveys a *Euclid*-like photometric instrument and the specifications of HI-line galaxy observations with the Phase 1 of the SKA (SKA1). We perform an extensive Bayesian analysis for the two showcases, for which we generate synthetic data including both leading-order Newtonian density fluctuations and the linear-order contribution due to RSD (e.g. Kaiser, 1987a; Szalay, Matsubara, and Landy, 1998). Some original pieces of work which considered a spherical harmonic analysis in redshift-space are (Scharf, Fisher, and Lahav, 1994; Heavens and Taylor, 1995). In particular, we provide the reader with an expression for RSD in Limber approximation (Kaiser, 1987b; LoVerde and Afshordi, 2008). To our knowledge, this is the first in the literature along with that of Chisari et al., 2019 published in the same period. The chapter is organised as follows. In section 4.1 we introduce the tomographic angular power spectrum $C_\ell^g(z_i, z_j)$ with and without RSD (Kaiser, 1987b; Kaiser, 1992), which we implement in the public `CosmoSIS` code (Zuntz et al., 2015) by using today's Fourier-space linear power spectrum $P_{\rm lin}(k)$ provided by `CAMB` (Lewis, Challinor, and Lasenby, 2000). A comparison between our Limber approximated spectra obtained with our modified `CosmoSIS` module and the full solution provided by `CLASS` (Lesgourgues, 2011; Blas, Lesgourgues, and Tram, 2011; Di Dio et al., 2013) is presented in subsection 4.3.1 for different test window functions. In section 4.2 we present the surveys specifications and then in section 4.3, we compare the equi-spaced and equi-populated binning scenarios via Fisher matrices for an idealistic case involving cosmological parameters only. In addition we show the likelihood applied in the final analysis. In section 4.4, we perform the Bayesian forecasting analysis for the same idealistic case and then including real-world nuisance parameters. Throughout this chapter, we assume a fiducial ΛCDM model with the best-fit parameters as of Ade et al. (2016) (see Table 4.2 in section 4.4 for symbols and fiducial values).

Following chapter 4, the work of chapter 5, focuses on one of the SKA precursors, the Evolutionary Map of the Universe (EMU, Norris et al., 2011) radio-continuum survey on the Australian SKA Pathfinder (ASKAP) telescope. Unlike the photometric (optical/near-IR) and the spectroscopic (optical/near-IR or HI-line galaxy survey

in the radio) experiments, radio continuum surveys like EMU have the advantage of being able to scan very quickly large areas of the sky by averaging over all frequencies, thus increasing the signal-to-noise ratio of each source. Despite the fact that the deep and fast scanning in redshift space can detect a large number of galaxies, including also very faint sources, their redshift estimation is quite poor. Given the insufficient redshift information, the angular tomographic clustering is usually adopted to analyse radio continuum galaxy catalogues, instead of the more usual three-dimensional Fourier-space power spectrum.

In this chapter, we move past the Fisher matrix approach hitherto employed, to a full likelihood-based analysis. We particularly turn our interest to the investigation of the cosmological information encoded in the weak lensing effect of magnification bias on the density fluctuations of the galaxy field (see Bartelmann and Schneider, 2001, for a seminal review on gravitational lensing). This effect is widely known and is due to the weak lensing contribution caused by the underlying matter field. It induces a modulation in the clustering signal across redshift bins, inducing a correlation between background and foreground sources.

chapter 5 is outlined as follows. In section 5.1, we introduce the harmonic-space angular power spectrum $C_\ell^g(z_i, z_j)$ with and without the magnification bias correction, and implement it in the publicly available `CosmoSIS` code (Zuntz et al., 2015). In section 5.2, we present the EMU survey specifications and simulation results used to construct the tomographic redshift bins that will be later applied in the analysis. In subsection 5.4.1, we perform a comparison test between our Limber approximated `CosmoSIS` code version and the full solution obtained with `CLASS` (Lesgourgues, 2011; Blas, Lesgourgues, and Tram, 2011; Di Dio et al., 2013). In section 5.3, we present the theoretical models considered, while the likelihood for the forecast is presented in section 5.4. In section 5.5, we examine in detail the Bayesian analysis of an idealistic and two realistic scenarios for the cosmological models considered, and we also show that the redshift-space distortions (RSD) correction to the density field has negligible effect in our case.

Finally in chapter 6 we implement the multi-tracer technique with the Dark Energy Spectroscopic Instrument (DESI, Aghamousa et al., 2016) to constrain neutrino masses. Concerning the Cosmic neutrinos, they are the most abundant particles in the Universe after photons, yet little is known about their mass and energy budget contribution today. Nonetheless, it has been detected with high significance, that there are three neutrino species each having a radiation number density contribution $\approx 112/\text{cm}^3$ in the early Universe and a temperature around $\approx 1.6 \cdot 10^{-4}\text{eV}$ (Ade et al., 2016). In addition to this, the neutrino oscillation measurements have shown that there are at least two massive out of the three neutrino mass eigenstates, contrary to the Standard Model of Particle Physics describing them as as fundamental but massless particles, and therefore suggesting that there is evidence for physics beyond the Standard Model.

It is also known that neutrino oscillation measurements provide us not with

the individual neutrino masses, but rather with the two squared mass splittings: the solar splitting with $\Delta m^2_{12} \approx 7.6 \cdot 10^{-4}$ eV and the atmospheric splitting with $|\Delta m^2_{13}| \approx 2.5 \cdot 10^{-3}$ eV (Gonzalez-Garcia, Maltoni, and Schwetz, 2016; Capozzi et al., 2016; Esteban et al., 2017; Capozzi et al., 2017; Salas et al., 2018b). Given the sign uncertainty in the atmospheric splitting we can have a *normal* hierarchy with $\Delta m^2_{13} > 0$ and $m_1 \geq 0$ eV, $m_2 \geq 0.0087$ eV and $m_3 \geq 0.049$ eV the three mass eigenstates, or an *inverted* hierarchy for $\Delta m^2_{13} < 0$ and $m_1 \geq 0.049$ eV, $m_2 \geq 0.05$ eV, $m_3 \geq 0$ eV. In case one of the three eigenstates is ≥ 0.1eV then $m_1 \approx m_2 \approx m_3$ and we have a quasidegenerate hierarchy. The relic neutrino density along with the oscillation data provide a lower limit on the sum of the neutrino species which is $\sum m_\nu \geq 0.06$eV for *normal* hierarchy and ≥ 0.1eV for *inverted*, whilst the upper limit provided by the latest cosmological data suggests that is $\sum m_\nu \leq 0.15$eV at 95% confidence level (Ade et al., 2016; Capozzi et al., 2016).

With the forthcoming experimental campaigns aimed at scrutinising the large-scale structure of the Universe, such as the aforementioned *Euclid* satellite, the SKA, the Rubin Observatory (formerly Large Synoptic Survey Telescope, LSST) (LSST Science Collaboration et al., 2009), or the Dark Enery Spectroscopic Instrument (DESI) (Aghamousa et al., 2016), we will be able to put constraints on the neutrino mass at the 3-4σ level, possibly ruling out the *inverted* hierarchy (Blennow, 2014; Hannestad and Schwetz, 2016; Vagnozzi et al., 2017; Simpson et al., 2017; Gerbino et al., 2017; Salas et al., 2018a; Long et al., 2018).

Generally, the presence of massive neutrinos affects the total matter fraction in the Universe in the sense that the linear growth of the matter fluctuations is suppressed for scales $k > k_{\rm fs}$ where $k_{\rm fs}$ the neutrinos free streaming scale (Lesgourgues and Pastor, 2006). This effect can be studied with lensing of the cosmic microwave background (CMB), the clustering of galaxies and other biased tracers of the large scale structure, and the weak lensing effect of cosmic shear, thus putting constraints on the (sum of) neutrino mass(es) (Hu, Eisenstein, and Tegmark, 1998).

Another consequence of the presence of massive neutrinos is a scale dependence induced on the linear growth rate of cosmic structures and on the galaxy bias (LoVerde, 2014; Font-Ribera et al., 2014; Upadhye et al., 2016). These quantities, unlike the matter power spectrum, are not dependent on a specific realisation of the density perturbation field and therefore are not affected by the cosmic variance (Seljak, 2009; McDonald and Seljak, 2009a; Bernstein and Cai, 2011). Thus, we can decrease the measured error on these quantities by increasing the number of tracers. With the so-called 'multi-tracer' technique, one considers two or more different galaxy populations—which are not independent by definition, since they both trace the same underlying dark matter field, but with different biases (Guzzo et al., 1997; Benoist et al., 1996). By multi-tracing, we effectively measure the ratio of the two biases (see e.g. Witzemann et al., 2019), net of the stochastic nature of the power spectrum. This is also true for the growth rate. As a result, an analysis employing

consistently multiple tracers can yield improved constraints on the sum of the neutrino masses, compared to a single tracer, due to the more precise measurements on the cosmic variance free quantities of the galaxy bias and the growth rate of structures via redshift-space distortions (RSD) (e.g. Kaiser, 1987a; Szalay, Matsubara, and Landy, 1998).

chapter 6 is summarised as follows. In section 6.1, we describe the Limber approximated angular power spectra in the case of multi-tracing and define the RSD and magnification bias scale dependent corrections. In section 6.2, we present our benchmark survey specifications, namely the spectroscopic survey DESI. In section 6.3, we review the massive neutrinos effect on the linear galaxy bias. Then, in section 6.4 we show the likelihood used for the forecast as well as the multipole cuts applied in our analysis. Lastly, the results are presented in section 6.5. The modified publicly available code is described in section D.1.

In chapter 7 we discuss the drawn conclusions of the results presented in this PhD thesis.

Chapter 2

The Standard Cosmological Model

Cosmology is the area of physics that concerns the modelling, evolution and the large-scale structure of the Universe at scales beyond our Galaxy. At these scales and on a background level a spatial isotropy (the so called *Copernican Principle*) and homogeneity is observed throughout its history, with the *Cosmic Microwave Background* (hereafter CMB) measurements (Ade et al., 2016; Hinshaw et al., 2012; Mather et al., 1994) at the early Universe and with the galaxies distribution (Marinoni, Bel, and Buzzi, 2012; Abazajian et al., 2009) at the late times. This assumption is the *Cosmological Principle* and constitutes one of the most important Modern Cosmology pillars. Along with this Principle and the assumption that General Relativity (hereafter GR) holds true at all scales, cosmologists have built the *Standard Cosmological Model*. We can summarize those two core elements of the Model:

- **Copernican Principle:** The widely accepted Standard Model implicitly agrees with the assumption that there is no such a special spot in the Universe for Earth to occupy. Beyond a doubt, one would need to test this further by making observations at several different positions in the Universe, though some tests could be done in order to check the consistency of the models supporting it. New tests propose that there is supporting evidence in favor of the homogeneity, consistently showing that this statement is valid beyond the scales of 100Mpc (Ntelis et al., 2017; Laurent et al., 2016; Sarkar et al., 2009). On the contrary, it is important to note that this accelerated Hubble expansion that we observe, could be explained if Earth is placed in an advantaged position. This could be the center of a large local under-density (February et al., 2010).

- **GR is valid at all scales:** The next basic assumption for the Standard Model is that GR holds true at a variety of scales. GR has successfully been tested within our Solar System at the order of $\approx 10^{-4}$pc, while the galaxy supercluster Laniakea, which our Galaxy is part of, at the scale of $\approx 10^{8}$pc. Considering the cosmological scales, one should account for a 12 order of magnitude gap, in order to test GR. Under this supposition, we describe the gravity as geometrical, where a metric tensor characterizes the spacetime. One should know that there is an ongoing development of non-geometrical descriptions (Milgrom, 2015; Verlinde, 2011), although the geometric one fairs well in being theoretically complex and explaining a plethora of phenomena at the same time.

We will hereafter elaborate these ideas in a mathematical framework.

2.1 The Hubble Expansion

With the term "Expanding Universe" we mean that the distance between us and the distant background galaxies is larger than that at the early times. This cosmological recession can be described with the scale factor $a = a(t)$. At present time t_0 we have $a_0 = a(t = t_0) = 1$ and at any earlier time $t < t_0$, $a(t) < 1$. We should note that in this thesis the subscript 0 corresponds to the present time unless otherwise stated. The physical distance in the units of the scale factor, is defined as the *comoving distance*. This means that two points at rest in the expanding universe always have the same comoving distance between them during the evolution of the Universe. Nonetheless, the physical distance being proportional to the scale factor changes in time. Given that, we can set a reference frame in which an observer at rest has coordinates that never vary in the Universe's history. This is the *Comoving frame* where we measure the distance between two points with the comoving distance (for more details see section 2.8). Thus, at rest, an observer has varying physical coordinates with the scale factor a, and constant comoving coordinates.

We can describe the spacetime geometry with three cases. *Flat*, *closed* or *open* Universe (see Figure 2.2). The *flat* Universe is also called Euclidean, in which if two particles begin to travel parallely, they shall remain as such unless/until an external interaction occurs. In a closed (open) Universe, on the other hand, these moving particles will converge (diverge) after a certain point, even if they initially move parallely. Those three cases, correspond to a null, positive or negative curvature value, respectively. As we will see in section 2.4, in GR the spacetime geometrical properties are closely related to the energy density: We have a flat Universe with null curvature if the energy density is equal with the total critical density. There is substantial observational evidence (Aghanim et al., 2020) suggesting that our Universe is flat (or approximately flat).

In order to examine the history of the expansion of the Universe, one is necessary to know the time evolution of the scale factor $a(t)$. This dependency is given by the *Hubble factor* that reads:

$$H(t) = \frac{\dot{a}}{a}, \tag{2.1}$$

where $\dot{()} = d/dt$ denotes the derivative with respect to time. Another important quantity which is closely related to the total critical energy density that will be discussed in section 2.4, is the Hubble constant which is the present value of the Hubble factor: $H_0 = H(t_0)$. Consider having two observers at rest in a comoving frame. The velocity with which they are moving away from one another depends on the varying scale factor. For the local Universe (or equivalently at low redshift (definition in

Equation 2.10)) the *Hubble Law* relates the observers' relative recessional velocity v and physical distance between them d such that:

$$v = H_0 d, \tag{2.2}$$

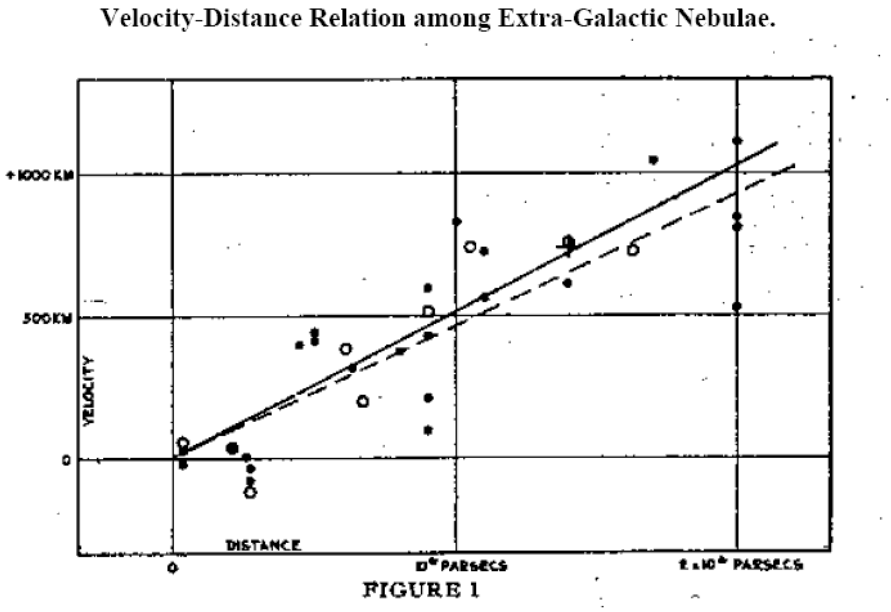

FIGURE 2.1: The original plot of Hubble showing the velocity-distance relation of galaxies. The radial velocities accounting for solar motion are shown as a function of distances calculated for incorporated stars and nebulae's mean luminosities in a cluster. The filled dots and the solid line represent the solar motion solution considering each nebulae separately. The solution after combining the nebulae in groups is presented with empty dots and the dashed line. The cross shows the mean velocity - mean distance relation for 22 nebulae that could not have their individual distances estimated.

where the constant H_0 is found $67.3\,\mathrm{Km\,s^{-1}Mpc^{-1}}$ (Ade et al., 2016). Cosmologists often use the dimensionless Hubble constant which is $h = 0.67$ where $h = H_0/100\,\mathrm{Km\,s^{-1}Mpc^{-1}}$.

2.2 The metric and Friedmann Equations

For the derivation of the Fridmann equations here we assume that the speed of light is $c = 1$. The core of the Standard Cosmological Model starts from the *Einstein equations*:

$$G_{\alpha\beta} = 8\pi G T_{\alpha\beta}. \tag{2.3}$$

The quantity $G_{\alpha\beta}$ is the Einstein tensor while $T_{\alpha\beta}$ is the stress-energy tensor corresponding to the matter and energy distribution and G the gravitational constant.

Equation 2.3 tells us that the geometry of the spacetime (on the left side) strongly relates with this distribution (on the right side). Also:

$$G_{\alpha\beta} = R_{\alpha\beta} - \frac{1}{2} g_{\alpha\beta} R, \tag{2.4}$$

where the quantity $R_{\alpha\beta}$ is the Ricci tensor, $g_{\alpha\beta}$ the metric of the spacetime, and the Ricci scalar $R = R_{\alpha\beta} g^{\alpha\beta}$ stands for the curvature. Given a perfect fluid with stress-energy tensor:

$$T_{\alpha\beta} = \rho v_\alpha v_\beta + P(g_{\alpha\beta} + v_\alpha v_\beta), \tag{2.5}$$

where ρ the density, P the pressure and v_α the four-velocity of the fluid, the following conservation law holds (Wald, 1984):

$$\nabla^\alpha T_{\alpha\beta} = 0, \tag{2.6}$$

representing the continuity and Euler equations (dynamics of classical fluids) in the relativistic extension (for the derivation in the Newtonian regime see chapter 3). One special case of the analytical solutions of the Einstein equation is of cosmological importance. The geometrical metric assuming isotropy and homogeneity takes the form:

$$ds^2 = -dt^2 + a^2(t) \left[\frac{dr^2}{1 - Kr^2} + r^2 (d\theta^2 + \sin^2 \theta d\phi^2) \right], \tag{2.7}$$

which is called Friedmann-Robertson-Walker metric (FRW). The quantity t is the cosmic time, while r, θ, ϕ are the spatial comoving coordinates. The spatial curvature denoted with K as explained in section 2.1, takes the values $0, 1, -1$ for flat (Euclidean), spherical (closed) or hyperbolic (open) geometry. If we substitute 2.7 into Equation 2.3, we obtain the *Friedmann equations*

$$\left(\frac{\dot{a}}{a} \right)^2 = \frac{8\pi G}{3} \rho - \frac{K}{a^2}, \tag{2.8}$$

$$\frac{\ddot{a}}{a} = -\frac{4\pi G}{3} (\rho + 3P). \tag{2.9}$$

In the introduction of chapter 2, we explained the terms of homogeneity and isotropy. It is actually true that the universe is not homogeneous and isotropic, otherwise we would not be able to observe the structures in the Universe, such as voids, filaments, clusters and galaxies. However, we can safely adopt this approximation on a background level when we consider scales above some hundreds of Mpc. Under this assumption the stress-energy tensor corresponds to the perfect fluid case. Furthermore, the above equations can be simplified if we introduce the equation of state parameter $w = P/\rho$ for all the fluid components in the Universe: $w = 0$ for non relativistic dark matter, $w = 1/3$ for radiation, and $w = -1$ for cosmological constant. It is important to note that from Equation 2.9, the Universe in no case can

be static but is free to contract or expand, since the assumption for $\rho > 0$, and $P \geq 0$ always ensures $\ddot{\alpha} \neq 0$.

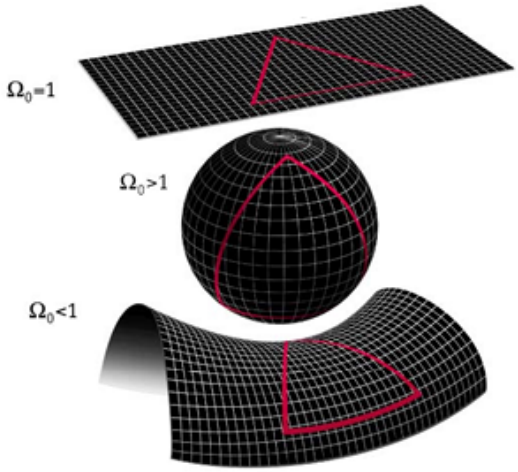

FIGURE 2.2: Here are presented the three possible scenarios a universe could experience as described by the FRW metric. Notably, depending on the curvatures $0, 1, -1$ we can have a flat (plane), a positively curved (spherical) or a negatively curved (hyperbolic) universe. With Ω_0 we denote the total fractional density parameter as presented in Equation 2.17 **(image on http://www.relativitycalculator.com/glossary.shtml)**

It wasn't until Hubble discovered that the Universe is expanding and therefore each galaxy recedes from us and each other. At this point, it is noteworthy that Equation 2.2 can be recovered by the Friedmann equations. In detail, he could not estimate this velocity directly, but he rather measured the Doppler shift in the objects' spectral lines due to the growing scale factor. This displacement is the *cosmological redshift*. This quantity is defined as:

$$z = \frac{\lambda_0}{\lambda} - 1 = \frac{\alpha(t_0)}{\alpha(t)} - 1, \tag{2.10}$$

where t_0 is observer's cosmic time, λ and λ_0 is the radiation wavelength traveling from the sources and the rest frame measurement respectively. By Taylor expanding Equation 2.10 around $(t_0 - t)$ up to second order we obtain:

$$z = H_0(t - t_0) + \left(1 + \frac{q_0}{2}{H_0}^2\right)(t_0 - t)^2 + \mathcal{O}(t_0 - t)^2, \tag{2.11}$$

where q_0 is the rest frame value of the deceleration parameter defined as:

$$q = -\frac{1}{H^2}\frac{\ddot{\alpha}}{\alpha}. \tag{2.12}$$

If we multiply with the speed of light c the linear term of Equation 2.11 assuming $z << 1$ we can recover again Equation 2.2.

2.3 Different species domination eras

As we look back in time, the Universe becomes smaller, denser and hotter. The cosmos as we know it described by the spacetime metric is the outcome of the huge explosion named "Big Bang". Nothing can be said for the singularity at the initial moment $t = 0s$ of the explosion since any physics occurring before $t_{Planck} < 10^{-43}s$ needs for a satisfactory unified quantum-gravity theory which is yet to be found. Despite the inaccessibility in the physical phenomena taking place in the newborn Universe, we can still extract useful pieces of information about the cosmic evolution working with Friedmann equations. After a few manipulations one can obtain the first law of thermodynamics analogue:

$$\frac{d}{dt}(\rho a^3) + P\frac{d}{dt}a^3 = 0. \tag{2.13}$$

If we consider an equation of state parameter for radiation with $P = \rho/3$ we have:

$$\rho \propto a^{-4}, \tag{2.14}$$

while for matter $P = 0$:

$$\rho \propto a^{-3}, \tag{2.15}$$

and for dark energy $P = -\rho$:

$$\rho = \text{constant}. \tag{2.16}$$

This means that matter density decreases slower than the radiation density, while the dark energy density remains constant throughout the cosmic history. Thus, it is evident that the cosmic history is divided into three fundamental eras: radiation, matter and dark energy epoch, starting from the early towards the late Universe (Figure 2.3). It is radiation dominated until $t \approx 5 \cdot 10^4$yr after the "Big Bang" when its energy density reached that of matter at $z_{eq} \approx 3600$. The next period is that of the non relativistic matter domination which is responsible for the formation of structures. This lasted until $a = 0.75$ corresponding to $t = 9.8Gyr$ where the dark energy epoch started.

2.4 Fractional densities of the hypothetical fluids

In order to understand the geometry of the Universe, it is clear that the ρ quantity from Equation 2.8 plays an important role to investigate this. We define the total *fractional density parameter* today as:

$$\Omega_0 = \frac{\rho_0}{\rho_c}, \tag{2.17}$$

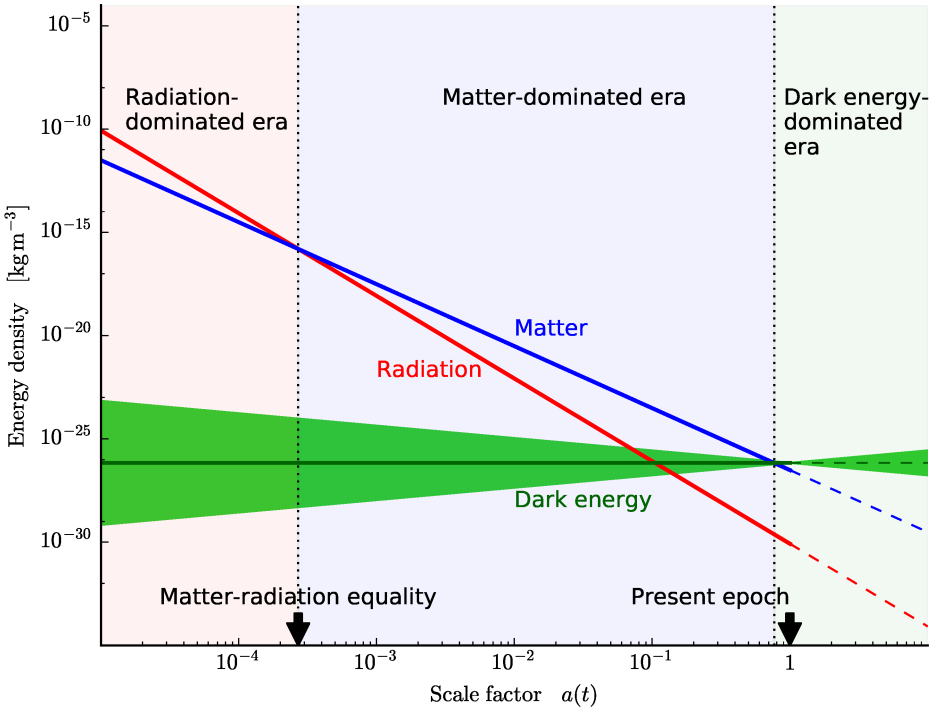

FIGURE 2.3: This figure presents how the radiation (red), matter (blue), and dark energy (green) densities evolve with the scale factor. Plot taken from Debono and Smoot, 2016

where ρ_0 is the present density and

$$\rho_c = \frac{3{H_0}^2}{8\pi G}, \tag{2.18}$$

the *critical density* corresponding to a flat Universe with $K = 0$. In detail, the spacetime is flat for $\Omega_0 = 1$, spherical for $\Omega_0 < 1$ and hyperbolic for $\Omega_0 > 1$ (see again Figure 2.2). The closed scenario implies that the expansion of the Universe would have a turnaround process leading to the "Big Crunch", while the open scenario along with an equation of state parameter $w < -1$ would eventually tear apart the spacetime causing the " Big Rip ".

2.5 The cosmological constant problem

The groundbreaking evidence for the accelerated expansion of the Universe came with the SNIa data analysis by Riess et al., 1998 and Perlmutter et al., 1998 (see section 2.9 for details). In addition, the CMB measurements (Ade et al., 2016) as we will see in section 2.6 suggest that depending on the main peak position (bottom panel of Figure 2.5), the total fractional density is $\Omega_0 \approx 1$. Nonetheless, the matter contribution is found to be only 0.3 and is not enough to account for the flat universe requirement. There should exist an additional component which is the *dark energy* (hereafter DE) to solve the issue. The simplest hypothesis is that this fluid component can be described by a constant term Λ added to the stress-energy tensor:

$$G_{\alpha\beta} = 8\pi G T_{\alpha\beta} - \Lambda g_{\alpha\beta}, \tag{2.19}$$

and the Friedmann equations now read:

$$\left(\frac{\dot{\alpha}}{\alpha}\right)^2 = \frac{8\pi G}{3}\rho - \frac{K}{\alpha^2} + \frac{\Lambda}{3}, \tag{2.20}$$

$$\frac{\ddot{\alpha}}{\alpha} = -\frac{4\pi G}{3}(\rho + 3P) + \frac{\Lambda}{3}. \tag{2.21}$$

Now it is pretty clear that for a given density ρ and pressure P there is $\Lambda > 0$ such that the Universe accelerates with $\ddot{\alpha} > 0$. There are many of a model for the description of DE with that of the cosmological constant with the equation of state parameter $w_{DE} = -1$ being the simplest of all. The physical meaning of Λ is that some form of vacuum energy fills naturally the expanding space, and since it has constant energy density, after a certain point (see again section 2.3) it surpasses the matter. According to the quantum field theory, these are the vacuum fluctuations with a contribution of the order of $\rho_{vac} \approx 2 \cdot 10^{110}$ erg $\cdot$ cm $^{-3}$, while the cosmological observations suggest a value $\rho_\Lambda \approx 2 \cdot 10^{-10}$ erg $\cdot$ cm $^{-3}$. This huge-120 order of magnitude-gap is yet to be explained. We can now rewrite Equation 2.20 in the form of fractional densities for all the components:

$$[H(z)/H_0]^2 = \Omega_m(1+z)^3 + \Omega_\gamma(1+z)^4 + \Omega_k(1+z)^2 + \Omega_\Lambda e^{3\int_0^z \frac{1+w_{DE}(z')}{1+z'}dz'}, \tag{2.22}$$

where all the component fractional densities:

$$1 = \frac{8\pi G}{3H^2}(\rho_m + \rho_\gamma + \rho_K + \rho_\Lambda) = \sum_i \Omega_i, \tag{2.23}$$

with Ω_m the non relativistic matter density parameter including baryons, Ω_γ the radiation and relativistic matter density (neutrinos or "hot" dark matter), Ω_Λ the DE density parameter and Ω_K the curvature density. For Euclidean (flat) Universe $\Omega_K = 0$, while for closed is negative and for open positive. In the case of cosmological constant the general non-static term for the dark energy equation of state becomes simply $w_{DE}(z) = w_{DE} = -1$.

Current measurements from Ade et al., 2016 show that $\Omega_b \approx 0.05$, leaving the rest 25% dominant gravitational component to be some form of unknown *dark matter* (hereafter DM). DM lacks any kind of electromagnetic emission and its nature can either be particle or just a modification of gravity that could provide insight about the dark sector (including DM and DE).

TABLE 2.1: The Ade et al., 2016 results for the cosmological parameters suggest that the Universe is described very well by the flat ΛCDM model (cosmological constant and cold dark matter)

Parameter	Best fit ($\pm 1\sigma$)
$\Omega_b h^2$	0.02222 ± 0.00023
$\Omega_c h^2$	0.1197 ± 0.0022
H_0	67.3 ± 1.2
Ω_Λ	0.685 ± 0.013
Ω_m	0.315 ± 0.013

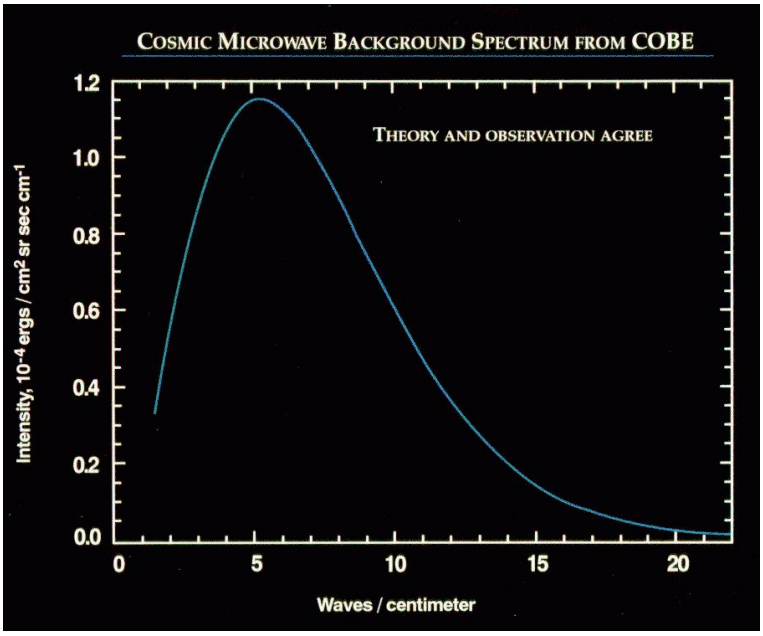

FIGURE 2.4: The theoretical prediction of the blackbody spectrum and the COBE observations (Mather et al., 1994). The measured errorbars are smaller than the thickness of the theoretical solid curve

2.6 CMB

Another important time in cosmic history, is that of *recombination* when the Universe was only 380000*yrs* ($z_{rec} \approx 1100$), in which radiation and matter decouple. Before that time, electrons and protons cannot form hydrogen atoms due to the constant scattering with the high energetic interacting photons. As the scale factor grows, so does the radiation wavelength, and eventually photons are allowed to travel long paths freely making the primordial Universe transparent. Those fossil photons are imprinted on the *Cosmic Microwave Background* (hereafter CMB), discovered back in 1965 by Penzias and Wilson, later providing us with unprecedented insights into the fundamental cosmology. There are three full-sky satellite experiments exclusively dedicated to the CMB. First, the launch of NASA's experiment, named *COsmic Background Explorer (COBE)* in 1989 (Mather et al., 1994), then the *Wilkinson Microwave Anisotropy Probe (WMAP)* in 2001 (Bennett et al., 2003) and more recently the

ESA's *Planck* in 2009 (The Planck Collaboration, 2006). COBE with angular resolution of 2^o, measured the temperature fluctuations $T = 2.728 \pm 0.002K$, and pointed out the blackbody spectrum nature of the CMB whose observational errorbars are way smaller than the thickness of the theoretical curve (see Figure 2.4). WMAP worked with better angular resolution targeting the CMB acoustic oscillations. The breakthrough precision measurements regarding resolution (3 times higher than the WMAP) and sensitivity (5 times higher than the WMAP) came with Planck, providing the cleanest maps of the CMB as of today.

By looking at the CMB, it is sensible to wonder about the origin of these temperature perturbations in the full sky. Now we know that these are the result of the initial density field perturbations. The temperature perturbations read:

$$\frac{\delta T}{T} = \frac{T - \bar{T}}{\bar{T}}, \tag{2.24}$$

where $\bar{T}$ is the mean temperature and $T = T(\hat{n})$ is a specific temperature measurement at the sky position (θ, ϕ).

We can also expand these fluctuations in spherical harmonics as:

$$\frac{\delta T}{T} = \sum_{\ell}^{\infty} \sum_{m=-\ell}^{\ell} g_{\ell m}(z_{CMB}) Y_{\ell m}(\hat{\mathbf{n}}), \tag{2.25}$$

with $Y_{\ell m}$ the Laplace spherical harmonics and $g_{\ell m}$ the harmonic coefficients. The perturbations can be quantified by introducing the temperature angular power spectrum. We can do this since the temperature CMB map can be assumed as a realization of a stochastic field (the same can be also applied for the density field as we will see in section 3.14). Thus we define:

$$C_\ell = \sqrt{\langle |g_{\ell m}|^2 \rangle}, \tag{2.26}$$

where with $\langle\rangle$ we denote the ensemble average. The bottom panel of Figure 2.5 presents the temperature angular power spectrum as a function of multipoles ℓ measured by the Planck satellite. It is clearly seen that the observational points agree very well with the ΛCDM model. We can summarize the main results for the CMB synergies as the following:

- The Universe can be considered isotropic at a remarkable extent, an observation that is consistent with the Standard Cosmological Model. The temperature fluctuations (of the order of $\delta T/T \approx 10^{-5}$) are quite small, yet able to provide useful pieces of information about the primordial density anisotropies from which all the structures stemmed.

- Yield strict constraints on the cosmological parameters (see Table 2.1). The detection of the peaks determines the values of the cosmological parameters, and in detail, with the ratio between the first-third peak and the second-forth peak, and the space between we can estimate the baryon and total matter density

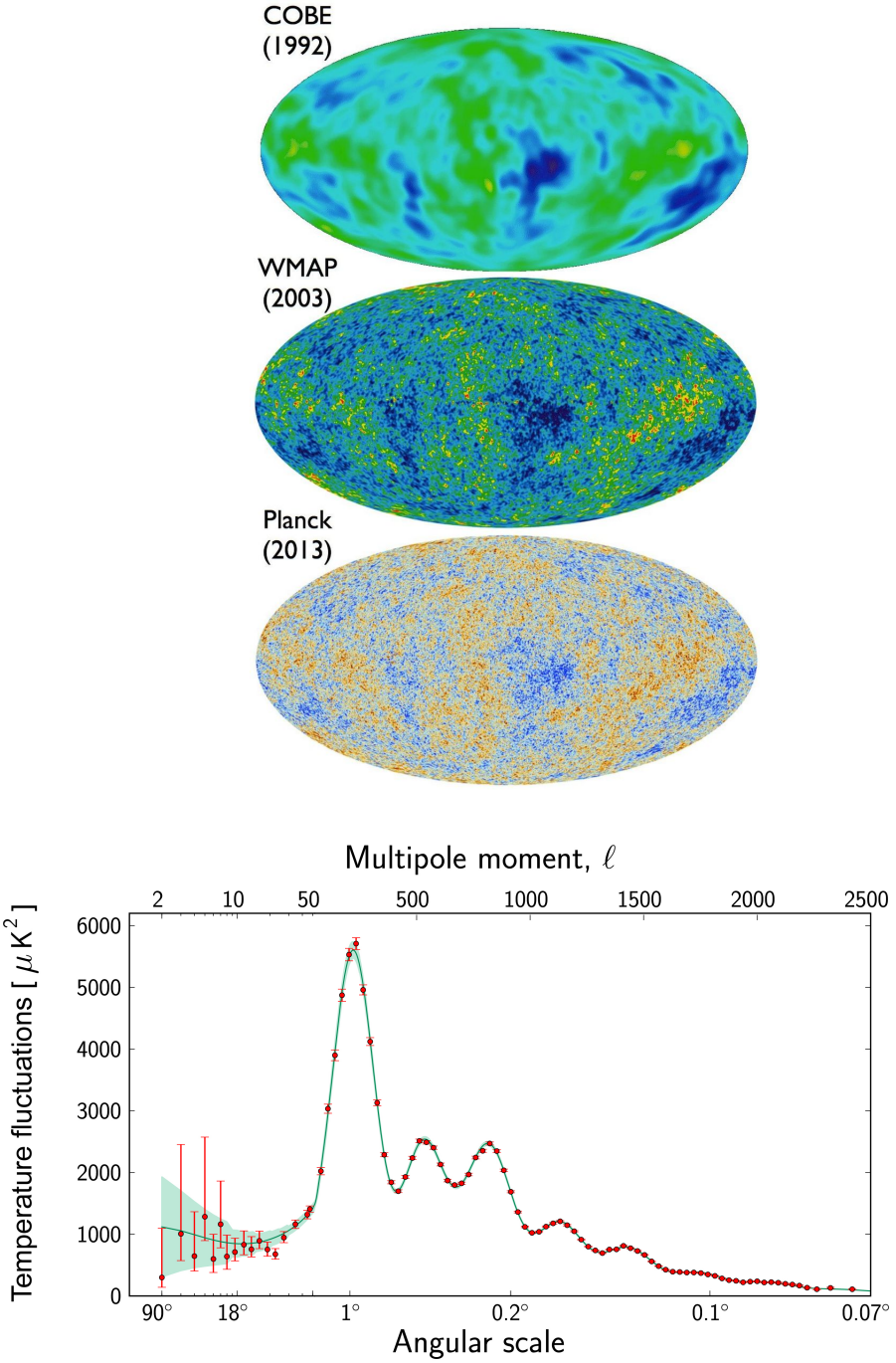

FIGURE 2.5: Top: In this plot we see how the CMB experiments measured the fluctuation in temperature corresponding to the primordial seeds of the density perturbations with progressively better angular resolution. Bottom: Here we see with the red points the CMB temperature anisotropy angular power spectrum measurements as a function of multipoles (angular separation). The blue solid line is the ΛCDM theory best fit (see Table 2.1). We should note that the cosmic variance (for details see section 3.6) becomes important at large scales where the errorbars are larger

2.7 Inflation

Despite having been in exceptional agreement with the observational data, the Standard Cosmological Model has been, as of today, insufficient to provide a solution to a number of problems stemming from the current observations. These issues concern the fine tuning that should be impose on the initial conditions of the Universe in order to explain what is measured.

- **Flateness:** As we saw in the previous section the evidence from Ade et al., 2016 suggest that the Universe is flat having a fractional density $\Omega_{tot} = 1$ within a few percent accuracy. Going back in time the constraints on the unity become even stronger. For instance, at Planck time $t_{Planck} \approx 10^{-44}s$ the relation reads $|1 - \Omega_{t_{Planck}}| \leq 10^{-60}$ rendering a coincidence highly unlikely. This flattening of the Universe warrants for a physical process acting on the early ages.

- **Horizon:** This is the problem of the observed homogeneity and isotropy of the Universe. The CMB experiments have shown that the amplitude of the temperature fluctuations are only $\approx 10^{-5}$ and hard to be explained by the "Big Bang" scenario since the gravitational expansion gives no time for the system to reach thermal equilibrium. Also, the horizon size at the time of recombination is half of the angular separation of two anti diametric points at the last scattering surface. As a result, those two regions receding from each other with speed greater than the speed of light, cannot have been in casual contact. This is quite puzzling considering that the separation of two points by a horizon distance at the time of recombination is $\approx 2^o$ and at the same time the Ade et al., 2016 measurements show that above that distance the temperature perturbations are very small. Given the no light interactions among those regions this temperature homogeneity is not explainable.

- **Magnetic monopoles:** Accepting the "Big Bang" theory would also mean that there should have been massively produced, heavy and stable primordial magnetic monopoles which ought to have persisted until the present day. Nonetheless, these relic magnetic fields are yet to be found setting quite stringent constraints on their density.

The inflationary solution proposed in the 1980s is the most successful theoretical paradigm developed to overcome the problems of the ΛCDM model (for a review in inflation see Liddle, 1999). Apart form the late cosmological expansion dominated by the DE, it has been proposed that the Universe at the very early stages of its history underwent another outward accelerated space-time expansion dominated by a cosmological constant Λ_I. This phase lasted from the time $10^{-36}s$ to roughly the time 10^{-33} or $10^{-32}s$ after the "Big Bang". After that time, the Universe continued to expand but at a slower accelerated rate. Similarly to the late time DE, the origin of this mechanism is unknown, although its existence is supported after it has successfully

made predictions which were later confirmed by observations. It is true that the observed Universe is only a small part of the enormous unobserved Universe, and the frontier between them is the well-known cosmological horizon. Equation 2.20 can be written down for inflation as:

$$\left(\frac{\dot{\alpha}}{\alpha}\right)^2 = \frac{\Lambda_I}{3}. \tag{2.27}$$

The evolution of the scale factor for an inflationary period starting at a time t_α and lasting until t_β is:

$$\alpha(t) = \begin{cases} \alpha_\alpha (t/t_\alpha)^{1/2} & \text{if} \quad t < t_\alpha \\ \alpha_\alpha e^{[H_I(t-t_\alpha)]} & \text{if} \quad t_\alpha < t < t_\beta \\ \alpha_\alpha e^{[H_I(t_\beta - t_\alpha)]} (t/t_\beta)^{1/2} & \text{if} \quad t > t_\beta \end{cases}, \tag{2.28}$$

with $H_I = \left(\frac{\Lambda_I}{3}\right)^{1/2}$ the Hubble constant at the time of the inflationary period, in which the resulting scale factor grew by:

$$\frac{\alpha_\beta}{\alpha_\alpha} = e^{[H_I(t_\beta - t_\alpha)]} \tag{2.29}$$

In case the inflation lasts long and is comparable with the Hubble time $1/H_I$, the expansion is sudden and the cosmological horizon remains unchanged. This exponential expansion results in separating two nearby regions very rapidly and their distance finally exceeds the horizon size. The space-time starts a less accelerated expansion when the inflationary field gradually goes to vacuum and the cosmological constant becomes zero. At this stage, the new areas that come into contact now are the same that were pushed far beyond the horizon at the time of the inflation giving a substantial explanation for the observed homogeneity of the temperature. Given that the total fraction density becomes:

$$|1 - \Omega(t)| \propto e^{(-2H_I t)}, \tag{2.30}$$

yielding a nearly flat curvature produced by an abrupt stretching of the space-time even if the duration of the inflation is short. The absence of the strong magnetic monopoles could be explained by supposing that the energy density of the particles describing them at the time of the inflation is diluted and drops to values that cannot be currently observed.

There has been a variety of mechanisms for the inflation. The most widely accepted scenario is the following. We can postulate that there exists a scalar field $\phi(\vec{r}, t)$ with potential $V(\phi)$ and the perfect fluid stress-energy tensor form $\rho = \dot{\phi}^2/2 + V(\phi)$ and $P = \dot{\phi}^2/2 - V(\phi)$. If V_0 is the plateau potential as shown in Figure 2.6 and the inflationary field is pushed from $\phi_\alpha = 0$ to $\phi = d\phi$, it starts slowly to roll down until the end of the inflation ϕ_β and then rapidly proceed to a meta-stable potential until reaching and oscillating around the $\phi = \phi_0$ minimum. At this point the inflationary field starts to interact with other fields and cause the reheating (where

vacuum energy decays into some particle content). It is during the times ϕ_α-ϕ_β transition when inflation freely occurs and the space-time expands exponentially. The expansion then turns to a normal power-law expansion at the time in which the minimum is reached. Given that the plateau of the curve is quite flat and the equation of state parameter w can take the form of

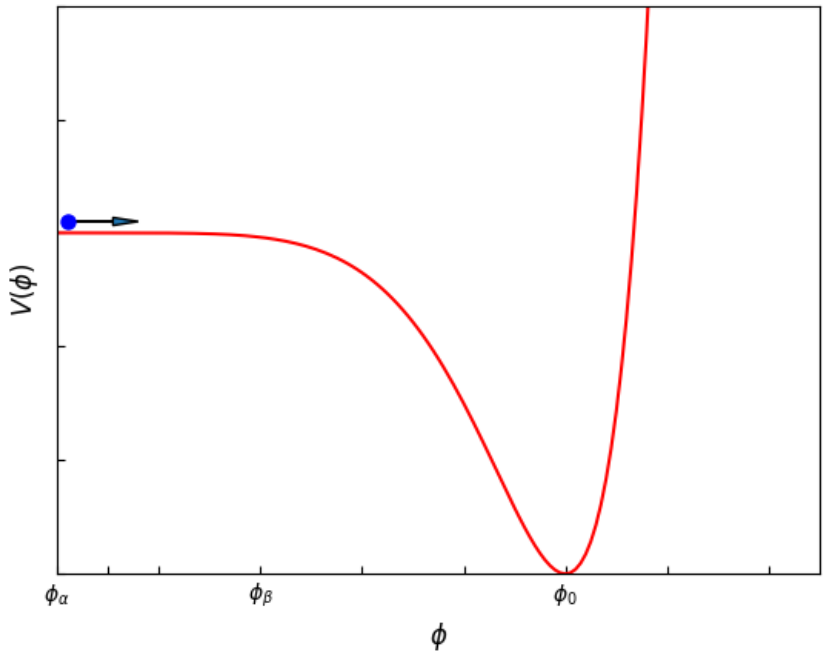

FIGURE 2.6: Here is presented the inflationary potential. The inflation starts at ϕ_α and ends at ϕ_β. In this initial part the curvature potential is very flat $(V(\phi) = V_0)$ to allow for slow roll in which time the Universe yields enough e-folds and then proceeds down the hill until it reaches the minimum ϕ_0

$$w = \frac{-1 + \dot{\phi}^2/2V(\phi)}{1 + \dot{\phi}^2/2V(\phi)}, \tag{2.31}$$

we can have an effective cosmological constant ($w = -1$) driving the expansion until $\phi = \phi_0$.

Despite the general acceptance of the inflationary theory among the cosmologists and the theoretical physicists community, there have been a series of criticisms concerning the lack of substantial empirical evidence. One of the most popular is that this inflationary field is an ad hoc artificiality accommodated to the current observations with no physical meaning. Either way this model is able to provide solutions and it is still the most accepted for the description of the early Universe which is impossible to be probed directly. Hopefully, the upcoming cosmological surveys will provide legacy datasets to be undergone thorough tests, shedding some light on this theory.

2.8 Cosmological distances

After having introduced the basic concepts in cosmology such as the scale factor α, the redshift z, the Hubble constant H_0, the cosmological parameters and the co-moving frame, we will proceed with the mathematical framework of the distance measures that have been applied in the observational cosmology.

2.8.1 Comoving distance

The *comoving distance* between two objects as we have already mentioned in section 2.1 is the constant distance assuming that those two objects move along with the Hubble flow. This is the *proper distance* (the measured distance with rulers at the exact time of the observation) multiplied by the factor $(1+z)$. To calculate the *co-moving distance* in the line of sight (hereafter l.o.s) direction between us and a distant object at redshift z is to take all the infinitesimal contributions and integrate radially from $z=0$ to source. We can rewrite Equation 2.22 as $H(z) = H_o E(z)$. The time-of-flight of a photon moving in a specific interval dz divided by that time α value is given by $dz/E(z)$. Thus, we can define the l.o.s comoving distance as the ratio of *proper distance* with the scale factor α that reads the following integral:

$$\chi(z) = d_H \int_0^z \frac{dx}{E(x)}, \tag{2.32}$$

where $d_H = cH_o^{-1}$. This is the correct distance measurement for the large-scale structure since it is that one between points having their distance estimated locally today if they are both stuck within the flow of the Hubble expansion. All the other distances in cosmology are simply based on the l.o.s *comoving distance*.

There is also the possibility for two objects to be separated by an angle $\delta\theta$ on the sky while both of them are at the same redshift z. Then the comoving distance between them is the angle $\delta\theta$ multiplied with the *transverse comoving distance* d_{trans} which is related to the l.o.s *comoving distance* as:

$$d_{trans}(z) = \begin{cases} d_H(1/\sqrt{\Omega_k}) \sinh\left(\sqrt{\Omega_k}\chi(z)/d_H\right) & \text{if} \quad \Omega_k > 0 \\ \chi(z) & \text{if} \quad \Omega_k = 0 \\ d_H(1/\sqrt{\Omega_k}) \sin\left(\sqrt{\Omega_k}\chi(z)/d_H\right) & \text{if} \quad \Omega_k < 0 \end{cases}. \tag{2.33}$$

2.8.2 Comoving volume

Given that a specific survey targets a fraction of the sky that reads:

$$f_{sky} = \frac{\Omega_{obs}}{4\pi}, \tag{2.34}$$

with Ω_{obs} the corresponding solid angle area, we can define the comoving volume in a redshift bin width dz:

$$dV = 4\pi f_{sky}\chi(z)^2 d\chi, \tag{2.35}$$

and by integrating between χ_{min} and χ_{max}:

$$V = \frac{4\pi}{3} f_{sky}\left(\chi^3_{max}(z) - \chi^3_{min}(z)\right). \tag{2.36}$$

2.8.3 Angular diameter distance

We can define the *angular diameter distance* by taking the ratio of the physical transverse size l of an object to its measured angular size $\delta\theta$ (in radians). It is related to the *transverse comoving distance* as:

$$d_A(z) = \frac{d_{trans}(z)}{1+z} = \frac{d_H}{1+z}\int_0^z \frac{dx}{E(x)}, \tag{2.37}$$

with the far right part holding true for $\Omega_k = 0$. (For $\Omega_K \neq 0$ we have the d_{trans} relation valid for $\Omega_K > 0$ and $\Omega_K < 0$ as given by Equation 2.33)

2.8.4 Luminosity distance

The *luminosity distance* can be defined as:

$$d_L = \sqrt{\frac{L}{4\pi S}}, \tag{2.38}$$

where L is the bolometric luminosity and S the bolometric flux integrated over all wavelengths. It is related to the *angular diameter distance* and the *transverse comoving distance* as:

$$d_L(z) = (1+z)d_{trans}(z) = (1+z)^2 d_A(z) = d_H(1+z)\int_0^z \frac{dx}{E(x)}, \tag{2.39}$$

with the far right part holding true for $\Omega_k = 0$. (For $\Omega_K \neq 0$ we have the d_{trans} relation valid for $\Omega_K > 0$ and $\Omega_K < 0$ as given by Equation 2.33)

2.9 Examples of geometrical probes: Supernovae Type Ia and Baryon Acoustic Oscillations

Type I*a* supernovae are objects known as 'standard candles', meaning that irrespective of the redshift where they are observed, they have distinct lightcurve shape from which we can infer their distance. These objects led to the great discovery of the accelerated expansion of the Universe (Riess et al., 1998; Perlmutter et al., 1998) and on top of that they are able to break degeneracies present in other data sets. SNI*a* are observationally characterized by two quantities. The color parameter C indicating the intrinsic reddening due to the dust present in its host galaxy at the peak of the

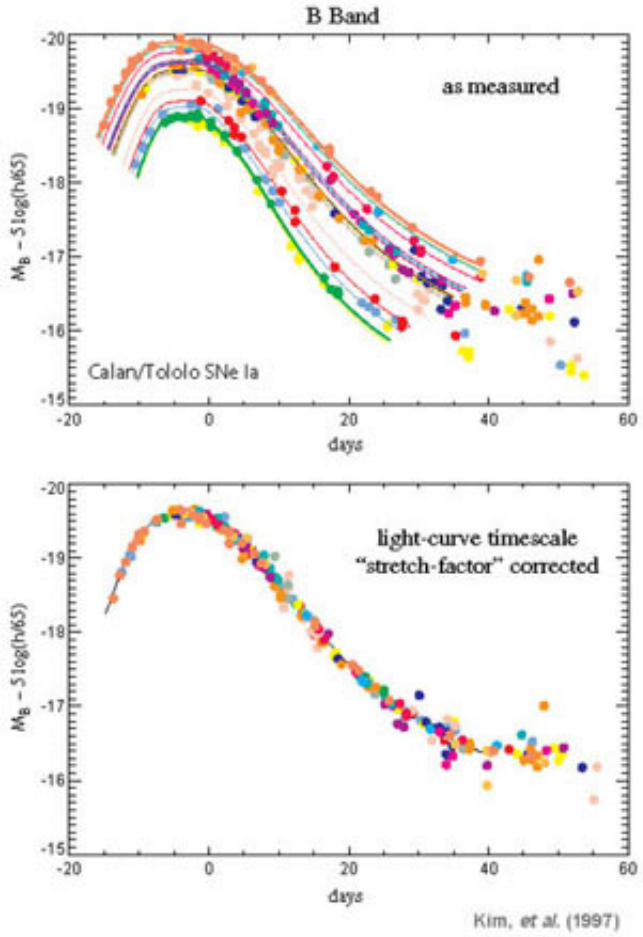

FIGURE 2.7: B-band $M_B - 5\log h/65$ as a function of time in days. Top: As observed. Bottom: After applying the *stretch factor* correction (Kim, 2004)

brightness and the stretch factor X_1 which is the average light-curve stretch in time. Thus, the observational distance modulus can be expressed as:

$$\mu_{obs} = m_B^* - M_B + aX_1 - \beta C, \tag{2.40}$$

where a, β are nuisance parameters, M_B is the absolute magnitude in the B band and m_B^* the rest frame peak magnitude in that band. It has been shown (Betoule, M. et al., 2014) that there is a dependency between the SNIa M_B and the mass of its host galaxy by a step function that reads:

$$M_B = \begin{cases} M_B^1 & \text{if} \quad M_{stellar} < 10^{10} M_\odot \\ M_B^1 + \Delta_M & \text{otherwise} \end{cases}, \tag{2.41}$$

with Δ_M a correcting nuisance parameter. The theoretical distance modulus is defined as a function of *luminosity distance*:

$$\mu_{th} = m - M = 5\log d_L(z) + 25 \quad \text{in Mpc.} \tag{2.42}$$

One can take the measurements of Equation 2.40 along with their corresponding error provided by a vector or a covariance matrix (in the case of cross-correlations) and the theoretical predictions of Equation 2.42 and fit several cosmological parameters.

The baryon acoustic oscillations (BAOs) are characteristic excess patterns observed in the 2-pt correlation function of the galaxy clustering (firstly reported on the SDSS Luminous Red Galaxies sample Eisenstein and Hu, 1998). They are pressure waves produced by the DM overdensed regions on the the photo-baryonic fluid at the early Universe. As we mentioned at the time of recombination ($z_{rec} \approx 1100$) photons decouple from baryons and start to free stream in the Universe while the sounds wave freeze. This exact scale is a 'standard ruler' and corresponds to the sound horizon length $d_s = 100\text{Mpc/h}$ (Eisenstein et al., 2005). The isotropic measurements of the BAO are taken by the ratio:

$$\frac{d_s(z_{drag})}{D_v(z)}, \tag{2.43}$$

where $d_s(z_{drag})$ is the size of the comoving sound horizon at the redshift of the baryon drag epoch $z_{drag} \approx 1060$:

$$d_s(z_{drag}) = \int_{z_{drag}}^{\infty} \frac{c_s(z)dz}{H(z)}, \tag{2.44}$$

with $c_s(z)$ the sound velocity as a function of redshift:

$$c_s(z) = \frac{c}{\sqrt{3(1+A(z))}}, \tag{2.45}$$

and $A(z) = 3\rho_b/4\rho_\gamma$ with ρ_b the baryon density and ρ_γ the photon density respectively. According to Eisenstein and Hu, 1998 we can approximate this term with $A(z) = 3.15 \times 10^4 \Omega_b h^2 \Theta_{2.7}^{-4}(1+z)^{-1}$ where $\Theta_{2.7} = T_{CMB}/2.7$. In the denominator of Equation 2.43 we have the effective distance (Eisenstein et al., 2005):

$$D_v(z) = \left((1+z)^2 d_A(z)^2 \frac{cz}{H(z)}\right), \tag{2.46}$$

where $d_A(z)$ is the *angular diameter distance*. In the case of anisotropic measurements we have two observed quantities being in the radial or transverse direction:

$$\delta z = \frac{d_s(z_{drag})H(z)}{c}, \tag{2.47}$$

$$\theta = \frac{d_s(z_{drag})}{(1+z)d_A(z)}. \tag{2.48}$$

Similarly to the SNI*a* analysis we are able to fit cosmological parameters using the theoretical predictions and the measured values with their joint uncertainties.

Chapter 3

Newtonian perturbation theory, structure formation and galaxy clustering probes

Until this point we treat the Universe as homogeneous and isotropic at a 'Background' level. However, the observed Universe is inhomogeneous and the creation and the evolution of this inhomogeneity is what we refer to as *structure formation*. We can probe the Universe's structure with the uneven distribution of galaxies called *galaxy clustering*. This distribution of objects active in a broad range of frequencies from radio to γ-rays, is of course nothing but the tracing of the non electromagnetically interacting *cold dark matter* (hereafter CDM). The primordial fluctuations of the young Universe were gravitationally amplified with the passing of time leading to the structures we see today. The theory of structures is dependent on two assumptions:

- **How these primordial fluctuations came about?** The most widely accepted scenario is *inflation* as we saw in section 2.7. It has been proposed that these structures stemmed from *quantum fluctuations* of the inflationary field at the time when scales crossed the horizon.
- **What led the later growth of fluctuations up to the current observations.** For this less speculative part, we have the well-established GR. Although the theory has been thoroughly tested, we are still unable to understand the exact nature of the Universe's largest components; DM and DE, the free streaming lengths and equation of state of which affect the growth of structures.

3.1 Perfect self-gravitating fluid

The equations of motion of a perfect non-relativistic and self-gravitating fluid at a position $\mathbf{r}$ and time t, with energy density ρ, pressure $P << \rho$ and velocity $\mathbf{v}$ are the Poisson, Continuity and Euler equations reading respectively:

$$\nabla^2_{\mathbf{r}}\Phi = 4\pi G\rho - \Lambda, \tag{3.1}$$

$$\partial_t \rho + \nabla_{\mathbf{r}} \cdot (\rho \mathbf{v}) = 0, \tag{3.2}$$

$$\partial_t \mathbf{v} + \mathbf{v} \cdot \nabla_{\mathbf{r}} \mathbf{v} = -\frac{1}{\rho} \nabla_{\mathbf{r}} P - \nabla_{\mathbf{r}} \Phi, \tag{3.3}$$

with Λ the usual cosmological constant and Φ the gravitational potential such that $\mathbf{g} = -\nabla_{\mathbf{r}} \Phi$ where $\mathbf{g}$ the gravitational acceleration.

3.2 Recovering the Background cosmology: Newtonian approach

As we introduced in section 2.1 we consider the Universe as a sphere of fluid expanding according to the Hubble law $\mathbf{v} = H(t)\mathbf{r}$. Considering that at $\mathbf{r} = 0$, $\Phi = 0$, the Poisson equation becomes:

$$\frac{\partial}{\partial r} \left(r^2 \frac{\partial \Phi}{\partial r} \right) = (4\pi G \rho - \Lambda) r^2, \tag{3.4}$$

and if we integrate we have:

$$\Phi = \frac{1}{6} (4\pi G \rho - \Lambda) r^2, \tag{3.5}$$

then the Euler equation becomes:

$$\frac{\partial H}{\partial t} \mathbf{r} + H^2 \mathbf{r} \cdot \nabla_{\mathbf{r}} \mathbf{r} = -\frac{1}{3} (4\pi G \rho - \Lambda) \mathbf{r}, \tag{3.6}$$

and since $\mathbf{r} \cdot \nabla_{\mathbf{r}} \mathbf{r} = \mathbf{r}$ we have:

$$\frac{\partial H}{\partial t} + H^2 = -\frac{1}{3} (4\pi G \rho - \Lambda), \tag{3.7}$$

which is the Newtonian limit of the Friedmann equations as seen in section 2.2 (there in the relativistic result has $\rho + 3P$ instead of ρ) and finally the continuity equation is:

$$\partial_t \rho + \nabla_{\mathbf{r}} \cdot [\rho(t) H(t) \mathbf{r}] = \partial_t \rho + 3\rho H = 0, \tag{3.8}$$

which is the energy conservation equation giving the solution $\rho \propto a^{-3}$, the familiar decay of the mass component during the expansion.

3.3 Coordinates of the comoving frame

As we have mentioned in section 2.1, any observer on the background level at *physical position* $\mathbf{r}$ has velocity $\mathbf{v} = d\mathbf{r}/dt = H(t)\mathbf{r}$, and since the *comoving distance* $\mathbf{x} = \mathbf{r}/a(t)$ is constant with cosmic history, it is more convenient to be adopted. This transforms the derivatives as:

$$\left(\frac{\partial}{\partial t}\right)_{\mathbf{r}} = \left(\frac{\partial}{\partial t}\right)_{\mathbf{x}} + \left(\frac{\partial \mathbf{x}}{\partial t}\right)_{\mathbf{r}} \cdot \nabla_{\mathbf{x}} = \left(\frac{\partial}{\partial t}\right)_{\mathbf{x}} - H(t)\mathbf{x} \cdot \nabla, \tag{3.9}$$

with $\nabla = \nabla_{\mathbf{x}}|_t$ and $\nabla_{\mathbf{r}} = \nabla/a$. Also we take ∂_t at fixed comoving distance $\mathbf{x}$.

3.4 Perturbed quantities

In perturbation theory we can write down a quantity as the sum of a background (where homogeneity and FRW Universe is assumed as we saw in section 3.2) value and a perturbation term deviating from that background value. For example at a given point $\mathbf{x}$ and at a time t the energy density ρ, pressure P and the velocity $\mathbf{v}$ of a perfect fluid as well as the potential Φ can be written as:

$$\rho = \overline{\rho}(t) + \delta\rho, \tag{3.10}$$

$$P = \overline{P}(t) + \delta P, \tag{3.11}$$

$$\mathbf{v} = a(t)H(t)\mathbf{x} + \mathbf{u}, \tag{3.12}$$

$$\Phi = \overline{\Phi}(\mathbf{x}, t) + \phi, \tag{3.13}$$

with ϕ the perturbed gravitational potential, and $\mathbf{u}$ the *peculiar velocity*. The latter quantity describes the deviations from the Hubble expansion in the comoving frame with time, since a particle in the flow has a velocity:

$$\mathbf{v} = \frac{d\mathbf{r}}{dt} = \frac{d(a\mathbf{x})}{dt} = aH\mathbf{x} + a\frac{d\mathbf{x}}{dt} = aH\mathbf{x} + \mathbf{u}. \tag{3.14}$$

The δ is the defined quantity:

$$\delta(x,t) = \frac{\delta\rho(x,t)}{\overline{\rho}(t)}, \tag{3.15}$$

as the *relative density fluctuation*, and it is necessary for $\delta \geq -1$ since always $\rho \geq 0$. It is possible to write these quantities for each fluid component of the Universe (CDM, radiation, DE). DE is expected to have negligible perturbation and in case of vaccum energy it is zero. For the late Universe we are going to focus on the matter density fluctuations that read:

$$\delta_m(x,t) = \frac{\delta\rho_m(x,t)}{\overline{\rho_m}(t)}. \tag{3.16}$$

So hereafter by δ we mean δ_m. Generally, perturbations are very small on the large scales, while at small scales they have grown large. Assuming that the perturbations are small, the approximated theory here is the *linear perturbation theory*. This means that higher order terms (the product of two or more perturbations are

zero) are eliminated. In detail, on the mean expansion rate the overdensities cancel the underdensities such that the average values would evolve as if there are no perturbations at all.

The idea is that if we subtract the zero terms corresponding to the homogeneity and isotropy from the equations, we end up with the perturbation equations containing only first order perturbation terms which are easy to be Fourier transformed.

In section 2.7 we saw that the cosmological scales exit the horizon during inflation, and then later enter back as we proceed to different species domination eras. After entering the horizon the matter fluctuations that are in subhorizon scales can be studied with the *Newtonian approach of perturbation theory*, while those at superhorizon or near the size of the horizon scales should be treated with *relativistic perturbation theory*.

Given that Equation 3.2 equals:

$$(1+\delta)\partial_t\bar{\rho} - H\bar{\rho}\mathbf{x}\cdot\nabla\delta + \bar{\rho}\partial_t\delta + \frac{\bar{\rho}}{\alpha}\nabla\cdot[(1+\delta)(\alpha H\mathbf{x}+\mathbf{u})] = 0, \tag{3.17}$$

and separating the terms to zeroth, first and second order we have:

$$[\partial_t\bar{\rho} + 3\bar{\rho}H] + \left[(\partial_t\bar{\rho} + 3\bar{\rho}H)\delta + \bar{\rho}\partial_t\delta + \frac{\bar{\rho}}{\alpha}\nabla\cdot\mathbf{u}\right] + \left[\frac{\bar{\rho}}{\alpha}(\mathbf{u}\cdot\nabla\delta + \delta\nabla\cdot\mathbf{u})\right] = 0, \tag{3.18}$$

by substituting the background term and ignoring the second order perturbations we get:

$$\partial_t\delta + \frac{1}{\alpha}\nabla\cdot\mathbf{u} = 0. \tag{3.19}$$

It is also easy to show that Poisson and Euler equations linearise as:

$$\nabla^2\phi = 4\pi G\alpha^2\bar{\rho}\delta, \tag{3.20}$$

$$\partial_t\mathbf{u} + H\mathbf{u} = -\frac{1}{\alpha\bar{\rho}}\nabla\delta P - \frac{1}{\alpha}\nabla\phi. \tag{3.21}$$

By taking the time derivative of Equation 3.18 we get:

$$\partial^2{}_t\delta - \frac{1}{\alpha}H\nabla\cdot\mathbf{u} + \frac{1}{\alpha}\nabla\cdot\partial_t\mathbf{u} = 0, \tag{3.22}$$

and after combining this with Equation 3.20 and Equation 3.21 we yield:

$$\partial^2{}_t\delta - \frac{1}{\alpha}H\nabla\cdot\mathbf{u} - \frac{1}{\alpha}\nabla\cdot\left[H\mathbf{u} + \frac{1}{\alpha\bar{\rho}}\nabla\delta P + \frac{1}{\alpha}\nabla\phi\right], \tag{3.23}$$

which finally is:

$$\partial^2{}_t\delta + 2H\partial_t\delta - 4\pi G\bar{\rho}\delta - \frac{1}{\alpha\bar{\rho}}\nabla^2\delta P = 0. \tag{3.24}$$

The above equation is the most fundamental in the *Newtonian theory* describing the competition of gravity with pressure as seen in the terms $4\pi G\bar{\rho}\delta$ and $\nabla^2\delta P$ respectively. Assuming a barotropic fluid satisfying $P = P(\rho)$ we have:

$$\delta P = \frac{\partial P}{\partial \rho}\bar{\rho}\delta = {c^2}_s\bar{\rho}\delta, \tag{3.25}$$

with c_s the sound speed. By Fourier transforming with $\nabla^2 \to -k^2$ the previous equation becomes:

$${\partial^2}_t\delta_k + 2H\partial_t\delta_k + \left[\frac{k^2{c^2}_s}{a^2} - 4\pi G\bar{\rho}\right]\delta_k = 0. \tag{3.26}$$

This is but the oscillator equation in the Hubble expansion and if $4\pi G\bar{\rho} < k^2{c^2}_s/a^2$ the pressure prevails giving rise to the sound waves of the fluid (acoustic oscillations). On the other hand, if $4\pi G\bar{\rho} > k^2{c^2}_s/a^2$ the gravitational accretion induces instability in the system. We can therefore define the Jeans length:

$$\lambda_J = {c^2}_s\sqrt{\frac{\pi}{\bar{\rho}G}}, \tag{3.27}$$

and those fluctuations exceeding the Jeans length become unstable under gravity, while for smaller scales they undergo pressure oscillations. For the case of a perfect fluid with $P > (-1/3)\rho$ the Jeans length grows faster than the comoving scale (proportional to a) during the expansion of the Universe affecting in this way the Fourier modes of the fluctuations, which initially start outside the Jeans scale and grow under gravitation and then later are inside the Jeans scale and oscillate.

3.5 CDM applications

3.5.1 EdS period

Long before the DE starts to prevail and right after the matter-radiation equality, we can describe the Universe as Einstein-de-Sitter with curvature $K = 0$ and pressure $P = 0$. In this era the cosmological scales are way larger than the Jeans length for the baryonic component and thus both baryons and CDM perturbations satisfy the same dynamics equations. Soon after the recombination the baryon fluctuations δ_b reaches that of the CDM δ_c and together behave as one single pressure-less fluid with total fluctuations such that:

$$\delta_m = \frac{\overline{\rho_b}\delta_b + \overline{\rho_c}\delta_c}{\overline{\rho_b} + \overline{\rho_c}} \approx \delta_c. \tag{3.28}$$

Also during this period $H^2 \propto \bar{\rho} \propto a^{-3}$ and $a \propto t^{2/3}$ which means that $4\pi G\bar{\rho} = 2/(3t^2)$. Thus, the density perturbations of matter are given by Equation 3.24 as:

$${\partial^2}_t\delta_m + \frac{4}{3t}\partial_t\delta_m - \frac{2}{3t^2}\delta_m = 0. \tag{3.29}$$

There are two independent solutions to the above equation, the decaying mode $\delta_m \propto a \propto t^{2/3}$ and the growing mode $\delta_m \propto t^{-1}$. Here, we should mention that as the Universe expands the gravitational growth has a power-law relation of δ, as opposed to the predicted exponential one in a non-expanding scenario. The gravitational potential remains constant since Equation 3.20 in Fourier space becomes:

$$-k^2\phi = 4\pi G = \text{const.} \tag{3.30}$$

3.5.2 The Meszaros phenomenon

According to this effect, during the radiation domination epoch the CDM fluctuations grow logarithmically for smaller scales than the sound horizon. We can generalise Equation 3.24 until the j-th component for a set of only gravitationally interacting fluids since CDM understands every clustered component through gravity:

$$\partial^2{}_t\delta_j + 2H\partial_t\delta_j - 4\pi G\sum_i \overline{\rho_i}\delta_i - \frac{1}{\alpha^2\bar{\rho}_j}\nabla^2\delta P_j = 0. \tag{3.31}$$

In the case of pressure-less CDM:

$$\partial^2{}_t\delta_c + 2H\partial_t\delta_c - 4\pi G\sum_i \overline{\rho_i}\delta_i = 0. \tag{3.32}$$

In the Newtonian approach, during the radiation epoch, the Jeans length for the fluctuations in the radiation fluid (where $c_s = 1/\sqrt{3}$) equals the size of the Hubble radius. The radiation perturbations with scales below that size are oscillating sound waves with zero time averaged density. Thus, only the CDM manage to cluster at this period:

$$\partial^2{}_t\delta_c + \frac{1}{t}\partial_t\delta_c - 4\pi G\bar{\rho}\delta_c = 0, \tag{3.33}$$

having used $H = 1/(2t)$ since $a \propto t^{1/2}$, and the CDM fluctuations evolve at cosmological timescales so:

$$\partial^2{}_t\delta_c \approx H^2\delta_c >> 4\pi G\overline{\rho_c}\delta_c, \tag{3.34}$$

with $\overline{\rho_r} >> \overline{\rho_c}$ during radiation epoch. Therefore, we can neglect the last term of Equation 3.33 and obtain the solutions $\delta_c = \text{const}$ and $\delta_c \propto \ln t$, meaning that the unclustered radiation keeps the δ_c growing only logarithmically.

3.5.3 Structure formation suppressed by late time Λ domination

In the late Universe the total matter component $\delta_m = \delta_c + \delta_b$ is the clustering component so we get:

$$\partial^2{}_t\delta_m + 2H\partial_t\delta_m - 4\pi G\overline{\rho_m}\delta_m = 0. \tag{3.35}$$

During the matter domination the above equation reduces to Equation 3.29 and $\delta_m \propto a$, but at the time when Λ starts to dominate $H \approx$ const and $a \propto e^{t\sqrt{\Lambda/3}}$. Given that $H^2 >> 4\pi G\overline{\rho_m}$ so:

$$\partial^2{}_t\delta_m + 2H\partial_t\delta_m \approx 0, \tag{3.36}$$

with solutions $\delta_m =$ const or $\delta_m \propto a^{-2}$ meaning that the growth of structure is suppressed in Λ epoch. In addition to that, a constant density fluctuation has as a consequence a decaying gravitational potential $\propto a^{-1}$. This is the well known *integrated Sachs-Wolfe effect* leaving an imprint on the CMB.

3.5.4 The baryon perturbations after recombination

Before recombination, the baryonic component has dynamics linked to the radiation via Compton scattering. At scales smaller than the sub-Hubble the δ_b oscillates similarly to radiation, after the radiation-matter equality $\delta_c \propto a$, and the moment after decoupling $\delta_c >> \delta_b$. Consequently, the baryons fall in the potential wells already formed by the CDM.

Provided that we ignore Λ and the baryonic pressure, the dynamics between baryons and CDM is given by:

$$\partial^2{}_t\delta_b + \frac{4}{3t}\partial_t\delta_b = 4\pi G(\overline{\rho_b}\delta_b + \overline{\rho_c}\delta_c), \tag{3.37}$$

$$\partial^2{}_t\delta_c + \frac{4}{3t}\partial_t\delta_c = 4\pi G(\overline{\rho_b}\delta_b + \overline{\rho_c}\delta_c). \tag{3.38}$$

By using Equation 3.28 and $\Delta = \delta_c - \delta_b$ we can decouple these equations:

$$\partial^2{}_t\Delta + \frac{4}{3t}\partial_t\Delta = 0, \tag{3.39}$$

having the solutions $\Delta =$ const or $\Delta \propto t^{-1/3}$, and δ_m following Equation 3.29 with solutions $\propto t^{-1}$ and $\propto t^{2/3}$. We have:

$$\frac{\delta_c}{\delta_b} = \frac{\overline{\rho_m}\delta_m + \overline{\rho_b}\Delta}{\overline{\rho_m}\delta_m - \overline{\rho_c}\Delta} \rightarrow \frac{\delta_m}{\delta_m} = 1. \tag{3.40}$$

It is clear that $\delta_b \rightarrow \delta_c$, and as a result a non negligible initial value of δ_b at the time of recombination leaves oscillations imprint on the late time matter fluctuation at a particular scale. This is the BAO as we saw in section 2.9.

3.6 Statistics of a stochastic field

The perturbations are a stochastic process having their origin back to the early Universe. The locations where these over-densities ($\delta > 0$) or under-densities ($\delta < 0$) occured are randomly determined, and thus we are not able to make precise theoretical predictions about them. What we can do is to make predictions of the statistical

properties of the homogeneous $\delta(\mathbf{x}, t)$ field. These properties are defined as averages of particular quantities. There are two kind of categories: the *ensemble average* and the *volume average*. The former is a theoretical and the later an observational concept. The volume average of a quantity $f(\mathbf{x})$ is:

$$\bar{f} = \frac{1}{V}\int_V d^3x f(\mathbf{x}), \tag{3.41}$$

with V the volume depending on each case. Regarding the ensemble average, we can assume that our Universe is but a single ensemble (realisation) of an infinite possible universes that could have randomly resulted from the initial fluctuations. To know this process would mean to know the probability distribution of every quantity generated. We can denote these quantities with q. These, for example, could be the produced initial density fluctuations at all positions $\delta(\mathbf{x})$ or their Fourier transforms $\delta(\mathbf{k})$ (as we will see in section 3.8). We can define the ensemble average (also named expectation value) of a quantity $f(q)$ depending on the q quantities as:

$$\langle f \rangle = \int dq P(q) f(q), \tag{3.42}$$

where $P(q)$ the probability distribution, and an example of f could be the density $\rho(\mathbf{x}, t)$, while the integral can in general have infinite dimensions. This is the probability distribution of all the possible universes. The prediction of such probability distribution can be made with a cosmological theory which is nonetheless unable to reproduce our real Universe realisation out of this distribution.

In the beginning of chapter 2 we talked about the *homogeneity* and *isotropy* of the Universe which constitute the first of the main pillars of *Cosmological Principle* and can be justified with the quantum fluctuations during the inflationary period (see section 2.7). Such properties can be described with the ensemble average. With the term *statistical homogeneity* we mean that at any $\mathbf{x}$ the ensemble average $\langle f(\mathbf{x}) \rangle$ has to be the same, so $\langle f(\mathbf{x}) \rangle = \langle f \rangle$. As for the *statistical isotropy*, this means that while some quantities depend on direction, the statistical properties are independent of this. For instance, all directions are equi-probable for the case of vector $\mathbf{v}$ and thus $\langle \mathbf{v} \rangle = 0$.

One can reasonably wonder how is it possible to compare theory with observations since the reality is just one case of the theoretical ensemble. Given a large number of realisations we should be capable of reproducing similar statistics for a specific part of the Universe when comparing it with different parts, providing in this way a good sample of the overall probability distribution. This is what we call *Ergodicity* and gives an estimate of how well one can compare theory with observations. Cosmological perturbations are assumed to be *ergodic*. Any field $f(\mathbf{x})$ satisfying:

$$\langle f \rangle = \bar{f}, \tag{3.43}$$

can be called *ergodic* at any random location $\mathbf{x}$ for $\langle f \rangle$, and an infinite V for $\bar{f}$. If the volume V under study is not infinite, the equality does not hold between theoretical predictions $\bar{f}$ and observations probing $\langle f \rangle$. This difference is the *cosmic variance* which is inverse proportional to the volume.

3.7 Autocorrelation function

As we saw in the previous section, the stochastic quantities like the density fluctuation are *ergodic* and therefore $\bar{\rho} = \langle \rho \rangle$ so $\langle \delta\rho \rangle = 0$ and generally $\langle \delta \rangle = 0$. Given that we are unable to measure inhomogeneity with that quantity. However, we can take the square of this which does not average out as $\langle \delta \rangle$ and it is necessary that is always ≥ 0. It is defined as the *variance* of the density fluctuation:

$$\langle \delta^2 \rangle = \frac{\langle \rho^2 \rangle}{\bar{\rho}^2}, \tag{3.44}$$

and its root mean square:

$$\delta_{rms} = \sqrt{\langle \delta^2 \rangle}, \tag{3.45}$$

which is the absolute value we could expect in a random position. This is a measure to test the level of inhomogeneity but nothing more beyond that. To access more information like the sizes and the shapes of the inhomogeneities, we should define the 2-pt autocorrelation function of the density perturbations at two locations $\mathbf{x_1}$ and $\mathbf{x_2}$:

$$\xi(\mathbf{x_1}, \mathbf{x_2}) = \langle \delta(\mathbf{x_1}) \delta(\mathbf{x_2}) \rangle. \tag{3.46}$$

With this function we can probe how the density fluctuations correlate between different locations, and it can be positive if the two regions have the same sign (if both are over-densities or under-densities) and negative if they have the opposite sign (one over-density and one under-density). We can redefine the correlation function using the *separation distance* $\mathbf{r} = \mathbf{x_2} - \mathbf{x_1}$ due to the space homogeneity:

$$\xi(\mathbf{r}) = \langle \delta(\mathbf{x}) \delta(\mathbf{x} + \mathbf{r}) \rangle, \tag{3.47}$$

and from spherical symmetry and statistical isotropy:

$$\xi(\mathbf{r}) = \xi(r). \tag{3.48}$$

As we can see in Figure 3.1 the correlation function is positive and large at r smaller than the standard under- or over- density region size and then smaller at larger r. When the separation distance is zero we have:

$$\langle \delta(\mathbf{x}) \delta(\mathbf{x}) \rangle = \langle \delta^2 \rangle = \xi(0). \tag{3.49}$$

Given only one realisation we can also write:

$$\widehat{\xi(\mathbf{r})} = \frac{1}{V}\int d^3x\delta(\mathbf{x})\delta(\mathbf{x}+\mathbf{r}), \tag{3.50}$$

and by integrating over **r**:

$$\int d^3r\widehat{\xi(\mathbf{r})} = \frac{1}{V}\int d^3rd^3x\delta(\mathbf{x})\delta(\mathbf{x}+\mathbf{r}) = \frac{1}{V}\int d^3\delta(\mathbf{x})\int d^3\delta(\mathbf{x}+\mathbf{r}) = 0, \tag{3.51}$$

due to the last integral being $\bar{\delta} = 0$. This integral applies also to $\xi(\mathbf{r})$ since $\xi(\mathbf{r}) = \langle\widehat{\xi(\mathbf{x})}\rangle$. Thus the correlation function $\xi(r)$ has to be negative at a certain point, so that an under-dense region is more probable to be found given some distance from an over-dense region. Of primary interest is the initially positive region of $\xi(r)$ at small r, while for very large separations the correlation function may have a very small amplitude and oscillate around zero.

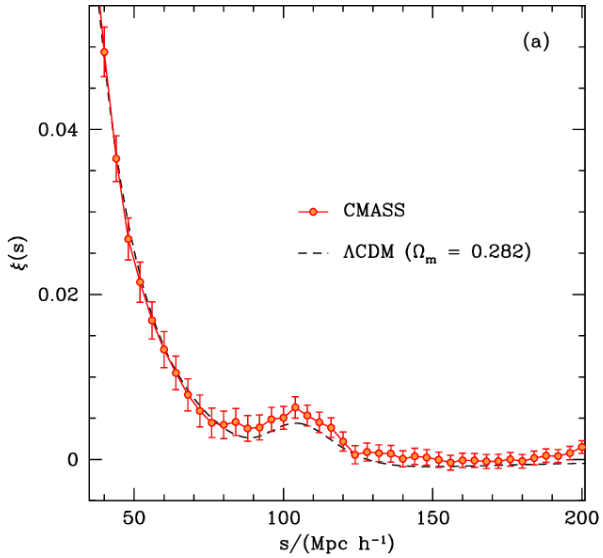

FIGURE 3.1: This is the 2-pt correlation function obtained from the DR9 (data release 9) of the CMASS BOSS (Baryonic Oscillation Spectroscopic Survey). The red dots with the errorbars are the observational points while the theoretical prediction for the ΛCDM model is shown with the dashed line. Around the scale of $100Mpch^{-1}$ we see the characteristic excess in the correlation function known as BAO (as we mentioned in section 2.9 (Sánchez et al., 2012)

3.8 The Fourier transformation and the power spectrum

In order to be easier to handle the distance scales on which the physics depends, one should separate these scales via Fourier transforming. Let us assume that the observable Universe is within a cubic box with periodic boundary conditions of volume $V = L^3$ and the region under study is a very small part of this, such that these conditions cannot affect it. Thus, if we consider the volume average of the Universe,

it has to be equal to the volume average of this box. Also the volume should be large enough to represent a fair ensemble sample as we saw from *ergodicity*. We can write to Fourier series a function $f(\mathbf{x})$ as:

$$f(\mathbf{x}) = \sum_{\mathbf{k}} f_{\mathbf{k}} e^{i\mathbf{k}\cdot\mathbf{x}}, \tag{3.52}$$

where the coefficients $f_{\mathbf{k}}$ are given by

$$f_{\mathbf{k}} = \frac{1}{V}\int_V f(\mathbf{x}) e^{-i\mathbf{k}\cdot\mathbf{x}} d^3x, \tag{3.53}$$

and the summed wavevectors $\mathbf{k} = \{k_1, k_2, k_3\}$ defined as:

$$k_i = \frac{2\pi n_i}{L}, \tag{3.54}$$

with $n_i = 0, \pm 1, \pm 2$, and $\mathbf{k} = 0$ is impossible if $f(\mathbf{x})$ is a perturbation with zero mean value. This expansion holds when the curvature of the background Universe is flat or even closed or open provided that the curvature radius is way larger that the size of the region under study. For separations $\Delta k_i = 2\pi/L$ we can replace the series with an integral:

$$f(\mathbf{x}) = \sum_{\mathbf{k}} f_{\mathbf{k}} e^{i\mathbf{k}\cdot\mathbf{x}} \left[\frac{L}{2\pi}\right]^3 \Delta k_1 \Delta k_2 \Delta k_3 \approx \frac{1}{(2\pi)^3}\int f(\mathbf{k}) e^{i\mathbf{k}\cdot\mathbf{x}} d^3k, \tag{3.55}$$

with $f(\mathbf{k}) = L^3 f_{\mathbf{k}}$ while the volume V and the coefficient's size depend on each other. The above approximation at the limit of $V \to \infty$ is exact, taking the pair of *Fourier transform*:

$$f(\mathbf{x}) = \frac{1}{(2\pi)^3}\int f(\mathbf{k}) e^{i\mathbf{k}\cdot\mathbf{x}} d^3k \qquad \text{and} \qquad f(\mathbf{k}) = \int f(\mathbf{x}) e^{-i\mathbf{k}\cdot\mathbf{x}} d^3x, \tag{3.56}$$

which converges requiring that for $|\mathbf{x}| \to \infty$, $f(\mathbf{x}) \to 0$.

Now we shall expand with a Fourier series the density fluctuations:

$$\delta(\mathbf{x}) = \sum_{\mathbf{k}} \delta_{\mathbf{k}} e^{i\mathbf{k}\cdot\mathbf{x}}, \tag{3.57}$$

where

$$\delta_{\mathbf{k}} = \frac{1}{V}\int_V \delta(\mathbf{x}) e^{-i\mathbf{k}\cdot\mathbf{x}} d^3x, \tag{3.58}$$

with $\delta_{-\mathbf{k}} = \delta^*_{\mathbf{k}}$. We should note that $\langle\delta(\mathbf{x})\rangle = 0$ meaning that $\langle\delta_{\mathbf{k}}\rangle = 0$.

Having defined the correlation function $\xi(\mathbf{x}, \mathbf{x}')$ we shall proceed to the Fourier spaced correlation $\langle\delta^*{}_{\mathbf{k}}\delta_{\mathbf{k}'}\rangle$, such that the autocorrelation $\langle\delta^*{}_{\mathbf{k}}\delta_{\mathbf{k}}\rangle = \langle|\delta_{\mathbf{k}}|^2\rangle \geq 0$ is just the $\delta_{\mathbf{k}}$ variance. Now we can calculate:

$$\langle\delta^*{}_{\mathbf{k}}\delta_{\mathbf{k}'}\rangle = \frac{1}{V^2}\int d^3x e^{-i\mathbf{k}\cdot\mathbf{x}} \int d^3x' e^{-i\mathbf{k}'\cdot\mathbf{x}'} \langle\delta(\mathbf{x})\delta(\mathbf{x}')\rangle, \tag{3.59}$$

and by applying $\mathbf{x}' = \mathbf{x} + \mathbf{r}$ and $\langle \delta(\mathbf{x})\delta(\mathbf{x}+\mathbf{r})\rangle$ we obtain:

$$= \frac{1}{V^2}\int d^3x e^{-i\mathbf{k}\cdot\mathbf{x}} \int d^3r e^{-i\mathbf{k}'\cdot(\mathbf{x}+\mathbf{r})}\langle \delta(\mathbf{x})\delta(\mathbf{x}+\mathbf{r})\rangle = \frac{1}{V^2}\int d^3r e^{-i\mathbf{k}'\cdot\mathbf{r}}\xi(\mathbf{r}) \int d^3x e^{i(\mathbf{k}-\mathbf{k}')\cdot\mathbf{x}}, \tag{3.60}$$

which is finally:

$$= \frac{1}{V}\delta_{\mathbf{k}\mathbf{k}'}\int d^3r e^{-i\mathbf{k}\cdot\mathbf{r}}\xi(\mathbf{r}) = \frac{1}{V}\delta_{\mathbf{k}\mathbf{k}'}P(\mathbf{k}), \tag{3.61}$$

resulting from the fact that the plane waves are orthogonal and the space is *statistically homogeneous* and we have:

$$\int d^3x e^{-i(\mathbf{k}-\mathbf{k}')\cdot\mathbf{x}} = \delta_{\mathbf{k}\mathbf{k}'} \to (2\pi)^3\delta_D^3(\mathbf{k}-\mathbf{k}'), \tag{3.62}$$

at the limit $V \to \infty$ with $\delta_{\mathbf{k}\mathbf{k}'}$ the Kronecker delta. By replacing $\delta(\mathbf{k}) = V\delta_{\mathbf{k}}$ we see that the $\delta_{\mathbf{k}}$ Fourier coefficients are correlated due to the *statistical homogeneity* since:

$$\langle \delta(\mathbf{k})^*\delta(\mathbf{k}')\rangle = V\delta_{kk'}P(\mathbf{k}) \to (2\pi)^3\delta_D^3(\mathbf{k}-\mathbf{k}')P(\mathbf{k}). \tag{3.63}$$

And the quantity called power spectrum, giving the variance of δ_k is defined as:

$$P(\mathbf{k}) = V\langle|\delta_{\mathbf{k}}|^2\rangle = \int d^3r e^{-i\mathbf{k}\cdot\mathbf{r}}\xi(\mathbf{x}), \tag{3.64}$$

which is the 3-dimensional Fourier transform of the correlation function $\xi(\mathbf{x})$:

$$\xi(\mathbf{r}) = \frac{1}{(2\pi)^3}\int d^3k e^{i\mathbf{k}\cdot\mathbf{r}}P(\mathbf{k}), \tag{3.65}$$

and is always positive unlike the correlation function that goes to zero for large separations making this one the most optimal choice when the large distances are of interest. In addition to that, we infer from statistical isotropy that $\xi(\mathbf{x}) = \xi(x) \to P(\mathbf{k}) = P(k)$ and any function maintains its spherical symmetry in the 3D Fourier transform. It is therefore easy to write the 1-dimensional correlation function and power spectrum in spherical coordinates:

$$\xi(r) = \left(\frac{1}{2\pi}\right)^3\int_0^\infty P(k)\frac{\sin(kr)}{kr}4\pi k^2 dk, \tag{3.66}$$

$$P(k) = \int_0^\infty \xi(r)\frac{\sin(kr)}{kr}4\pi r^2 dr. \tag{3.67}$$

The power spectrum has dimensions $\mathrm{Mpc}^3\mathrm{h}^{-3}$. The density autocorrelation function reads:

$$\xi(0) = \langle\delta^2\rangle = \left(\frac{1}{2\pi}\right)^3\int_0^\infty P(k)4\pi k^2 dk = \int_{-\infty}^\infty \Delta^2(k)d\ln k, \tag{3.68}$$

where we defined the dimensionless power spectrum:

$$\Delta^2(k) = \frac{k^3}{2\pi^2} P(k). \tag{3.69}$$

3.9 Growth factor, transfer function and matter power spectrum

At the time of matter-radiation equality (where $\rho_r = \rho_m$) those modes with $k > k_{eq}$ are inside the horizon while those for $k < k_{eq}$ are outside. Also, during radiation domination it holds that $H \propto a^{-2}$ and during the matter domination $H \propto a^{-3/2}$. As we have already mentioned, the matter fluctuations inside the gravitational potential stem from the primordial fluctuations during inflation. They were initially on super-horizon scales due to the exponential growth and later evolved classically. GR predicts that these fluctuations remained almost constant when outside the horizon. After crossing the horizon they start to evolve and affect the matter fluctuations. Regarding the CDM perturbations, they can only be influenced by the gravitational potential since the sound velocity is zero rendering the pressure insignificant. We should note that, the Fourier modes evolve identically at late times. Prior to that, what is important is the exact time of the mode crossing inside the horizon and in particular whether it occurs before or after a_{eq}. This has the consequence that modes with $k > k_{eq}$ are suppressed while those with $k < k_{eq}$ are not. Given that, we can factorize the gravitational potential as:

$$\Phi(k, a) = \Phi_\zeta(k) \cdot T(k) \cdot \frac{D(a)}{a}, \tag{3.70}$$

with $\Phi_\zeta(k)$ the primordial potential, $T(k)$ the *transfer function* describing the Fourier mode evolution in the horizon crossing and at the time of the matter-radiation equality and $D(a)$ the scale-independent *growth factor* describing the late time growth of the perturbations which is normalised as $D(a) = a$ in the Einstein-de Sitter model. The *transfer function* is usually defined as:

$$T(k) = \frac{\Phi(k, a_+)}{\Phi(k_{LS}, a_+)}, \tag{3.71}$$

with k_{LS} the large-scale modes and a_+ the times very close to decoupling. Also the scale-independent *growth factor* can be expressed at late times as:

$$\frac{D(a)}{a} = \frac{\Phi(k, a)}{\Phi(k, a_+)}. \tag{3.72}$$

Now we can rewrite Equation 3.70 as:

$$\Phi(k, a) = \frac{9}{10} \Phi_\zeta(k) T(k) \frac{D(a)}{a}, \tag{3.73}$$

where the prefactor corresponds to a 10% decrease at large scales during the radiation period. Additionally, we know that in Fourier space the Poisson equation becomes:

$$-\frac{k^2}{\alpha^2}\Phi = 4\pi G\bar{\rho}\delta, \tag{3.74}$$

and with some easy manipulations we have:

$$\delta(k,\alpha) = -\frac{\alpha k^2\Phi(k,\alpha)}{\frac{3}{2}\Omega_m H_0^2}. \tag{3.75}$$

Finally by inserting Equation 3.73 we get:

$$\delta(k,\alpha) = -\frac{3}{5}\frac{k^2}{\Omega_m H_0^2}\Phi_\zeta(k)T(k)D(\alpha). \tag{3.76}$$

Starting from inflation described by a scalar field we derive the power spectrum similarly to the definition Equation 3.63 seen in section 3.8:

$$\left\langle \Phi_\zeta(\mathbf{k})^*\Phi_\zeta(\mathbf{k}')\right\rangle = (2\pi)^3\delta^3{}_D(\mathbf{k}-\mathbf{k}')P_\zeta(k), \tag{3.77}$$

where

$$P_\zeta(k) = \frac{50\pi^2}{9k^3\delta_H^{-2}}\left(\frac{k}{H_0}\right)^{n_s-1}\left(\frac{\Omega_m}{D(\alpha=1)}\right)^2, \tag{3.78}$$

with n_s the spectral index and δ_H the large scale normalisation constant. Now, we define the matter power spectrum (which from now on is denoted simply as P) as:

$$\left\langle \delta(\mathbf{k})^*\delta(\mathbf{k}')\right\rangle = (2\pi)^3\delta^3{}_D(\mathbf{k}-\mathbf{k}')P(k,\alpha), \tag{3.79}$$

and considering Equation 3.76,Equation 3.77,Equation 3.78 we finally obtain for times $\alpha > \alpha_+$:

$$P(k,\alpha) = \frac{2\pi^2\delta_H^2 k^{n_s}}{H_0^{n_s+3}}T^2(k)\left(\frac{D(\alpha)}{D(\alpha=1)}\right)^2, \tag{3.80}$$

which can be written at present time $\alpha = 1$:

$$P(k) = \zeta(k)T^2(k), \tag{3.81}$$

where $\zeta(k) = Ak^{n_s}$ the primordial power spectrum and A the new constant containing the previous constants.

The treatment inside the horizon assuming the Newtonian approach is feasible, while that outside the horizon warrants for the GR. The scale factor at the matter-radiation equality is $\alpha_{eq} = (1+z_{eq})^{-1} = \Omega_r/\Omega_m$ with a wavenumber $k_{eq} = H_{eq}\alpha_{eq}$ since the comoving distance is $(H_{eq}\alpha_{eq})^{-1}$. Generally, a mode k crosses the horizon

at the point where $k = H\alpha$. The comoving Hubble length grew after inflation, and during the radiation period was $\propto t^{1/2}$ while in the matter period was $\propto t^{1/3}$.

As the time passed, new scales entered the horizon. Those scales for $k < k_{eq}$ which are larger than $(H_{eq}\alpha_{eq})^{-1}$ crossed the horizon in the matter period. Those modes never stopped growing since they grew by α^2 in radiation period and by α in matter period. Thus, the fluctuations with $k < k_{eq}$ between a time t_i before the equality and a time t_f after it evolved like:

$$\delta(t_f) = \frac{\delta(t_{eq})\delta(t_f)}{\delta(t_i)\delta(t_{eq})}\delta(t_i) = \frac{\alpha_{eq}^2\alpha_f}{\alpha_i^2\alpha_{eq}}\delta(t_i), \tag{3.82}$$

which is a scale-independent quantity, allowing the transfer function to be constant at this regime.

Regarding the scales $k > k_{eq}$, those crossed the horizon during the radiation period, experiencing a suppression of growth contrary to the larger scales while inside the horizon at the radiation period. As a result a scale $k_{cross} = H_{cross}\alpha_{cross}$ is suppressed between the times t_{cross} and t_{eq} for $k > k_{eq}$ yielding:

$$\delta(t_f) = \frac{\delta(t_{cross})\delta(t_f)}{\delta(t_i)\delta(t_{eq})}\delta(t_i) = \frac{\alpha_{cross}^2\alpha_f}{\alpha_i^2\alpha_{eq}}\delta(t_i) = \frac{\alpha_{cross}^2}{\alpha_{eq}} \cdot \left(\frac{\alpha_{eq}^2\alpha_f}{\alpha_i^2\alpha_{eq}^2}\right)\delta(t_i). \tag{3.83}$$

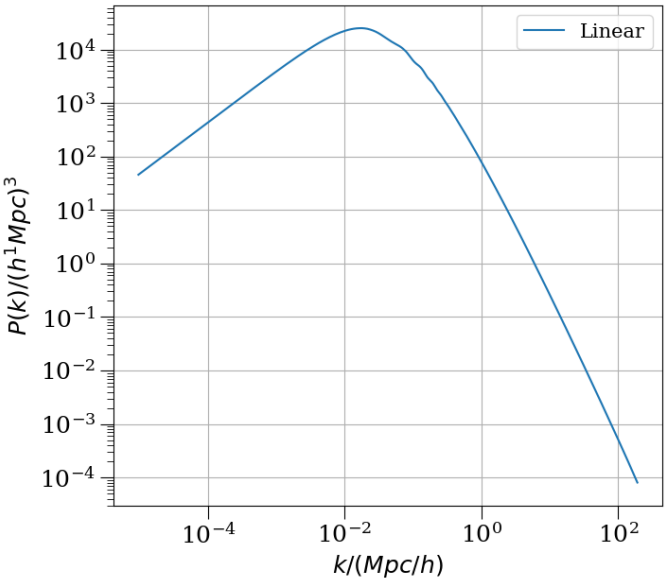

FIGURE 3.2: The matter power spectrum as a function of scale (image produced using the `CosmoSIS` package code)

with the second term being the same as in the case of $k < k_{eq}$ and the first term yielding the growth suppression for the mode inside the horizon at the radiation

epoch where $k_{cross} \propto \alpha_{cross}^{-1}$. Hence, the transfer function has the scale-dependent behavior:

$$T(k) \begin{cases} = 1 & \text{if} \quad k < k_{eq} \\ \propto k^{-2} & \text{if} \quad k > k_{eq} \end{cases}, \tag{3.84}$$

imprinted also on the present day matter power spectrum with the characteristic bend on the scale $k_{eq} \propto h\Omega_m$ (see Figure 3.2),

$$P(k) \begin{cases} \propto k & \text{if} \quad k < k_{eq} \\ \propto k^{-3} & \text{if} \quad k > k_{eq} \end{cases}. \tag{3.85}$$

We should note that in the case of including baryons on top of the cold dark matter fluctuations (hereafter CDM) we have the damping effect on the matter power spectrum (excluding neutrinos) due to the BAOs at the scale $k = n\pi \left(c_s \int_0^{t_{rec}} \frac{dt}{\alpha(t)} \right)^{-1}$ with n a positive integer.

3.10 Galaxy bias

The galaxy density fluctuations are related to the matter density fluctuations in the large-scale limit according to:

$$\delta_g = b\delta_m, \tag{3.86}$$

where the linear galaxy bias constant b accounts for the fact that the galaxies are not the perfect representation of the underlying matter field. The galaxy bias is generally described as a scale-independent function of redshift, the functional form of which changes according to the galaxy survey type specifications. Nonetheless, it can also be a scale-dependent quantity if the physics considered demands it (for example, in a massive neutrino scenario; for details see chapter 6). Hence, the galaxy Fourier space power spectrum due to Equation 3.79 is defined as:

$$P_g(k) = b^2 P(k). \tag{3.87}$$

3.11 Growth rate

One way to discriminate between different theories of gravity and cosmological models (Song and Percival, 2009) is with the linear growth rate f of the large-scale structure. This parameter can be constrained with the measurements of the peculiar velocities and the redshift-space distortions (hereafter RSD) (Raccanelli et al., 2013). The modelling of the large-scale RSD is feasible with the linear perturbation theory (Guzzo et al., 2008). The growth rate is defined as:

$$f = \frac{d \ln D}{d \ln \alpha} = -\frac{(1+z)}{D} \frac{dD}{dz}. \tag{3.88}$$

From Equation 3.26 we can easily derive the growth rate f evolution equation:

$$\frac{df}{d\ln a} + f^2 + \left(2 + \frac{\dot{H}}{H^2}\right) = \frac{3}{2}\Omega_m. \tag{3.89}$$

There are several parameterisations of the growth rate with the most common and simplest that of a power-law total matter fraction parameter (Peebles, 1980):

$$f(z) = \Omega_m(z)^\gamma, \tag{3.90}$$

where γ is the growth index, which is generally a constant and time-invariant. However, the γ value predictions can differ depending on the considered theory of gravity. For example, the vanilla ΛCDM+GR model yields $\gamma \approx 0.55$, while self-accelerating Modified Gravity models predict a $\gamma \approx 0.68$ (Linder, 2008). Thus, it is essential that this parameter be constrained.

3.12 Redshift-space distortions

In principle, the spatial distribution of the galaxies can be reconstructed with Equation 2.32 provided that the galaxy redshifts and cosmological parameters of interest are known. Nonetheless, in redshift-space the position of these objects is not an exact representation of their positions. Apart from the cosmological recession, the galaxies as members of groups, interact gravitationally with each other, as well as with their local environment. This induces an extra term accounting for the peculiar velocities that is added on top of the Hubble flow (see Equation 3.14) and the observed redshift is $z_{obs} = z_{cos} + z_{pec}$. Thus, the resulting image of the sources in redshift-space is squashed and deformed (see Figure 3.3). In particular, at large scales, the sources fall into high density regions, squashing the density field in the redshift-space since the clustering in the l.o.s direction is enhanced. This is known as the *Kaiser effect* (Kaiser, 1987a). In addition, the random and virialized motions of galaxies on small scales result in the stretching of the density field when observed in redshift-space and the clustering in the l.o.s is reduced. This is known as the *Finger-Of-God effect* (Jackson, 1972).

Assuming GR and neglecting the gravitational potential relating to the peculiar velocities we can estimate the redshift of the observed light ray as:

$$1 + z_{obs} = \frac{E_s(1 + \mathbf{u_s} \cdot \hat{\mathbf{n}})}{E_o}, \tag{3.91}$$

with E_s the photon energy at the source, E_o the photon energy at the observer, $\mathbf{u_s}$ the peculiar velocity of the source and $\hat{\mathbf{n}}$ the l.o.s direction. Considering now that there are not peculiar velocities the cosmological redshift would be:

$$1 + z_{cos} = \frac{E_s}{E_o}. \tag{3.92}$$

From Equation 3.91 and Equation 3.92 we have:

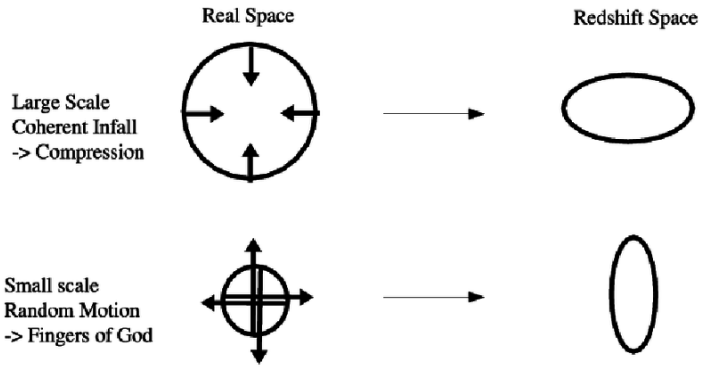

FIGURE 3.3: The Kaiser and the Finger-Of-God effect . The observer is at the bottom of the figure looking up. Transverse motions do not contribute any effect. From Thomas et al., 2004.

$$1 + z_{obs} = (1 + \mathbf{u_s} \cdot \hat{\mathbf{n}})(1 + z_{cos}), \tag{3.93}$$

and therefore the redshift difference induced by the source's peculiar velocity is:

$$\delta z = z_{pec} = z_{obs} - z_{cos} = (\mathbf{u_s} \cdot \hat{\mathbf{n}})(1 + z_{cos}). \tag{3.94}$$

We can define the comoving distances in the real and the redshift space as $\mathbf{r} = \chi(z_{cos})\hat{\mathbf{n}}$ and $\mathbf{s} = \chi(z_{obs})\hat{\mathbf{n}}$ respectively. By Taylor expanding to the first order the real comoving distance:

$$\chi(z_{obs}) = \chi(z_{cos} + \delta z) = \chi(z_{cos}) + \frac{d\chi(z_{obs})}{dz_{cos}}\delta z, \tag{3.95}$$

and according to the Equation 2.32 setting $c = 1$ we have

$$\chi(z_{obs}) = \chi(z_{cos} + \delta z) = \chi(z_{cos}) + \frac{\delta z}{H(z_{cos})}, \tag{3.96}$$

and inserting Equation 3.94 we obtain:

$$\mathbf{s} = \mathbf{r} + \frac{1 + z_{cos}}{H(z_{cos})}\mathbf{u_s}(\mathbf{r}) \cdot \hat{\mathbf{n}}. \tag{3.97}$$

From the mass conservation we know that the number desnity of galaxies observed in the real and the redshift-space should be the same:

$$n_g^s d\mathbf{s} = n_g^r d\mathbf{r}, \tag{3.98}$$

which is:

$$n_g^r(1 + \delta_m(\mathbf{s}))d\mathbf{s} = n_g^r(1 + \delta_m(\mathbf{r}))d\mathbf{r}. \tag{3.99}$$

Assuming cylindrical coordinates and the l.o.s on the z-axis direction, it holds:

$$d\mathbf{s} = \frac{\partial s}{\partial r} d\mathbf{r} = \frac{\partial \chi(z_{obs})}{\partial \chi(z_{cos})} d\mathbf{r}, \tag{3.100}$$

where:

$$\frac{\partial \chi(z_{obs})}{\partial \chi(z_{cos})} = 1 + \frac{1}{H(z_{cos})} \frac{\partial \delta z}{\partial \chi(z_{cos})} - \frac{1}{H^2(z_{cos})} \frac{\partial H(z_{cos})}{\partial \chi(z_{cos})} \delta z, \tag{3.101}$$

the third term is negligible since the Hubble rate is quite small compared to the second term, and now using Equation 3.101, Equation 3.100, Equation 3.99 and Equation 3.94 we finally have:

$$\delta_m(\mathbf{s}) = \delta_m(\mathbf{r}) - \frac{1 + z_{cos}}{H(z_{cos})} \frac{\partial}{\partial \chi(z_{cos})} \mathbf{u_s}(\mathbf{r}) \cdot \hat{\mathbf{n}}, \tag{3.102}$$

which is the so-called Kaiser formula.

It is convenient to define the divergence field of velocity as follows:

$$\theta(\mathbf{r}) = -\frac{\nabla \cdot \mathbf{u_s}(\mathbf{r})}{\alpha_{cos} f H(z_{cos})}, \tag{3.103}$$

with the Fourier transformation:

$$\mathbf{u_s}(\mathbf{k}) = -iH(z_{cos}) \alpha_{cos} f \frac{\mathbf{k}}{k^2} \theta(\mathbf{k}). \tag{3.104}$$

Using the continuity equation Equation 3.19 and the growth rate definition Equation 3.88 we see that:

$$\delta_m^r(\mathbf{k}) = \theta(\mathbf{k}). \tag{3.105}$$

Now, if we Fourier transform the observed matter fluctuation field in the plane-parallel approximation (where the large-scale separations are smaller than the observer-sources distance) we have:

$$\begin{aligned} \delta_m^s(\mathbf{k}) &= \int d\mathbf{s} \delta_m(\mathbf{s}) e^{i\mathbf{k}\cdot\mathbf{s}} \\ &= \int d\mathbf{r} \left(\delta_m(\mathbf{r}) - \frac{1}{\alpha_{cos} H(z_{cos})} \frac{\partial}{\partial \chi(z_{obs})} \mathbf{u_s}(\mathbf{r}) \cdot \hat{\mathbf{n}} \right) e^{i\mathbf{k}\cdot\mathbf{r} + ik\mu u_s / (\alpha_{cos} H(z_{cos}))}, \end{aligned} \tag{3.106}$$

with $\mu = \hat{\mathbf{k}} \cdot \hat{\mathbf{n}}$. Finally, keeping the linear order terms for u_s and δ and neglecting the second power term in the exponential we have:

$$\begin{aligned} \delta_m^s(\mathbf{k}) &= \delta_m^r(\mathbf{k}) - \int d\mathbf{r} e^{i\mathbf{k}\cdot\mathbf{r}} \frac{1}{\alpha_{cos} H(z_{cos})} \frac{\partial}{\partial \chi(z_{cos})} \int \frac{d\mathbf{k}'}{(2\pi)^3} e^{i\mathbf{k}'\cdot\mathbf{r}} \mathbf{u_s}(\mathbf{k}') \\ &= \delta_m^r(\mathbf{k}) + f \int \frac{d\mathbf{k}'}{(2\pi)^3} \int d\mathbf{r} e^{[i(\mathbf{k}-\mathbf{k}')\cdot\mathbf{r}]} \frac{kk'}{k^2} \theta(\mathbf{k}) \\ &= \delta_m^r(\mathbf{k}) + \mu^2 f \theta(\mathbf{k}) \\ &= (1 + f\mu^2) \delta_m^r(\mathbf{k}), \end{aligned} \tag{3.107}$$

which means that

$$\delta_m(\mathbf{s}) = (1 + f\mu^2)\delta_m(\mathbf{r}), \tag{3.108}$$

and therefore the observed matter Fourier-space power spectrum is:

$$P^s(k,\mu) = (1 + f\mu^2)^2 P^r(k). \tag{3.109}$$

Due to Equation 3.86 the observed galaxy Fourier-space power spectrum reads:

$$P_g^s(k,\mu) = b^2(1 + \beta\mu^2)^2 P^r(k) = (1 + \beta\mu^2)P_g^r(k), \tag{3.110}$$

where we define the distortion parameter $\beta = f/b$. A complete modelling of the RSD would need for the small scale contribution of the Finger-Of-God effect. The correct treatment for this, is to consider a dispersion model to account for the damping effect on the non-linear scales. However, in this work we restrict our study only in the linear regime, and therefore we do not include it.

We can expand the $P_g^s(k,\mu)$ with Legendre polynomials,

$$P_g^s(k,\mu) = \sum_\ell P_{g,\ell}^s(k)\mathcal{L}_\ell(\mu), \tag{3.111}$$

and

$$P_{g,\ell}^s(k) = \frac{2\ell+1}{2}\int_{-1}^{+1} d\mu P_g^s(k,\mu)\mathcal{L}_\ell(\mu). \tag{3.112}$$

It is evident from Equation 3.108 that the terms are up to μ^4 and since only the absolute value of μ is important in the RSD, the odd multipoles $P_{g,1}, P_{g,3}$ are zero and the $P_{g,0}, P_{g,2}, P_{g,4}$ which are the monopole, the quadropole and hexadecapole are non vanishing, reading respectively:

$$\begin{aligned} P_{g,0}^s(k) &= \frac{1}{2}\int_{-1}^{+1} d\mu b^2(1 + \beta\mu^2)^2 P^r(k) \\ &= \left(b^2 + \frac{2}{3}fb + \frac{1}{5}f^2\right) P^r(k), \end{aligned} \tag{3.113}$$

$$\begin{aligned} P_{g,2}^s(k) &= \frac{5}{2}\int_{-1}^{+1} d\mu \frac{1}{2}(3\mu^2 - 1)b^2(1 + \beta\mu^2)^2 P^r(k) \\ &= \left(\frac{4}{3}fb + \frac{4}{7}f^2\right) P^r(k), \end{aligned} \tag{3.114}$$

$$\begin{aligned} P_{g,4}^s(k) &= \frac{9}{2}\int_{-1}^{+1} d\mu \frac{35\mu^4 - 30\mu^2 + 3}{8} b^2(1 + \beta\mu^2)^2 P^r(k) \\ &= \left(\frac{8}{35}f^2\right) P^r(k), \end{aligned} \tag{3.115}$$

and provided that we know the galaxy bias b and the real matter Fourier-space power spectrum $P^r(k)$ we can solve the equations to find the growth rate f.

3.13 Magnification bias

It is well-known that light ray paths experience deflections by the intervening matter distribution lying on the l.o.s direction. This induces distortions in the images of distant objects; such distortions, in the weak lensing limit, are usually decomposed into a 'convergence' κ and a 'shear' γ. The former—a surface mass density integrated along the l.o.s—is responsible for changing the apparent size of a distant galaxy's image, whilst the latter—a complex, spin-2 quantity—stretches an observed galaxy's shape in different directions, making for instance ellipses out of circles (see Clarkson, 2016, for some beautiful and intuitive illustrations of lensing distortions). In turn, convergence and shear are jointly responsible for the magnification,

$$\mathcal{M} = \left|(1-\kappa)^2 - |\gamma|^2\right|^{-1}. \tag{3.116}$$

Cosmic magnification has been first measured by cross-correlating high-redshift quasars with the low-redshift galaxies observed by the Sloan Digital Sky Survey (Scranton et al., 2005), and later with galaxy-dust and galaxy-mass correlations by Ménard et al., 2010. The same effect was detected with normal galaxy samples using the Canada-France-Hawaii-Telescope Legacy Survey measurements (Hildebrandt, H., van Waerbeke, L., and Erben, T., 2009). Furthermore, the magnification bias has been proposed as a probe for the investigation of the primordial magnetic fields (Camera, Fedeli, and Moscardini, 2014).

Besides being a lensing observable per se (e.g. Van Waerbeke, 2010), magnification contributes to the observed correlation of galaxy number counts (Yoo, 2010; Challinor and Lewis, 2011b; Bonvin and Durrer, 2011). The effect of magnification on the observed clustering is due to foreground galaxies effectively acting as lenses for sources in the background. On the one hand, images of a fixed set of sources are distributed over a larger solid angle, thus reducing the number density by a factor $\mathcal{M}^{-1}$. On the other hand, the magnification allows for the observation of fainter sources, as the flux threshold is likewise lowered by the $\mathcal{M}^{-1}$ factor. Now, if $N_{\rm g}$ is the *comoving* number density of galaxies above a certain flux threshold F^* (or, equivalently, below some magnitude threshold m^*), we can define,

$$\mathcal{Q} = -\left.\frac{\partial \ln N_{\rm g}}{\partial \ln F}\right|_{F^*} = \frac{5}{2}\left.\frac{\partial \log_{10} N_{\rm g}}{\partial m}\right|_{m^*}. \tag{3.117}$$

Hence, in the weak lensing regime where $\mathcal{M} \approx 1 + 2\kappa$, it can be seen that the fluctuations in galaxy number counts, $\delta_{\rm g}$, get a further contribution from lensing. This is modulated by $\mathcal{Q}$, for which reason is called 'magnification bias'.[1] Specifically

[1] An alternative notation is also known in the literature, with $s = 2\mathcal{Q}/5$.

the corrected galaxy density contrast (in comoving-synchronous gauge) is,

$$\delta_g = b\,\delta_m + f\mu^2\delta_m + 2(\mathcal{Q}-1)\kappa, \tag{3.118}$$

The first term in Equation 3.118 is the usual Newtonian density fluctuations, the second term is RSD, and the last is the magnification contribution. According to the convergence definition (Bartelmann and Schneider, 2001), at a lensed direction $\boldsymbol{\theta}$ we have:

$$\kappa(\boldsymbol{\theta}) = \frac{1}{c^2}\int_0^\infty \chi d\chi \widetilde{n}^i(\chi)\nabla_\perp^2\Phi, \tag{3.119}$$

where $\nabla_\perp^2\Phi$ the two-dimensional Laplacian of the gravitational potential in the transverse direction and $\widetilde{n}^i(\chi)$ reading:

$$\widetilde{n}^i(\chi) = \int_\chi^\infty d\chi' \frac{\chi'-\chi}{\chi'} n^i(\chi'), \tag{3.120}$$

which is often called the lensing efficiency function with $n^i(\chi)$ the number of sources in a redshift bin i. After inserting the Poisson equation Equation 3.20 and considering that the mean density is $\bar{\rho} = \frac{3H_o^2\Omega_m}{8\pi G}a^{-3}$ we finally have:

$$\kappa(\boldsymbol{\theta}) = \frac{3H_o^2\Omega_m}{2c^2}\int_0^\infty \chi d\chi [1+z(\chi)]\widetilde{n}(\chi)\delta(\chi,\boldsymbol{\theta}). \tag{3.121}$$

Thus, the magnification bias term can take the form:

$$2(\mathcal{Q}-1)\kappa(\boldsymbol{\theta}) = (\mathcal{Q}-1)\frac{3H_o^2\Omega_m}{c^2}\int_0^\infty \chi d\chi [1+z(\chi)]\widetilde{n}(\chi)\delta(\chi,\boldsymbol{\theta}). \tag{3.122}$$

3.14 The spherical-harmonics power spectrum

The spherical-harmonics expansion of the matter fluctuations at a given position $\hat{\mathbf{n}}$ on the sky and redshift z is:

$$\delta(\mathbf{r}) = \sum_{\ell=0}^{\infty}\sum_{m=-\ell}^{\ell} g_{\ell,m}(z)Y_{\ell,m}(\hat{\mathbf{n}}), \tag{3.123}$$

and multiplying with the spherical harmonic conjugate, while integrating over the full assuming orthogonality, we get:

$$\delta_{\ell\ell'}\delta_{mm'} = \int d\boldsymbol{\Omega} Y_{\ell,m}(\hat{\mathbf{n}})Y^*{}_{\ell',m'}(\hat{\mathbf{n}}), \tag{3.124}$$

with $d\boldsymbol{\Omega}$ the solid angle at $\hat{\mathbf{n}}$. Then the density fluctuations harmonic coefficients become:

$$g_{\ell,m}(z) = \int d\boldsymbol{\Omega} Y^*{}_{\ell',m'}(\hat{\mathbf{n}})\delta(\mathbf{r}). \tag{3.125}$$

Since the density fluctuations are expanded in Fourier-space, this identity holds:

$$e^{i\mathbf{k}\cdot\mathbf{r}} = e^{ik\mu\chi} = \sum_{\ell=0} i^{\ell}(2\ell+1)P_{\ell}(\mu)j_{\ell}(k\chi), \tag{3.126}$$

with j_ℓ the spherical Bessel function of order ℓ. Inserting in Equation 3.125 the coefficients become:

$$g_{\ell,m}(z) = \frac{1}{(2\pi)^3}\int\int d\mathbf{k}d\mathbf{\Omega}Y^*{}_{\ell,m}(\hat{\mathbf{n}})\delta(\mathbf{k})\sum_{\ell'=0} i^{\ell'}(2\ell'+1)P_{\ell'}(\mu)j_{\ell'}(k\chi), \tag{3.127}$$

which can be further simplified to

$$g_{\ell,m}(z) = \frac{i^{\ell}}{2\pi^2}\int d\mathbf{k}\delta(\mathbf{k})Y^*{}_{\ell,m}(\hat{\mathbf{n}})j_{\ell}(k\chi), \tag{3.128}$$

$$g^*{}_{\ell,m}(z) = \frac{(-i)^{\ell}}{2\pi^2}\int d\mathbf{k}\delta(\mathbf{k})Y_{\ell,m}(\hat{\mathbf{n}})j_{\ell}(k\chi), \tag{3.129}$$

under the property of the Legendre Polynomial:

$$\int d\mathbf{\Omega}Y^*{}_{\ell,m}(\hat{\mathbf{n}})P'_{\ell}(\mu) = \frac{4\pi Y^*{}_{\ell,m}(\hat{\mathbf{n}})}{2\ell+1}\delta_{\ell\ell'}. \tag{3.130}$$

The spherical-harmonics power spectrum is defined as:

$$\langle g_{\ell,m}(z_i)g^*{}_{\ell,m}(z_j)\rangle = \delta_{\ell,\ell'}\delta_{m,m'}C_{\ell}(z_i,z_j), \tag{3.131}$$

and substituting Equation 3.128 and Equation 3.129 we get:

$$\langle g_{\ell,m}(z_i)g^*{}_{\ell',m'}(z_j)\rangle = \frac{i^{\ell}(-i)^{\ell'}}{(2\pi^2)^2}\int\int d\mathbf{k}d\mathbf{k}'Y_{\ell,m}(\hat{\mathbf{n}})Y^*{}_{\ell',m'}(\hat{\mathbf{n}}') \cdot\langle\delta(\mathbf{k})\delta^*(\mathbf{k}')\rangle j_{\ell}(k\chi(z_i))j_{\ell'}(k\chi(z_j)). \tag{3.132}$$

Instead of using δ which are the matter fluctuations, we are interested in the galaxy density fluctuations following $\delta_g = b\delta$. Therefore, we can imagine a 2D radial projection $\delta_g^{2D}(z,\hat{\mathbf{n}})$ which is connected to the 3D galaxy density field $\delta_g(z,\hat{\mathbf{n}})$ as:

$$\delta_g^{2D}(z_i,\hat{\mathbf{n}}) = \int dz n^i(z)\delta_g(z,\hat{\mathbf{n}}) = \int d\chi n^i(\chi)\delta_g(\chi,\hat{\mathbf{n}}), \tag{3.133}$$

where $n^i(\chi)\mathrm{d}\chi = n^i(z)\mathrm{d}z$ and $\int \mathrm{d}z\, n^i(z) = 1$ hold. It is convenient to rewrite Equation 3.76 as:

$$\delta(k,z) = C\cdot K(k,z)\cdot k^{1/2}\cdot\mathcal{P}_{\zeta}(k), \tag{3.134}$$

with C a new constant containing many constants, $K(k,z) = T(k)D(z)$ and the primordial power spectrum is now defined as $\mathcal{P}_\zeta(k) = A_s(k/k_0)^{n_s-1}$ with A_s the primordial amplitude parameter and k_0 the pivot scale. The fluctuations of the density field are:

$$\langle \delta(\mathbf{k}, z_i)\delta(\mathbf{k}', z_j)\rangle = (2\pi)^3\delta_D^3(\mathbf{k}-\mathbf{k}')K(\mathbf{k}, z_i)K(\mathbf{k}, z_j)C^2\mathcal{P}_\zeta(k)k, \tag{3.135}$$

and it holds that $\langle \delta_g(\mathbf{k}, z_i)\delta_g(\mathbf{k}', z_j)\rangle = b(z_i)b(z_j)\langle \delta(\mathbf{k}, z_i)\delta(\mathbf{k}', z_j)\rangle$. The result after inserting $\langle \delta_g^{2D}(\mathbf{k}, z_i)\delta_g^{2D}(\mathbf{k}', z_j)\rangle$ and separating the angular and the radial terms in spherical coordinates is:

$$\begin{aligned}\langle g_{\ell m}(z_i)g^*{}_{\ell m}(z_j)\rangle = \frac{2}{\pi}(-i)^\ell i^{\ell'}C^2\int k^3dk\int d\chi b(z_i)n(z_i)K(k,z_i)j_\ell(k\chi(z_i))\\ b(z_j)n(z_j)K(k,z_j)j_{\ell'}(k\chi(z_j))\cdot\mathcal{P}_\zeta(k)\int d\mathbf{\Omega}Y_{\ell,m}(\hat{\mathbf{n}})Y^*{}_{\ell',m'}(\hat{\mathbf{n}}'),\end{aligned} \tag{3.136}$$

and finally with the property of orthogonality and from the definition Equation 3.131 we obtain the 2D tomographic angular power spectra for the galaxy density fluctuations:

$$C_\ell^g(z_i, z_j) = 4\pi C^2\int \mathrm{d}\ln k\,\mathcal{P}_\zeta(k)\mathcal{W}_\ell^g(k; z_i)\mathcal{W}_\ell^g(k; z_j), \tag{3.137}$$

with the new weight function:

$$\mathcal{W}_\ell^{\mathrm{g}}(k; z_i) = \int \mathrm{d}\chi\, n^i(\chi)\mathcal{W}_\ell^{\mathrm{g}}(k,\chi), \tag{3.138}$$

where we have

$$\mathcal{W}_\ell^{\mathrm{g}}(k,\chi) = b(\chi)D(\chi)T(k)j_\ell(k\chi), \tag{3.139}$$

3.14.1 The RSD correction

As we have seen in section 3.12 in redshift-space the observed galaxies are affected by the RSD. Thus, it is natural that this effect propagates to the angular power spectrum of the galaxy number counts. The RSD fluctuations are given by:

$$\delta_{RSD} = f\mu^2\delta_m = -\frac{\partial^2}{\partial^2(k\chi)}f\delta_m, \tag{3.140}$$

and the spherical harmonic coefficient becomes:

$$\begin{aligned} g_{\ell,m}^{RSD}(z) &= -\frac{1}{(2\pi)^3}\int d\mathbf{k}\delta(\mathbf{k})f(z)n(z)\frac{\partial^2}{\partial^2(k\chi)}\int d\mathbf{\Omega}e^{i\mu k\chi}Y^*{}_{\ell,m}(\hat{\mathbf{n}})\\ &= \frac{-i^\ell}{2\pi^2}\int d\mathbf{k}\delta(\mathbf{k})f(z)n(z)j_\ell''(k\chi)Y^*{}_{\ell,m}(\hat{\mathbf{n}}),\end{aligned} \tag{3.141}$$

after expanding the exponential according to Equation 3.126 and the Legendre polynomial property Equation 3.130. The prime denotes derivatives with respect to the argument of the function, viz. $k\chi$. The angular power spectrum for the RSD contribution is:

$$C_\ell^{RSD}(z_i, z_j) = 4\pi C^2 \int \mathrm{d}\ln k\, \mathcal{P}_\zeta(k) \mathcal{W}_\ell^{RSD}(k; z_i) \mathcal{W}_\ell^{RSD}(k; z_j), \tag{3.142}$$

and now the weight function:

$$\mathcal{W}_\ell^{\mathrm{RSD}}(k; z_i) = \int \mathrm{d}\chi\, n^i(\chi) \mathcal{W}_\ell^{\mathrm{RSD}}(k, \chi), \tag{3.143}$$

and

$$\mathcal{W}_\ell^{\mathrm{RSD}}(k, \chi) = f(\chi) D(\chi) T(k) j_\ell''(k\chi). \tag{3.144}$$

3.14.2 The magnification bias correction

We have seen that the magnification bias fluctuations are given by:

$$\delta_{mag} = 2(\mathcal{Q} - 1)\kappa. \tag{3.145}$$

Thus, the spherical-harmonic coefficient after inserting Equation 3.122 has now the form:

$$\begin{aligned} g_{\ell,m}^{mag}(z) &= \frac{1}{(2\pi)^3} \int d\mathbf{k} \delta(\mathbf{k}) (\mathcal{Q}(\chi) - 1) \frac{3{H_o}^2 \Omega_m}{c^2} [1 + z(\chi)] \chi \widetilde{n}(\chi) \int d\mathbf{\Omega} e^{i\mu k\chi} {Y^*}_{\ell,m}(\hat{\mathbf{n}}) \\ &= \frac{i^\ell}{2\pi^2} \int d\mathbf{k} \delta(\mathbf{k}) (\mathcal{Q}(\chi) - 1) \frac{3{H_o}^2 \Omega_m}{c^2} [1 + z(\chi)] \chi \widetilde{n}(\chi) j_\ell(k\chi) {Y^*}_{\ell,m}(\hat{\mathbf{n}}), \end{aligned} \tag{3.146}$$

assuming again the exponential expansion Equation 3.126 and the Legendre polynomial property Equation 3.130. The angular power spectrum of the magnification bias fluctuations is:

$$C_\ell^{mag}(z_i, z_j) = 4\pi C^2 \int \mathrm{d}\ln k\, \mathcal{P}_\zeta(k) \mathcal{W}_\ell^{mag}(k; z_i) \mathcal{W}_\ell^{mag}(k; z_j), \tag{3.147}$$

with the weight function:

$$\mathcal{W}_\ell^{\mathrm{mag}}(k; z_i) = T(k) \int \chi \mathrm{d}\chi\, D(\chi) [\mathcal{Q}(\chi) - 1] \frac{3{H_o}^2 \Omega_m}{c^2} [1 + z(\chi)] \widetilde{n}(\chi) j_\ell(k\chi), \tag{3.148}$$

3.14.3 The total angular power spectrum for galaxy number counts

The galaxy number count angular spectrum on linear scales can be written as

$$C_\ell^{\mathrm{g,tot}}(z_i, z_j) = 4\pi C^2 \int \mathrm{d}\ln k\, \mathcal{P}_\zeta(k) \mathcal{W}_\ell^{\mathrm{g,tot}}(k; z_i) \mathcal{W}_\ell^{\mathrm{g,tot}}(k; z_j), \tag{3.149}$$

with the redshift-integrated kernels given by

$$\mathcal{W}_\ell^{\mathrm{g,tot}}(k; z_i) = T(k) \int \mathrm{d}\chi\, D(\chi) \Big\{ b(\chi) n^i(\chi) j_\ell(k\chi) - f(\chi) n^i(\chi) j_\ell''(k\chi) + [\mathcal{Q}(\chi) - 1]\, w_\ell^{\kappa,i}(k, \chi) j_\ell(k\chi) \Big\}, \tag{3.150}$$

with

$$w_\ell^{\kappa,i}(k, \chi) = \frac{3\Omega_m H_0^2}{c^2} [1 + z(\chi)]\, \chi \tilde{n}^i(\chi) \tag{3.151}$$

the lensing weight for the galaxy redshift distribution in the ith redshift bin, $n^i(\chi)$.

To sum up now, if we compare Equation 3.150 to Equation 3.118, the effect of projecting in harmonic space becomes clear:

- Each different contribution to the fluctuations in the galaxy number density, δ_{g}, is modulated by a peculiar quantity—the bias for the matter density contrast, the growth rate for the RSD, and the magnification bias for the lensing convergence.
- Each contribution is weighted by the galaxy distribution in the redshift bin considered—note that lensing convergence is an integrated effect, weighted by a geometric factor, so that the source redshift distribution does not enter explicitly the third term of Equation 3.138, but is integrated along the line of sight via Equation 3.151.
- Each contribution is projected according to its specific spherical Bessel function—e.g. for RSD it is derived twice, because it is a projected radial derivative.

Chapter 4

The importance of RSD for galaxy number counts

4.1 The angular power spectrum of galaxy number counts

Here, we introduce the main tool of our analysis, i.e. the tomographic angular power spectrum of galaxy number counts in the Limber approximation, for which we include RSD for the first time. To do so, we start from the Fourier-space matter power spectrum, $P(k,z)$, and at the end apply the Limber approximation to the harmonic-space angular power spectrum, $C_\ell^{\rm g}(z_i,z_j)$. We modify modules of the publicly available `CosmoSIS` code. We check the agreement between our approximated spectra and the full solution provided by the `CLASS` Boltzmann solver (see subsection 4.3.1).

4.1.1 The Fourier-space matter power spectrum

The linear matter power spectrum can be written as

$$P_{\rm lin}(k,z) = P_{\rm lin}(k)D^2(z), \tag{4.1}$$

where we also define the present-day linear matter power spectrum as $P_{\rm lin}(k) \equiv P_{\rm lin}(k,z=0)$. Hereafter, we shall limit our analysis to linear scales.

4.1.2 The harmonic-space galaxy angular power spectrum

From Equation 3.150, including up to RSD (no magnification bias correction), the (tomographic) angular power spectrum reads:

$$C_\ell^{\rm g,den+RSD}(z_i,z_j) = 4\pi C^2 \int {\rm d}\ln k\, \mathcal{P}_\zeta(k)\mathcal{W}_\ell^{\rm g,den+RSD}(k;z_i)\mathcal{W}_\ell^{\rm g,den+RSD}(k;z_j), \tag{4.2}$$

with the redshift-integrated kernels given by

$$\mathcal{W}_\ell^{\rm g,den+RSD}(k;z_i) = T(k)\int {\rm d}\chi\, D(\chi)\Big\{b(\chi)n^i(\chi)j_\ell(k\chi) - f(\chi)n^i(\chi)j_\ell''(k\chi)\Big\}, \tag{4.3}$$

As we have already discussed in subsection 3.14.3, the first term in Equation 4.3 is the main contribution to galaxy number density fluctuations, due to density perturbations, whereas the second term encodes RSD.

The computation of angular power spectra as in Equation 4.2 is time expensive and prone to numerical instabilities, due to the integration of highly oscillating spherical Bessel functions. Therefore, the Limber approximation (valid on scales $\ell \gg 1$) is often employed. In this limit, the spherical Bessel functions are proportional to a Dirac Delta,

$$j_\ell(k\chi) \xrightarrow[\ell\gg1]{} \sqrt{\frac{\pi}{2\ell+1}}\delta_{\rm D}\left(\ell+\frac{1}{2}-k\chi\right). \tag{4.4}$$

By inserting this into Equation 4.2, and for now just considering the first term in Equation 4.3, we obtain the well-known expression for the galaxy angular power spectrum in Limber approximation,[1]

$$C^{\rm g,den}_{\ell\gg1}(z_i,z_j) = \int {\rm d}\chi\, \frac{W^i_b(\chi)W^j_b(\chi)}{\chi^2} P_{\rm lin}\left(k=\frac{\ell+1/2}{\chi}\right). \tag{4.5}$$

Since the contribution to galaxy number counts from density fluctuations is modulated by the galaxy bias, we have defined the window function

$$W^i_b(\chi) = n^i(\chi)b(\chi)D(\chi). \tag{4.6}$$

Now, we want to include RSD in the Limber galaxy angular power spectrum. As clear from Equation 4.3, RSD are driven by the growth rate, $f(z)$, we thus introduce a new window function,

$$W^i_f(\chi) = n^i(\chi)f(\chi)D(\chi). \tag{4.7}$$

After some manipulations (see section A.1), and the introduction of a window function for the global 'den+RSD' signal,

$$\begin{aligned} W^i(\chi) = W^i_b(\chi) &+ \frac{2\ell^2+2\ell-1}{(2\ell-1)(2\ell+3)}W^i_f(\chi) \\ &- \frac{(\ell-1)\ell}{(2\ell-1)\sqrt{(2\ell-3)(2\ell+1)}}W^i_f\left(\frac{2\ell-3}{2\ell+1}\chi\right) \\ &- \frac{(\ell+1)(\ell+2)}{(2\ell+3)\sqrt{(2\ell+1)(2\ell+5)}}W^i_f\left(\frac{2\ell+5}{2\ell+1}\chi\right), \end{aligned} \tag{4.8}$$

we eventually get

$$C^{\rm g,den+RSD}_{\ell\gg1}(z_i,z_j) = \int {\rm d}\chi\, \frac{W^i(\chi)W^j(\chi)}{\chi^2} P_{\rm lin}\left(k=\frac{\ell+1/2}{\chi}\right). \tag{4.9}$$

[1] Henceforth, we shall use, in comparisons, 'den+RSD' and 'den' to refer to Equation 4.9 or Equation 4.5, respectively. Otherwise, when no ambiguity arises, $C^{\rm g}_\ell(z_i,z_j)$ will either mean the galaxy angular power spectrum in general, or the most comprehensive case considered in this chapter, viz. 'den+RSD'.

It is instructive to notice how RSD affect the harmonic-space angular power spectrum. As we show in Equation 3.110 the Fourier-space galaxy power spectrum $P_{\rm g}(\boldsymbol{k}, z)$, which is isotropic if we consider density fluctuations only, due to RSD acquires a further dependence on μ, the cosine between the wave-vector $\boldsymbol{k}$ and the l.o.s direction $\hat{\boldsymbol{n}}$. We remind the reader that this translates into a quadrupolar anisotropy pattern, resulting into the well-known squashing of the galaxy power spectrum on large scales and in the direction perpendicular to the line of sight, and, oppositely, into the so-called Finger-of-God effect on nonlinear scales and in the l.o.s direction (see again section 3.12). On the contrary, the net effect of RSD on the harmonic-space angular power spectrum C_ℓ^g is far less straightforward. In this sense, the Limber approximation makes it simpler to understand. If we look at Equation 4.8, we appreciate that RSD effectively shuffle galaxies around among (neighbouring) redshift bins due to the $(2\ell-3)/(2\ell+1)$ and $(2\ell+5)/(2\ell+1)$ factors that modulate χ in the RSD window functions. The reason behind this is the second derivative of the spherical Bessel function in Equation 4.3, in turn coming from RSD being caused by the radial derivative of the galaxies' velocity along the line of sight (see e.g. Bonvin and Durrer, 2011, Section III). As in the case of the Fourier-space galaxy power spectrum discussed above, linear RSD effects are stronger on the largest angular scales, where $(2\ell-3)/(2\ell+1)$ or $(2\ell+5)/(2\ell+1)$ deviate from unity the most. (We remind the reader that we limit our analysis to linear scales, so we are not interested in modelling Finger-of-God effects.)

4.2 Surveys adopted in the analysis

Here, we present the details of the two surveys adopted to test our pipeline. One survey is a proxy for future photometric imaging experiments, and the other is a representative of planned spectroscopic observational campaigns. Better to foresee the potentiality of our pipeline when applied to oncoming data from cosmological galaxy surveys, we decide to study both the cases of optical/near-infrared and radio observations.

To model redshift binning in spectroscopic and photometric redshift surveys, we here assume top-hat and Gaussian bins, respectively. This is clearly a simplification, but it is enough to capture the main features of both observational strategies. On the one hand, the exquisite redshift accuracy of spectroscopic measurements allows for separating galaxies into sharp, non-overlapping redshift slices. This is implemented here by the top-hat bins, to which we had a degree of smoothing to stabilise numerical integration over the bin. On the other hand, photometric redshift estimation is far less accurate than spectroscopy, and it usually results into a PDF $p(z_{\rm ph}|z)$ for each galaxy, representing the probability of having estimated a photometric redshift, $z_{\rm ph}$, given the galaxy's true redshift, z. Although one could, in principle, use each galaxy separately (see e.g. Kitching and Heavens, 2011), it is customary to combine the various PDFs into a certain number of redshift bins, which look much broader than

spectroscopic ones, and which often overlap each other to a greater or lesser extent, depending on photometric redshift uncertainties. Without any loss of generality, we follow the literature and model this effect by implementing Gaussian redshift bins with a redshift-dependent (monotonically-increasing) width.

For a generic survey X, we shall denote: the total redshift distribution of sources by $n_X(z)$; the distribution of sources in the ith redshift bin by $n_X^i(z)$; and the (angular) number density of galaxies by

$$\bar{n}_X^i = \int \mathrm{d}z\, n_X^i(z), \tag{4.10}$$

so that the total number density of galaxies is $\bar{n}_X = \sum_i \bar{n}_X^i$.[2] The redshift distributions for the two surveys under investigation, and the two binning strategies are shown in Figure 4.1, and will be discussed in the following sections.

4.2.1 Photometric galaxy survey

As a proxy of an optical/near-infrared photometric galaxy survey, we adopt the specifications of a *Euclid*-like experiment (Laureijs et al., 2011; Amendola et al., 2013; Amendola et al., 2018). The *Euclid* satellite will be launched in 2022 and will probe $15,000\,\mathrm{deg}^2$ of the sky for weak lensing and photometric galaxy clustering in the redshift range $0 < z \lesssim 2.5$, detecting $\bar{n}_{\mathrm{Euc}} = 30$ galaxies per square arcminute. The source redshift distribution and the redshift-dependent galaxy bias are given by (Amendola et al., 2013)

$$n_{\mathrm{Euc}}(z) = \frac{3\bar{n}_{\mathrm{Euc}}}{2z_0^3} z^2 \exp\left[-\left(\frac{z}{z_0}\right)^{3/2}\right] \mathrm{arcmin}^{-2}, \tag{4.11}$$

$$b_{\mathrm{Euc}}(z) = \alpha_{\mathrm{Euc}}(1+z)^{\beta_{\mathrm{Euc}}}, \tag{4.12}$$

where $z_0 = 0.9/\sqrt{2}$, 0.9 being the mean redshift of the survey, $\alpha_{\mathrm{Euc}} = 1$, and $\beta_{\mathrm{Euc}} = 0.5$. In Figure 4.1 (left panels) we present the equi-spaced and equi-populated binned $n_{\mathrm{Euc}}(z)$, implementing photometric redshift errors. We use photometric uncertainties in redshift following Ma, Hu, and Huterer (2005). That is, the given true redshift distribution of galaxies inside the ith photometric redshift bin with photometric redshift estimate z_{ph} in the range $z_{\mathrm{ph}}^i < z_{\mathrm{ph}} < z_{\mathrm{ph}}^{i+1}$ can be expressed as

$$n_{\mathrm{Euc}}^i(z) = \int_{z_{\mathrm{ph}}^i}^{z_{\mathrm{ph}}^{i+1}} \mathrm{d}z_{\mathrm{ph}}\, n_{\mathrm{Euc}}(z)\, p(z_{\mathrm{ph}}|z), \tag{4.13}$$

[2] We remind the reader that the term $n^i(z)$ appearing in Equation 3.138, Equation 4.6, and Equation 4.7 is normalised, meaning that it in fact corresponds to $n_X^i(z)/\bar{n}_X^i$.

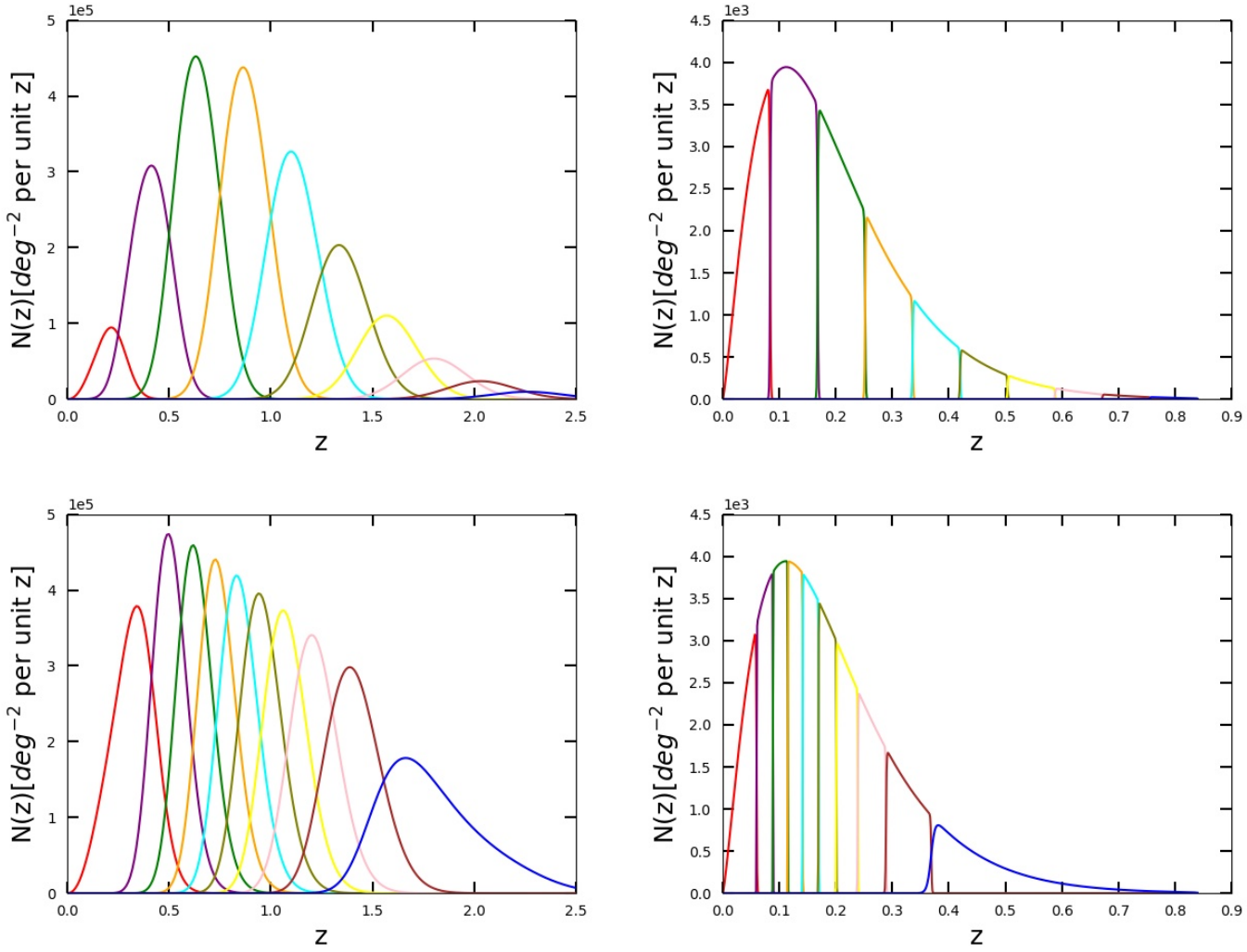

FIGURE 4.1: Galaxy redshift distributions for the *Euclid*-like photometric galaxy survey (left panels) and the SKA1 HI-line galaxy survey (right panels). Top and bottom panels respectively show equi-spaced and equi-populated bins.

where $p(z_{\rm ph}|z)$ is the probability distribution of photometric redshift estimates $z_{\rm ph}$ given true redshifts z. More specifically, we adopt a probability distribution of Gaussian form,

$$p(z_{\rm ph}|z) = \frac{1}{\sqrt{2\pi}\sigma_z} \exp\left[-\frac{\left(z - z_{\rm ph} - \delta z\right)^2}{2\sigma_z^2}\right], \tag{4.14}$$

with δz the redshift bias (set to zero in our case), and $\sigma_z = 0.05(1+z)$ the scatter of the photometric redshift estimate with respect to the true redshift value— a typical value in photometric redshift measurements (see e.g. Hoyle et al., 2018).

4.2.2 Spectroscopic galaxy survey

As a representative of oncoming cosmological experiments operating at radio frequencies, we choose a spectroscopic HI galaxy survey performed by SKA1 (Maartens

et al., 2015; Abdalla et al., 2015; Bacon et al., 2018), which will be able to access even very large angular scales (Camera, Santos, and Maartens, 2015a; Camera, Maartens, and Santos, 2015a). Such a survey with this large radio telescope will probe 5000 $\deg^2$, detecting $\bar{n}_{\rm SKA} = 0.28$ galaxies per square arcminute (Yahya et al., 2015, 'reference' case). The survey specifications adopted in this work for the range $0 < z \lesssim 0.9$ are

$$n_{\rm SKA}(z) = 10^{5.438}\, z^{1.332}\, \mathrm{e}^{-11.837z}\, \deg^{-2}, \tag{4.15}$$

$$b_{\rm SKA}(z) = \alpha_{\rm SKA} \exp\left(\beta_{\rm SKA} z\right), \tag{4.16}$$

with $\alpha_{\rm SKA} = 0.625$ and $\beta_{\rm SKA} = 0.881$. Similarly to the case of *Euclid*, we consider equi-spaced and equi-populated bins as shown in Figure 4.1 (right panels). In both scenarios we choose 10 bins. For the top-hat bins, we define a smoothed top-hat window function (the same functional form is implemented in `CLASS`), i.e.

$$w_{\rm SKA}(z) = \frac{1}{2}\left\{1 - \tanh\left[\frac{|z-\bar{z}| - \sigma_{\rm SKA1}}{r\sigma_{\rm SKA}}\right]\right\}, \tag{4.17}$$

where $\bar{z}$ is the central value of the bin, $\sigma_{\rm SKA}$ is half of the top-hat width, and r is the smoothing edge factor, with a realist value of 0.03.

4.3 Pipeline implementation

Here we describe the various ingredients and tests performed to implement and validate our pipeline.

4.3.1 Validation of the code

Here, we perform some tests to validate the expressions derived in subsection 4.1.2, namely the agreement between the Limber approximation in Equation 4.9 and the full solution involving the double integral and the spherical Bessel functions of Equation 4.2. We consider four window functions for the angular power spectrum. Our code is validated against the results of `CLASS`, where the Limber approximation is applied for multipoles $\ell \geq 100$, but we also cross-checked that our results do not change if we enforce `CLASS` never to use the Limber approximation.

Consequently, these cases are considered to be indicative of the binning scenarios for *Euclid* and SKA1 as shown in subsection 4.2.1 and subsection 4.2.2 and are chosen as templates to validate the performance of the code.

For the sake of simplicity, let us assume that we have only one redshift bin covering the range $0 < z \leq 2$ and peaking at $\bar{z} = 1$. We can define a Gaussian distribution of sources in the bin as

$$n_{\rm G}(z) = \frac{1}{\sigma_{\rm G}\sqrt{2\pi}} \exp\left[-\frac{(z-\bar{z})^2}{2\sigma_{\rm G}^2}\right], \tag{4.18}$$

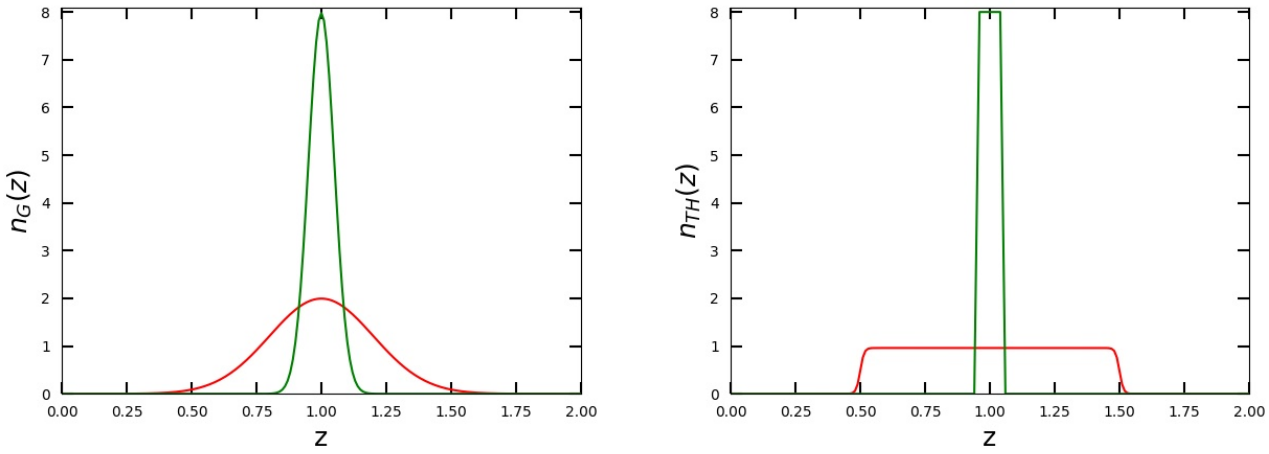

FIGURE 4.2: Various window functions: broad and narrow Gaussian (left panel), and broad and narrow smoothed top-hat (right panel).

where σ_G is the width of the distribution. We consider both a narrow and a broad bin by setting $\sigma_G = 0.05$ and $\sigma_G = 0.2$, respectively. Such a Gaussian bin is shown in the left panel of Figure 4.2.

Similarly, we adopt Eq. 4.17 where now σ_{TH} is half of the top-hat width, and r is the smoothing edge factor. Again, we consider both a narrow and a broad redshift bin, respectively defined by $\{\sigma_{TH}, r\} = \{0.05, 0.003\}$ and $\{0.5, 0.03\}$. They are presented in the right panel of Figure 4.2.

We check our code performance against the `CLASS` for the case of density perturbations only in Figure 4.3 (top panels) for the broad and narrow Gaussian and top-hat bins. Similarly, the convergence is shown for the case of density and RSD as seen in Figure 4.3 (bottom panels).

4.3.2 Multipole range

Since the Limber approximation is not a good approximation on large angular scales, we set the minimum multipole in our analysis, ℓ_{min}, by performing the same comparison as in Figure 4.3 for each bin pair, binning scenario, and survey. For the rest of this analysis, we consider the convergence between Limber-approximated spectra and the full solution of Equation 4.2 met when the relative error between `CosmoSIS` and `CLASS` is below 5%. This is a reasonable choice, since such a percentage difference between correct and approximated angular power spectra is well within the standard deviation of the signal (see section 5.4 for the covariance matrix). The result of this is presented in Table 4.1.

Generally, it is evident that there is a trend of increasing ℓ_{min} with redshift, apart from the equi-populated bins for SKA1, to whose highest z bin(s) correspond a lower ℓ_{min}. This happens because the broader the top-hat bin, the more accurate the Limber approximation (see also the right panels of Fig. 4.3). Interestingly, we also find that in the case of the smoother, photometric redshift bins of the *Euclid*-like survey, the

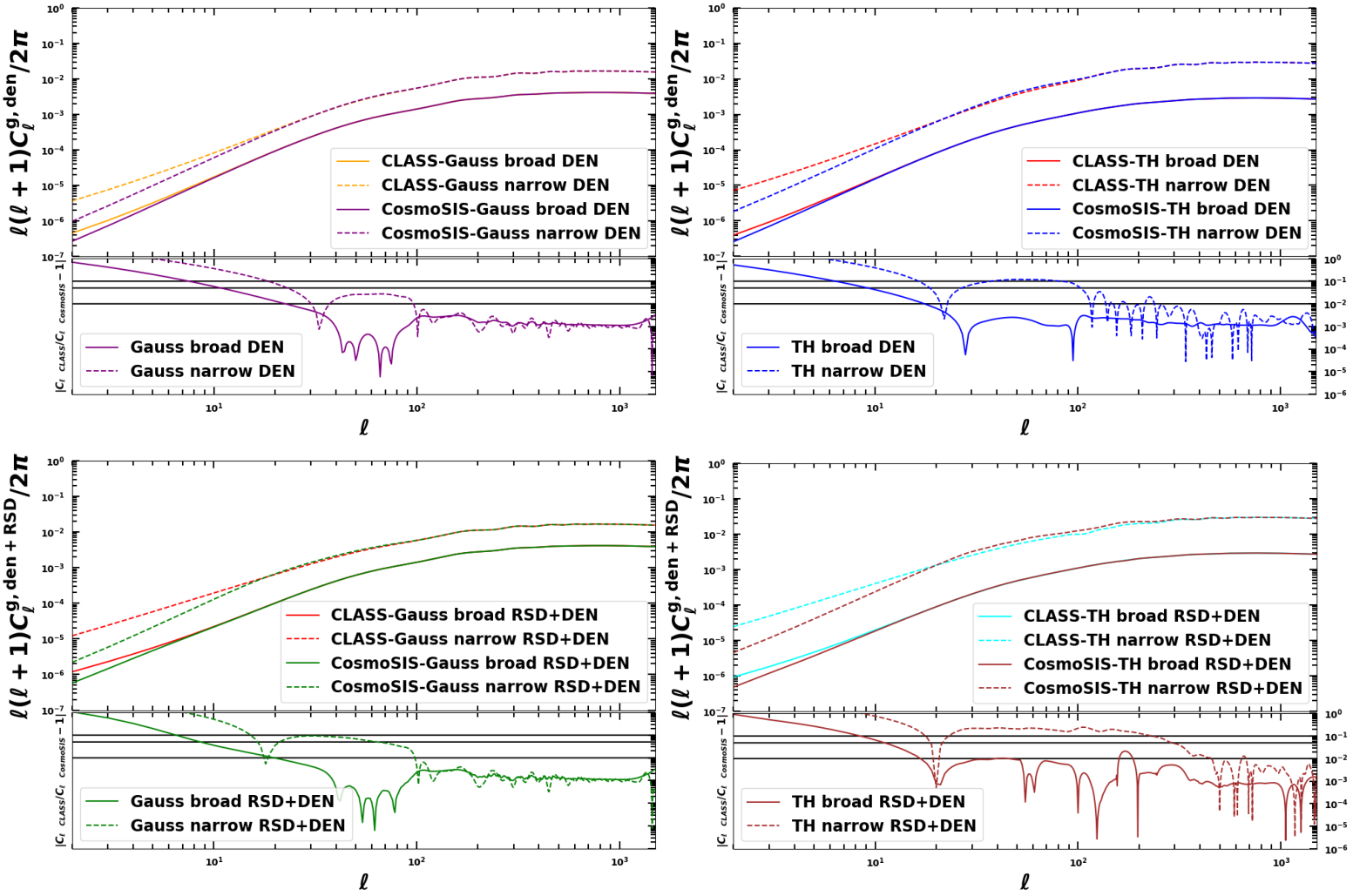

FIGURE 4.3: Code comparison for the window functions (solid lines: broad bins; dashed lines: narrow bins). Top and bottom panels respectively refer to 'den' and 'den+RSD', with Gaussian (top-hat) window functions on the left (right). In each panel, the bottom plot shows the relative error due to Limber approximation as implemented in our modified version of `CosmoSIS`, with respect to the full solution of `CLASS`; the three black solid lines correspond to 10%, 5% and 1% relative errors from top to bottom, respectively.

TABLE 4.1: Mininum and maximum multipoles for the two binning strategies. The former are set so that the relative error between angular spectra computed with `CosmoSIS` and `CLASS` is below 5%. The latter follow $\ell_{\rm max} = \chi(\bar{z}_i)k_{\rm max}$ in redshift bin i centred on $\bar{z}_i$.

Equi-spaced bins						Equi-populated bins					
Euclid			SKA1			*Euclid*			SKA1		
$\ell_{\rm min}$		$\ell_{\rm max}$	$\ell_{\rm min}$		$\ell_{\rm max}$	$\ell_{\rm min}$		$\ell_{\rm max}$	$\ell_{\rm min}$		$\ell_{\rm max}$
den	den+RSD		den	den+RSD		den	den+RSD		den	den+RSD	
2	2	133	3	13	45	4	3	348	2	7	32
8	6	373	1	13	134	10	7	480	7	30	80
12	9	581	14	26	218	12	9	576	11	78	109
16	11	759	29	40	299	15	10	659	13	77	136
22	13	913	33	60	375	17	12	733	15	80	164
28	17	1046	43	70	448	18	13	806	19	80	194
32	20	1162	63	73	518	20	14	880	22	91	228
36	22	1265	60	101	584	22	15	957	26	82	270
40	25	1356	70	110	647	24	17	1054	30	65	331
50	30	1437	80	120	707	25	19	1181	11	44	564

agreement between Limber and non-Limber spectra extends to larger scales when RSD are included, than what happens with density perturbations only.

Additionally, we want to find the upper limits of the multipole range for each redshift bin so that we safely remain within the linear regime. This corresponds to setting the largest angular scale, $\ell_{\rm max}$, corresponding to the maximum wavenumber before entering the nonlinear regime, $k_{\rm max}$. This is estimated through the rms fluctuations of the total mass density in spheres of radius R at $z = 0$,

$$\sigma_M^2(R) = \int \frac{{\rm d}k}{2\pi^2}\, k^2 P_{\rm lin}(k) \left[\frac{3j_1(kR)}{kR}\right]^2 . \tag{4.19}$$

We choose $k_{\rm max}$ such that $\sigma_M^2(R_{\rm min}) = 1$ and $k_{\rm max} = \pi/(2R_{\rm min})$. Since we are considering multipoles $\ell \gg 1$, where the Limber approximation is a good approximation, we simply set $\ell_{\rm max} = k_{\rm max}\chi(\bar{z}_i)$, with $\bar{z}_i$ the centre of the ith redshift bin. We find $k_{\rm max} = 0.25\,h\,{\rm Mpc}^{-1}$ for our fiducial model.

4.3.3 Likelihood

To construct the likelihood of the signal, we start from the Gaussian covariance matrix implemented in `CosmoSIS`, $\mathbf{\Gamma}_{\ell\ell'}$, whose entries are

$$\Gamma^{ij,kl}_{\ell\ell'} = \frac{\delta^{\ell\ell'}_{\rm K}}{2\ell\Delta\ell f_{\rm sky}} \left[\widetilde{C}^{\rm g}_\ell(z_i,z_k)\widetilde{C}^{\rm g}_\ell(z_j,z_l) + \widetilde{C}^{\rm g}_\ell(z_i,z_l)\widetilde{C}^{\rm g}_\ell(z_j,z_k)\right], \tag{4.20}$$

where $\Delta\ell$ is the width of the multipole bin, $f_{\rm sky}$ the sky fraction covered by the survey, $\delta_{\rm K}$ is the Kronecker symbol, and the observed signal is

$$\widetilde{C}^{\rm g}_{\ell}(z_i, z_j) = C^{\rm g}_{\ell}(z_i, z_j) + \frac{\delta^{ij}_{\rm K}}{\bar{n}^i}, \tag{4.21}$$

with $\bar{n}^i$ defined in Equation 4.10. Then, for N_z redshift bins and $N_\ell = 20$ multipole bins, we can write the data vector as

$$\boldsymbol{d}_\ell = \Big\{ \underbrace{C^{\rm g}_{\ell_{\rm min}}(z_1, z_1), \ldots, C^{\rm g}_{\ell_{\rm min}}(z_1, z_{N_z})}_{\substack{\text{Auto- and cross-bin spectra at } \ell_{\rm min} \\ \text{between bin 1 and all other } N_z \text{ bins.}}}, \underbrace{C^{\rm g}_{\ell_{\rm min}}(z_2, z_2), \ldots, C^{\rm g}_{\ell_{\rm min}}(z_2, z_{N_z})}_{\substack{\text{Auto- and cross-bin spectra at } \ell_{\rm min} \\ \text{between bin 2 and all other } N_z - 1 \text{ bins.}}},$$
$$C^{\rm g}_{\ell_{\rm min}+1}(z_1, z_1), \ldots, \underbrace{C^{\rm g}_{\ell_{\rm max}}(z_{N_z}, z_{N_z})}_{\substack{\text{Last of all the } N_\ell N_z(N_z+1)/2 \\ \text{data points.}}} \Big\}, \tag{4.22}$$

and then build the Gaussian log-likelihood as

$$-2\ln L = \sum_{\ell,\ell'=\ell_{\rm min}}^{\ell_{\rm max}} \Big\{ \ln\left[2\pi \det\left(\boldsymbol{\Gamma}_{\ell\ell'}\right)\right] + \left[\boldsymbol{d}_\ell - \boldsymbol{t}_\ell(\boldsymbol{\theta})\right]^{\rm T} \left(\boldsymbol{\Gamma}_{\ell\ell'}\right)^{-1} \left[\boldsymbol{d}_\ell - \boldsymbol{t}_\ell(\boldsymbol{\theta})\right] \Big\}. \tag{4.23}$$

Here, $\boldsymbol{t}_\ell(\boldsymbol{\theta})$ is the vector of the theoretical prediction based on a cosmological model defined by its cosmological parameters, whose values are stored in the parameter vector $\boldsymbol{\theta}$; the superscripts 'T' and '-1' denote matrix transposition and inversion, respectively. This likelihood function is maximised for a given combination of values of the model parameters. In the current analysis, the Gaussian covariance matrix of Equation 4.20[3] is assumed to be independent on the parameters, and therefore the normalisation term of Equation 4.23 can be ignored.

4.3.4 Binning strategy

To optimise our method, we adopt two binning strategies. First, we consider bins of the same size in redshift space (hereafter, 'equi-spaced' bins), and then the case of bins with an equal number of galaxies in each ('equi-populated' bins). To choose among the two binning strategies presented in the previous section, i.e. equi-spaced

[3]Note that the denominator of Equation 4.20 should actually read $(2\ell + 1)$, and not 2ℓ as reported in Joachimi and Bridle (2010). Such a difference, however, is negligible for $\ell \gg 1$ where the Limber approximation holds true. Moreover, we are here interested in comparing two methods (i.e. fitting the data with or without RSD), so the absence of the $+1$ factor does not affect the validity of our results.

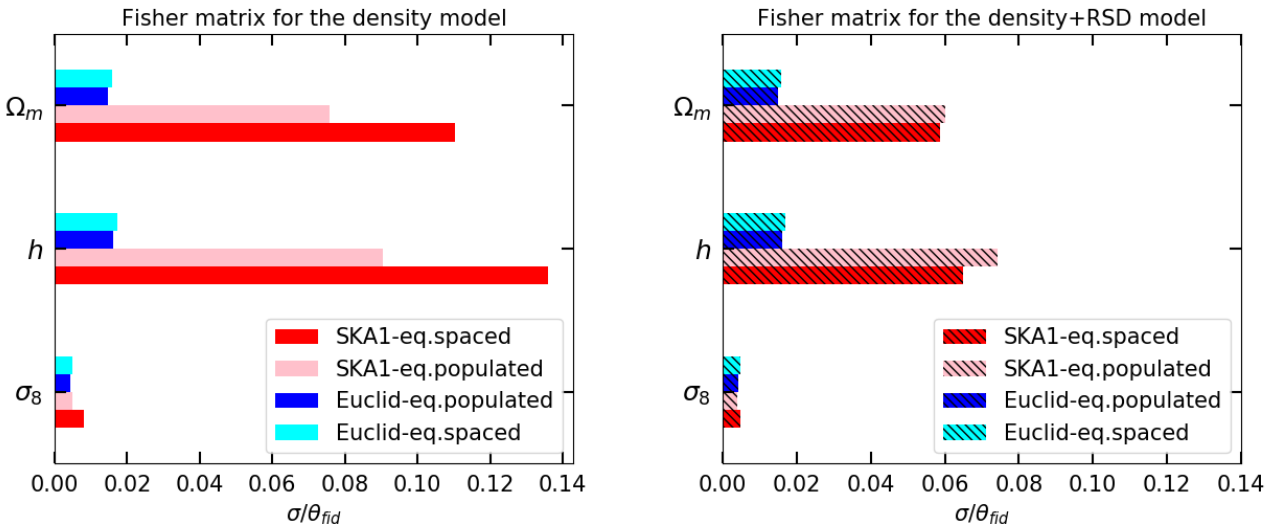

FIGURE 4.4: Marginal 1σ Fisher matrix errors divided by the fiducial parameter value, for the two binning scenarios and the two proxy surveys. *Left panel:* Model with density fluctuations only. *Right panel:* Model with density fluctuations and RSD.

vs equi-populated bins, we perform a preliminary Fisher matrix analysis (Tegmark, Taylor, and Heavens, 1997). Assuming a Gaussian likelihood for the cosmological parameters of interest, we can define the Fisher matrix $\mathbf{F}$ with entries

$$F_{\alpha\beta} = \sum_{\ell,\ell'=\ell_{\rm min}}^{\ell_{\rm max}} \frac{\partial C_\ell^{\rm g}(z_i,z_j)}{\partial\theta_\alpha} \left(\mathbf{\Gamma}_{\ell\ell'}^{-1}\right)^{ij,kl} \frac{\partial C_{\ell'}^{\rm g}(z_k,z_l)}{\partial\theta_\beta}, \tag{4.24}$$

where θ_α are the elements of the parameter vector $\boldsymbol{\theta} = \{\Omega_{\rm m}, h, \sigma_8\}$.

We forecast constraints on cosmological parameters by computing the Fisher matrix (in the appropriate multipole range) for both binning strategies, as well as for both $C_{\ell\gg1}^{\rm g,den}$ and $C_{\ell\gg1}^{\rm g,den+RSD}$. (Note that the covariance matrix in Equation 4.24 is always the correct one, i.e. it includes both density fluctuations and RSD.) Then, we compare the results. In Figure 4.4 we show the relative marginal errors on $\{\Omega_{\rm m}, h, \sigma_8\}$ for all the cases considered. Constraints for *Euclid* are always marginally tighter for equi-populated bins. In the case of SKA1, however, both binning strategies give almost equivalent results for the 'den+RSD' model, whilst equi-populated bins yield tighter constraints for the 'den' case. Overall, it is evident that the *Euclid*-like survey is more constraining compared to SKA1. In order to investigate this, we calculate the cumulative signal-to-noise ratio (SNR) for the input reference cosmology,

$$\text{SNR} = \sqrt{\sum_{\ell,\ell'=\ell_{\rm min}}^{\ell_{\rm max}} C_\ell^{\rm g}(z_i,z_j) \left(\mathbf{\Gamma}_{\ell\ell'}^{-1}\right)^{ij,kl} C_{\ell'}^{\rm g}(z_k,z_l)}. \tag{4.25}$$

In Figure 4.5, we present the cumulative SNR for *Euclid* (red) and SKA1 (blue) with the 'den-only' and 'den+RSD' models (dashed and solid lines respectively) in

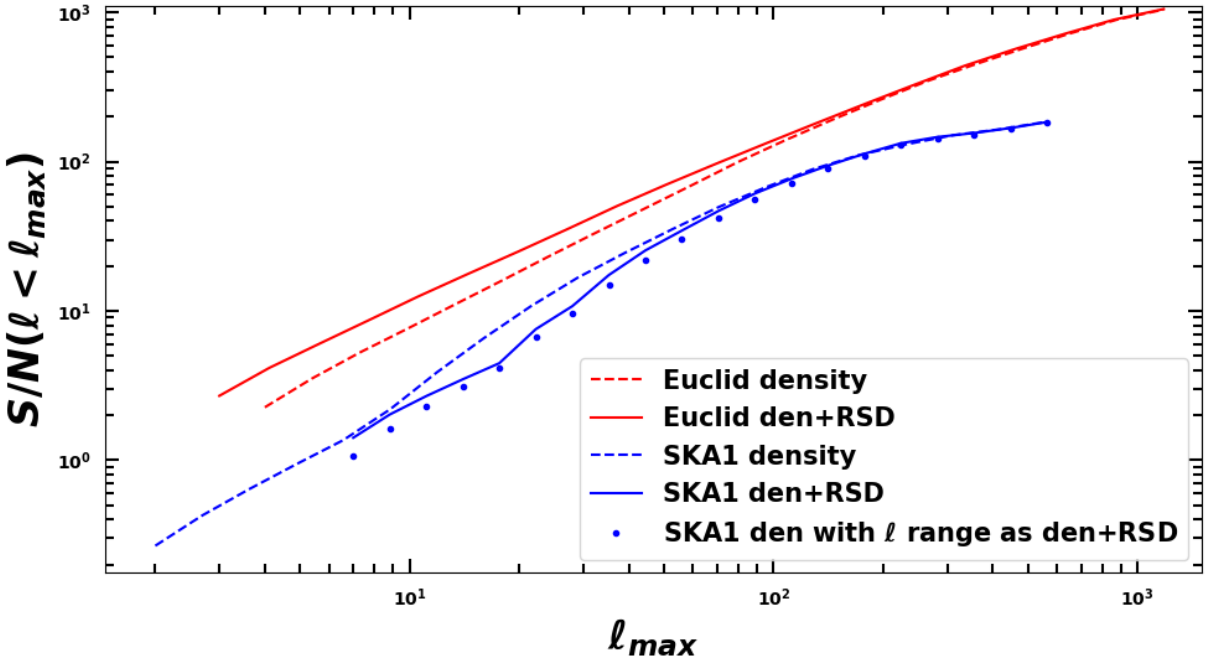

FIGURE 4.5: Cumulative SNR as a function of the maximum multipole included in the analysis, $\ell_{\rm max}$, for *Euclid* and SKA1 equi-populated bins (red and blue curves, respectively) and the two models considered, i.e. den-only (dashed lines) and den+RSD (solid lines). The blue, dotted curve refers to the SKA1 SNR for density perturbations only in the case where we compute it in the same multipole range as for den+RSD.

the equi-populated scenario (this applies to the equi-spaced case as well). If we ignore for a while the different cumulative SNR between these two models within the same experiment, it is clear that generally the SNR for *Euclid* is always greater than that of SKA1. The reason for this, is that *Euclid* as seen in Table 4.1 extends to higher $\ell_{\rm max}$values and also the sky fraction $f_{\rm sky}$ covered by this survey is three times that of SKA1.These two factors minimize the covariance matrix (see again Equation 4.23), yielding to an overall higher SNR. The specific features seen in Figure 4.5 will be discussed in more detail in subsection 4.4.1.

Furthermore, we perform preliminary MCMC tests for both surveys to make clear which binning configuration is computationally cheaper in terms of a faster convergence of the chains. Considering the case of density fluctuations and equi-populated bins, the chains converge quicker compared to equi-spaced bins for all the cases considered, whilst the convergence speed for den+RSD is comparable. Consequently, we conclude that the equi-populated redshift bins are more suitable to be adopted in the extensive and computationally expensive analysis of section 4.4.

TABLE 4.2: Fiducial values and priors of cosmological and nuisance parameters.

Parameter description	Parameter symbol	Fiducial value	Prior type	Prior range
Present-day fractional matter density	$\Omega_{\rm m}$	0.3089	Flat	$[0.1, 0.4]$
Dimensionless Hubble parameter	h	0.6774	Flat	$[0.5, 1.0]$
Amplitude of clustering[‡]	σ_8	0.8159	Flat	$[0.5, 1.2]$
Present-day fractional baryon density	$\Omega_{\rm b}$	0.0486	–	–
Slope of the primordial curvature power spectrum	$n_{\rm s}$	0.9667	–	–
Amplitude of the primordial curvature power spectrum[‡]	$\ln(10^{10} A_{\rm s})$	3.064	–	–
Optical depth to reionisation	$\tau_{\rm re}$	0.066	–	–
Photo-z survey bias amplitude parameter[¶]	$\alpha_{\rm Euc}$	1.0	Flat	$[0.6, 1.4]$
Photo-z survey bias slope parameter[¶]	$\beta_{\rm Euc}$	0.5	Flat	$[0.1, 0.9]$
Spectro-z survey bias amplitude parameter[¶]	$\alpha_{\rm SKA}$	0.625	Flat	$[0.2, 1.0]$
Spectro-z survey bias slope parameter[¶]	$\beta_{\rm SKA}$	0.881	Flat	$[0.5, 1.3]$
Bin-dependent bias amplitude parameters[§]	$b_{{\rm g},i}$	1.0	Flat	$[0.1, 1.9]$

[‡] Adopting the LSS convention, we use σ_8 to parameterise the amplitude of matter fluctuations, thus setting the prior on this parameter rather than on the primordial amplitude parameter, $A_{\rm s}$.
[¶] Parameter varied in the reported prior range only in the 'realistic scenario' of subsection 4.4.2.
[§] A dummy amplitude parameter for each redshift bin of *Euclid* or SKA1 varied in the reported prior range only in the 'conservative scenario' of subsection 4.4.3.

4.4 Results and discussion

Throughout our analysis, in order to constrain the parameters of interest, we applied the Bayesian-based `emcee` sampler (Foreman-Mackey et al., 2013) and `Multinest` (Feroz, Hobson, and Bridges, 2009) interchangeably, depending on which sampling method is optimal/faster for each case. As discussed above, we focus on the set of cosmological parameters $\boldsymbol{\theta} = \{\Omega_{\rm m}, h, \sigma_8\}$. Moreover, we also include a certain number of nuisance parameters, as described in the following three scenarios:

i) An ideal case where we constrain the cosmological parameter set assuming perfect knowledge of the galaxy bias;

ii) A realistic case with two bias nuisance parameters per experiment (see Eqs 4.12 and 4.16);

iii) A conservative case where we include a nuisance parameter per redshift bin, thus allowing for a free redshift evolution of the bias.

Reality is believed to lie between the last two cases. We note again that the procedure we follow is based on the rationale explained in subsection 4.3.4. That is, to create a mock data set where both density fluctuations and RSD are present, and then fit it against either a (wrong) model that ignores RSD, or a (correct) model that includes both density and RSD.

In an analysis where the `emcee` or the `Multinest` sampler is used, both high and the low likelihood areas are sampled, in contrast to the Fisher matrix, which only characterises the likelihood near its peak, assuming it is well approximated by a

Gaussian. With our pipeline we want to explore the multi-dimensional parameter space of the two aforementioned models given the mock data in a Bayesian way. A major point in our analysis is the fact that we construct the mock data and, therefore, have perfect knowledge of the information it encodes. Hence, when we fit the mock data with the correct model, containing exactly the same information as the mock data, we expect this model to fit the data better than the wrong model, where the effect of the RSD in galaxy clustering is neglected. This latter, wrong model may or may not be sufficient to describe the data, depending mostly on the relative importance of signal, cosmic variance, and noise. In case it is proven not to be sufficient, the results will be biased. This bias will manifest as a misplaced peak in the posterior distribution. (Alternatively, it might also happen that the posterior exhibits some degree of bimodality.) In order to avoid referring to best-fit values—which can sometimes be misleading for strongly non-Gaussian posterior distributions—we opt for the means. The results of the pipeline analysis with *Euclid* and SKA1 for the three scenarios discussed above are presented in Figure 4.6, Figure 4.8 and Figure 4.10, respectively. Table 4.3 and Table 4.4 list estimates of the means and 68% marginal errors on each parameter. We discuss these results thoroughly in the following subsections.

4.4.1 Ideal scenario

In Figure 4.6 (top panels) we show the 68% and 95% joint marginal error contours for the Bayesian analysis with *Euclid* on the parameter set $\{\Omega_m, h, \sigma_8\}$. We use priors and fiducial values as given in Table 4.2. These constraints appear quite stringent, and it is clear that, when we fit the mock data with the correct model (in red), the input reference cosmology (white cross) lies well within the 1σ regions of the reconstructed parameter error intervals. On the contrary, if we assume the wrong data model—namely we do not include RSD in the theoretical data vector—it is evident that the reconstructed contours (in grey) are biased with respect to the input cosmology. It is worth noticing that the 2σ regions do not overlap in parameter space. This may seem somewhat unexpected, as it is often assumed that RSD do not matter when one deals with photometric galaxy surveys. However, this finding, which represents one of the main results of our work, is also in agreement with previous literature focussed on galaxy clustering including RSD for photometric redshifts (e.g. Makarov et al., 2007; Blake et al., 2007; Crocce, Cabré, and Gaztañaga, 2011). For instance, Ross, Percival, and Nock (2010) proposed a new binning scheme based on galaxy pair centres rather than the galaxy positions, to alleviate the anisotropic RSD on the projected galaxy two-point function. This is more evident in Figure 4.7, where the estimated mean for the incomplete model (red bullet point) is more than 1σ away (red, dashed line) from the input values of parameters $\{\Omega_m, \sigma_8\}$, shown as vertical dashed black lines.

Similarly, in Figure 4.6 (bottom panels) we present the constraints on the parameters from the SKA1. In particular, SKA1 yields weaker constraints than *Euclid* due to the lower SNR (see Figure 4.5) , as discussed at the end of subsection 4.3.4, namely

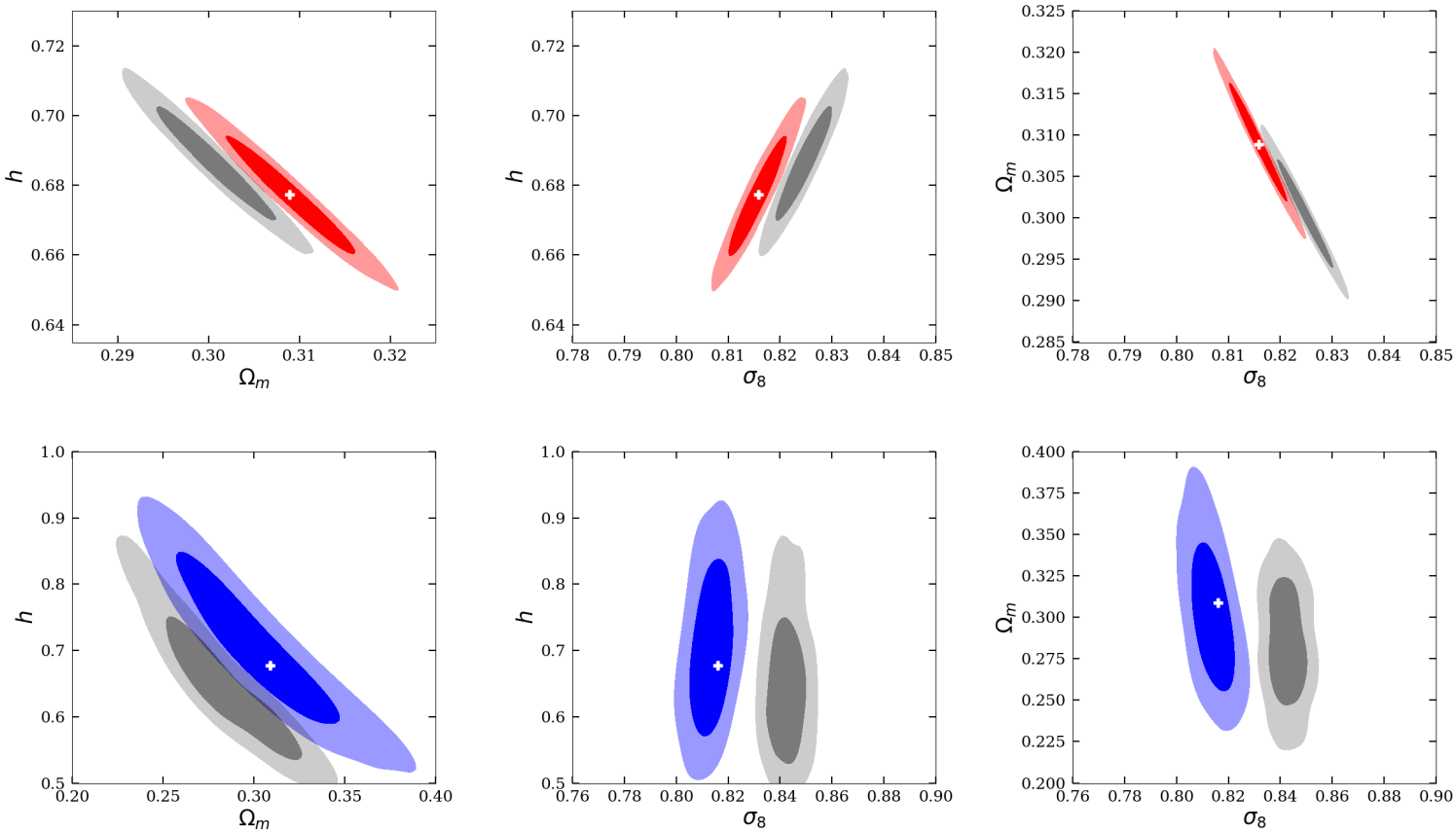

FIGURE 4.6: Constraints on cosmological parameters for the ideal case, i.e. no nuisance parameters. Outer and inner contours respectively correspond to 95% and 68% confidence levels in the joint 2D parameter space. *Top panels:* (*Bottom panels:*) parameter estimation from the *Euclid*-like optical/near-infrared photometric (SKA1-like radio spectroscopic HI-line) galaxy survey with the red (blue) and grey contours accounting for the complete and the incomplete model respectively. The white cross indicates the fiducial cosmology.

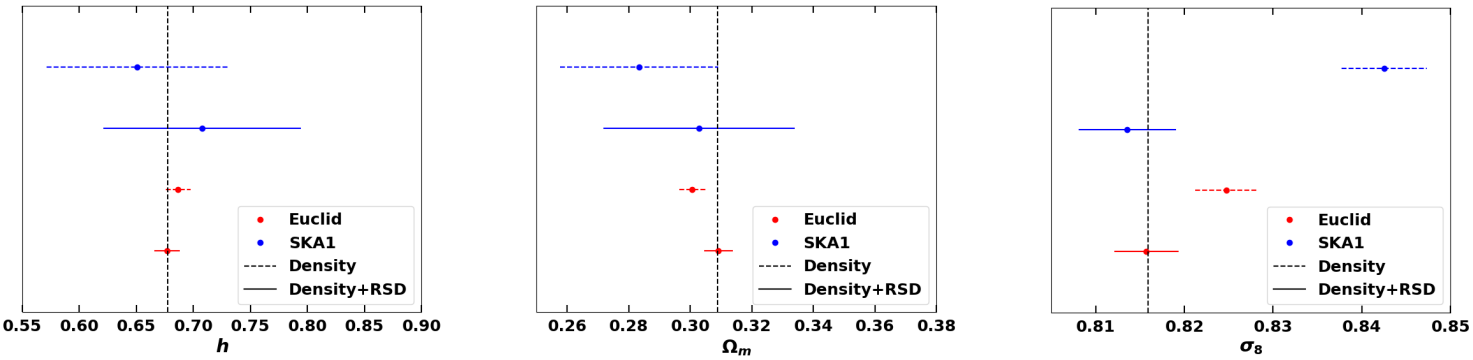

FIGURE 4.7: 1σ marginal errors (horizontal solid (complete model) and dashed (incomplete model) lines) on the estimated mean value (filled bullets) for *Euclid* and SKA1 in the ideal scenario. The vertical dashed black line corresponds to the input value of our fiducial cosmology.

the smaller $f_{\rm sky}$ and the more limited multipole range. In this case, too, it is evident that the estimate from the incomplete, density-only model is biased beyond 1σ for all cosmological parameters, whereas results from the den+RSD model are consistent with the input cosmology (see again Figure 4.7 the blue lines). However, we find that den+RSD model yields slightly weaker constraints compared to the (biased) ones we get when neglecting RSD.

In order to understand this we need to go back to Figure 4.5. In this plot as previously seen in subsection 4.3.4 the SNR is shown, with red and blue curves respectively referring to *Euclid* and SKA1, and dashed(solid) lines for den-only(den+RSD); we also show, as a blue dotted curve, the SKA1 cumulative SNR for den-only in the case where we use the same multipole range as for den+RSD. We notice that for *Euclid* the SNR curve corresponding to den+RSD is always higher than that of the density fluctuations only in the whole multipole range. This makes sense, since we consider additional information by adding the RSD on top of the density fluctuations and, as a result, we increase the signal and obtain higher SNR. Regarding the SKA1 setup, the SNR curves will be significantly lower than in the case of *Euclid* for the reasons explained in subsection 4.3.4. By looking the SNR, we see that the curve for the complete (density+RSD) model is below that of the incomplete one, which neglects RSD. This trend seems to be the exact opposite of the what discussed for *Euclid*. However, we should note that in the case of SKA1 the multipole range where we can trust the Limber approximation is smaller for density+RSD, compared to density perturbations only (see Table 4.1). Given that, we compute again the SNR of the density model but now evaluated at the shorter multipole range that was applied for the correct model. After implementing this (dotted curve), we now observe the same trend as for *Euclid*. This implies that the relatively larger contours for SKA1 den+RSD have to be attributed to the higher ℓ_{min} limit resulting in a slightly shorter multiple range.

4.4.2 Realistic scenario

As mentioned at the beginning of the section, the assumption that our knowledge of the galaxy bias is perfect is an idealistic one. Thus, we now introduce nuisance parameters to account for our inherent ignorance of the bias. Such parameters will then be fitted alongside cosmological parameters. To this purpose, we choose a similar modelling for the two surveys under consideration, i.e. an overall normalisation of the galaxy bias over the whole redshift range, and a parameter accounting for the redshift dependence of the bias. In other words, we let the parameters α_X and β_X of Equation 4.12 and Equation 4.16 to vary freely, with $X = \{\text{Euc}, \text{SKA}\}$. The normalisation and power-law bias nuisance parameters with their corresponding priors for the surveys are shown in Table 4.2.

Figure 4.8 (top panels) shows the results for the optical/near-infrared *Euclid*-like photometric survey, after marginalising over bias nuisance parameters. Interestingly, the constraints on h and Ω_m are very similar to those of the ideal scenario. That is, the biased estimate for density only lies beyond 1σ on Ω_m but not for h with respect to the fiducial values. However, the picture is completely different when it comes to σ_8. It is clear that σ_8 is totally unconstrained by the density-only model (grey contours). The reason for this is that density fluctuations are sensitive to the galaxy bias (the angular power spectrum depends linearly on the bias squared). This means that when we consider an overall normalisation of the bias—common to the whole redshift range—we cannot break the degeneracy present between α_X and σ_8. On the other hand, once we include RSD (red contours), the degeneracy is lifted considerably.

The SKA1 results for this realistic bias scenario are shown in the bottom panels of Figure 4.8. We can appreciate a similar behavior compared to the case of *Euclid*. The incomplete model containing only density fluctuations is statistically significantly biased on Ω_m and, again, the constraint on σ_8 is very degenerate for the reasons explained above. By incorporating RSD in our modeling we manage to alleviate this and get an unbiased estimate of Ω_m. Again, the constraining power of SKA1 is not so good as that of the *Euclid*-like survey, due to the lower SNR.

4.4.3 Conservative scenario

Let us now consider the pessimistic case in which the galaxy bias evolution with redshift is utterly unknown. Thus, we add bias nuisance parameters per redshift bin $b_{\text{g},i}$, with $i = 1, N_z$, and flat priors in the range $[0.1, 1.9]$. We then obtain constraints over the full parameter set consisting of 13 parameters—namely three cosmological parameters plus N_z bias nuisance parameters—and present the joint 2D marginal error contours on the cosmological parameters by marginalising over all the bias parameters.

As before, in Figure 4.10 (top panels) we present the cosmological constraints from *Euclid*. Again, we can clearly see that the results on h and Ω_m are quite similar

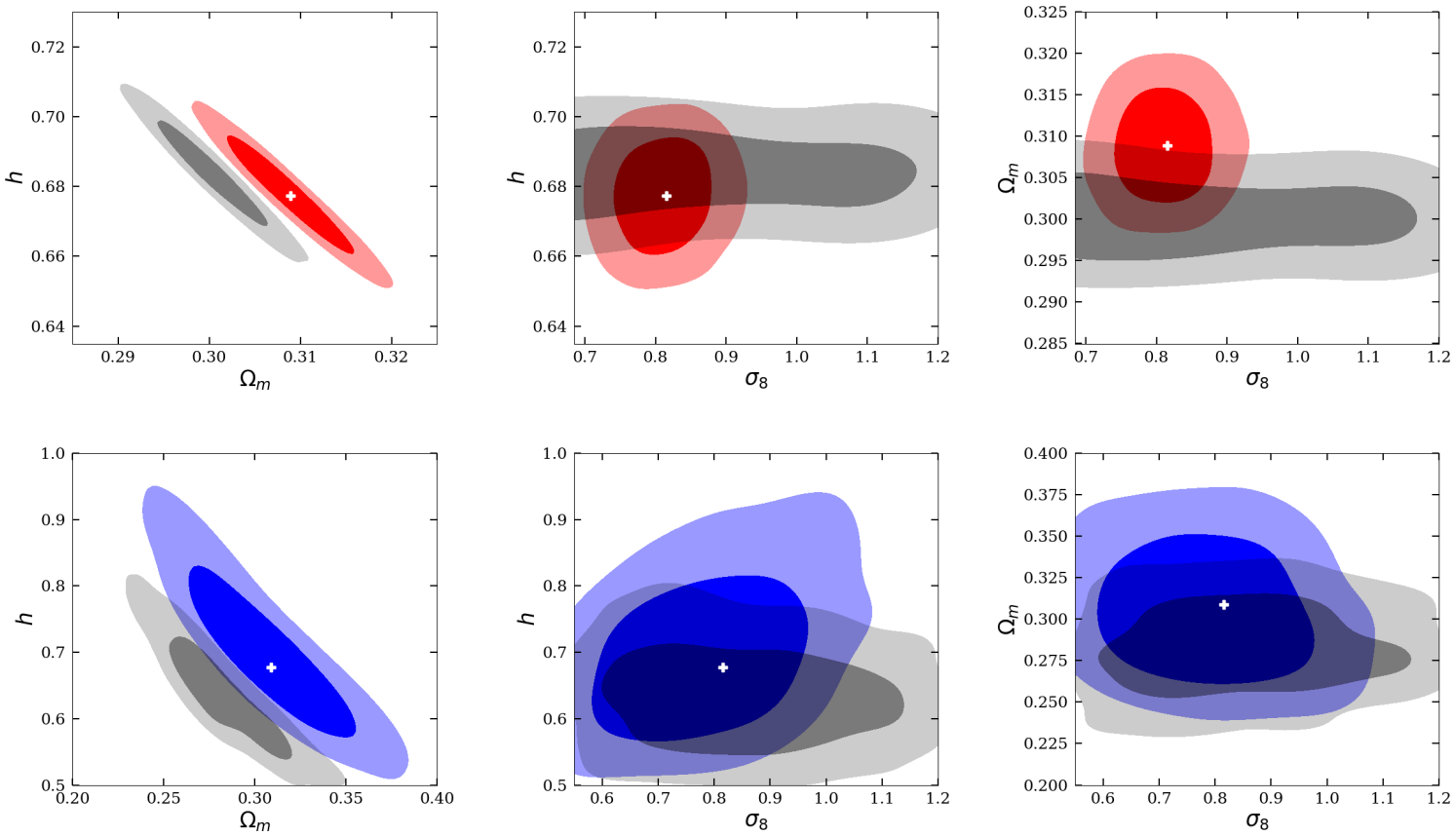

FIGURE 4.8: Same as Figure 4.6 but for the realistic scenario, i.e. two nuisance parameters modelling the overall amplitude and the redshift evolution of the bias.

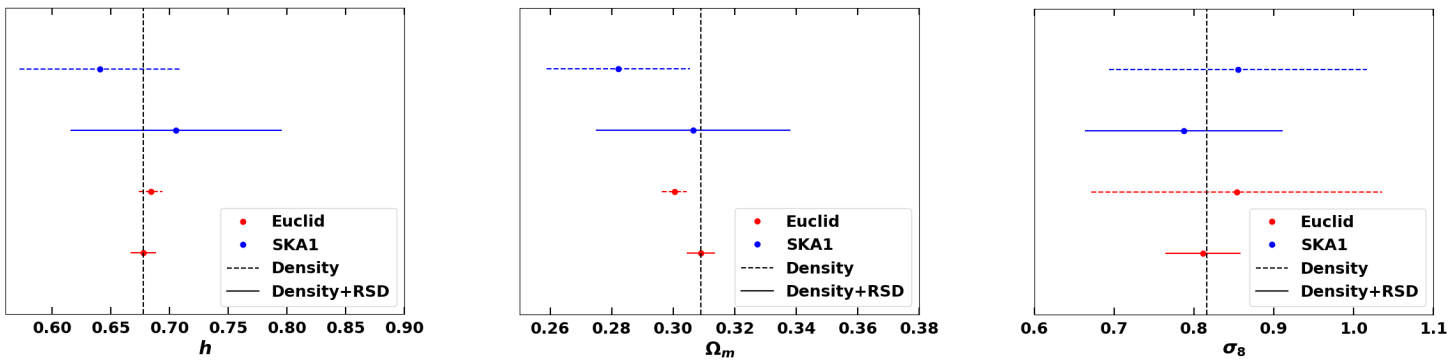

FIGURE 4.9: Same as Figure 4.7 but for the realistic scenario

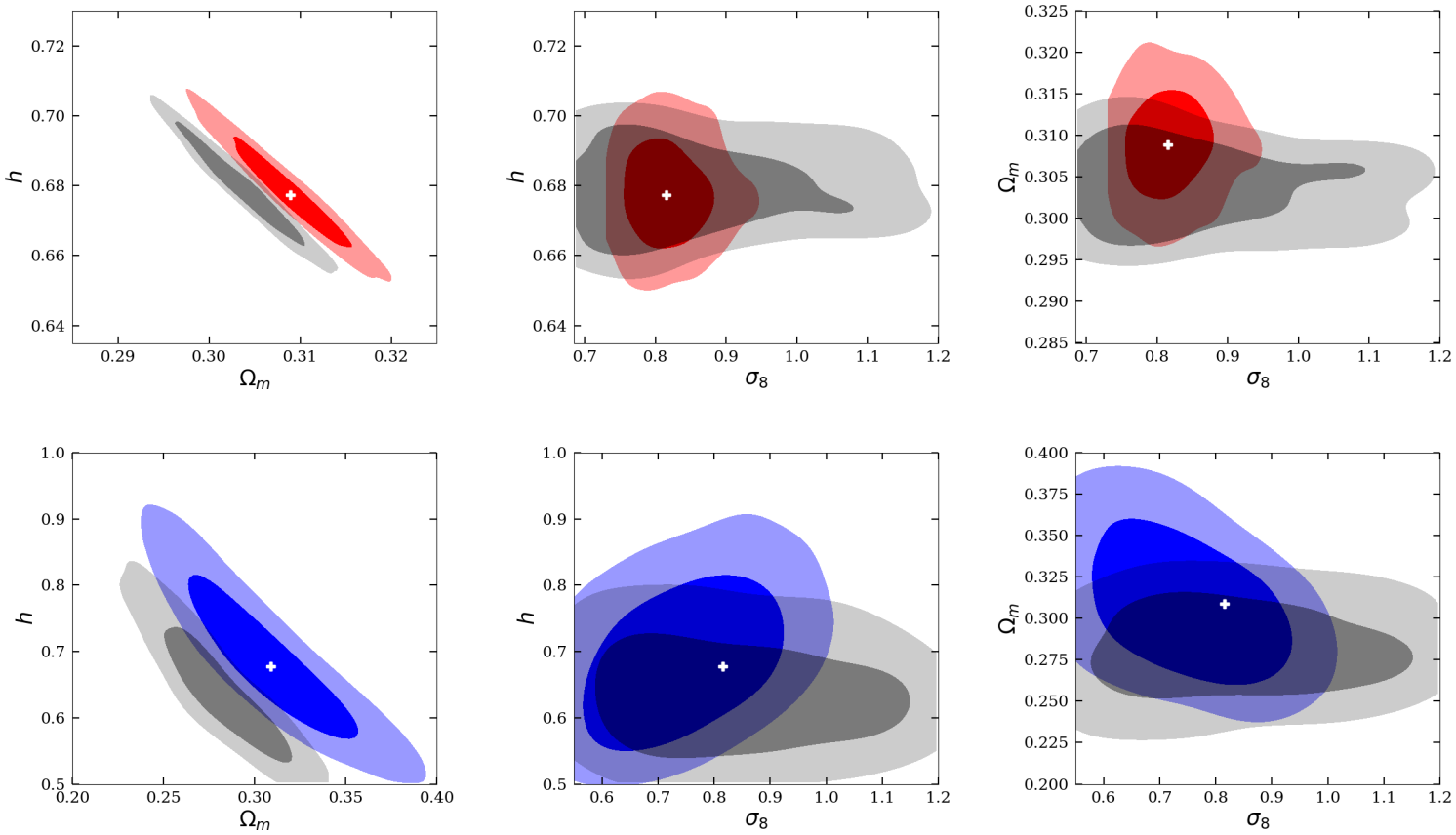

FIGURE 4.10: Same as Figure 4.6 but for the conservative scenario, i.e. one nuisance bias parameter per redshift bin.

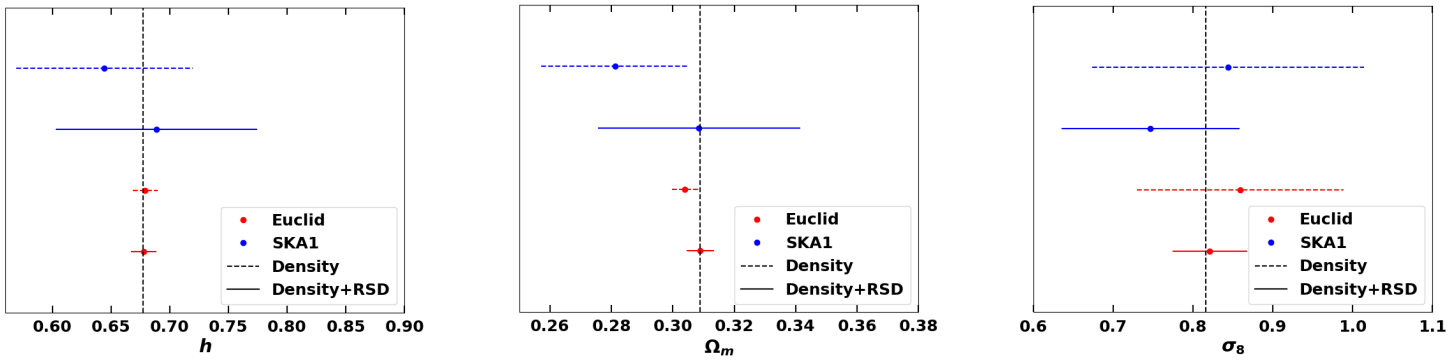

FIGURE 4.11: Same as Figure 4.7 but for the conservative scenario

TABLE 4.3: Means and corresponding 68% marginal error intervals on cosmological parameters for the optical/near-infrared *Euclid*-like photo-z galaxy survey.

	Euclid					
	Ideal scenario		Realistic scenario		Conservative scenario	
	den	den+RSD	den	den+RSD	den	den+RSD
$\Omega_{\rm m}$	0.3006 ± 0.0042	0.3091 ± 0.0046	0.3003 ± 0.0040	0.3089 ± 0.0045	0.3038 ± 0.0042	0.3089 ± 0.0045
h	0.6865 ± 0.0107	0.6770 ± 0.0111	0.6837 ± 0.0101	0.6775 ± 0.0109	0.6791 ± 0.0105	0.6778 ± 0.0108
σ_8	0.8247 ± 0.0034	0.8157 ± 0.0036	0.8534 ± 0.1823	0.8111 ± 0.0474	0.859 ± 0.1298	0.8211 ± 0.0469

TABLE 4.4: Means and corresponding 68% marginal error intervals on cosmological parameters for the radio SKA1-like spectro-z galaxy survey.

	SKA1					
	Ideal scenario		Realistic scenario		Conservative scenario	
	den	den+RSD	den	den+RSD	den	den+RSD
$\Omega_{\rm m}$	0.2833 ± 0.0256	0.3028 ± 0.0311	0.2821 ± 0.0232	0.3063 ± 0.0316	0.2811 ± 0.0239	0.3084 ± 0.0329
h	0.6504 ± 0.0793	0.7077 ± 0.0866	0.6404 ± 0.0684	0.7054 ± 0.0897	0.6443 ± 0.0752	0.6887 ± 0.0857
σ_8	0.8425 ± 0.0048	0.8135 ± 0.0055	0.8552 ± 0.1613	0.7872 ± 0.1238	0.8438 ± 0.1703	0.7467 ± 0.1118

to those from the ideal and the realistic scenario with the matter density parameter $\Omega_{\rm m}$ being more than 1σ away from the input values for the incomplete model. Likewise, the results on the normalisation σ_8 are equivalent to that of the pessimistic case. That is, the persistence of the degeneracy on σ_8. We, again, alleviate this with the correct den+RSD model—since RSD are not sensitive to the galaxy bias—which yields results in agreement with the fiducial cosmology.

The case for SKA1 is shown in Figure 4.10 (bottom panels). It is obvious, as well, that the picture does not change with respect to the pessimistic scenario. In a similar fashion, the incomplete model yields degenerate results on σ_8, while the correct model gives more tighter constraints. In addition to that, the estimate of the density model on Ω_m remains biased more than 1σ away.

Chapter 5

A case study for magnification bias and radio continuum surveys

5.1 Galaxy clustering in harmonic space

Here, we describe how to construct the galaxy clustering (tomographic) angular power spectrum, $C_\ell^{\rm g}(z_i, z_j)$, including contributions from density fluctuations, RSD, and magnification bias. Again, to ensure the robustness of our cosmological results, we use only linear scales (see Jalilvand et al., 2019, for a study on nonlinearities in angular spectra) in a region where the Limber approximation holds true (Limber, 1953; Kaiser, 1992). In the following analysis, we implement this framework in a modified version of the `CosmoSIS` package. The treatment in our analysis follows closely that of chapter 4, to which we refer the reader for any clarification.

5.1.1 The observed galaxy number count angular power spectrum

The total linear angular power spectrum including for the RSD and magnification bias correction on the galaxy density field is given by Equation 3.149 and Equation 3.150.

The inclusion of the lensing magnification in cross and auto-correlations of galaxy clustering and cosmic shear has been studied with Fisher analysis (Duncan et al., 2013; Villa, Di Dio, and Lepori, 2018; Thiele, Duncan, and Alonso, 2019; Vanessa Böhm and Castorina, 2019), where it has already been suggested that the ignorance of the magnification bias may induce a bias in the cosmological parameter estimation. Here, as we will see, we test this hypothesis by performing a full likelihood mock data analysis.

If we are interested in constraining standard cosmological parameters, the lowest multipoles, corresponding to ultra-large scales, are of little interest (Camera, Maartens, and Santos, 2015b; Lorenz, Alonso, and Ferreira, 2018). As we have already mentioned in chapter 4, this allows us to resort to the Limber approximation, thus getting rid of the integration of the spherical Bessel functions, which is computationally expensive and highly oscillating, thus inducing numerical instabilities. It is worth noting, however, that there are nowadays publicly available routines implementing fast Fourier transforms, such as `AngPow` (Campagne, J.-E., Neveu, J., and

Plaszczynski, S., 2017), which can be applied for the computation of tomographic power spectra beyond the Limber approximation in the case one was interested to the largest scales or wanted to reduce the multipole cuts for cross-bin correlations, (see also Chisari et al., 2019).

The Limber approximation works well for $\ell \gg 1$, and the spherical Bessel functions are replaced by a Dirac Delta, (see Equation 4.4). By implementing this into Equation 3.149, we get:

$$C^{\mathrm{g}}_{\ell\gg1}(z_i, z_j) = \int \mathrm{d}\chi \, \frac{W^i_{\mathrm{g}}(\chi) W^j_{\mathrm{g}}(\chi)}{\chi^2} P_{\mathrm{lin}}\left(k = \frac{\ell + 1/2}{\chi}\right), \tag{5.1}$$

with

$$W^i_{\mathrm{g}}(\chi) = W^i_{\mathrm{g,den}}(\chi) + W^i_{\mathrm{g,RSD}}(\chi) + W^i_{\mathrm{g,mag}}(\chi). \tag{5.2}$$

Here, we have split the contributions into three separate window functions: the standard one, for density fluctuations,

$$W^i_{\mathrm{g,den}}(\chi) = n^i(\chi) b(\chi) D(\chi); \tag{5.3}$$

the one for RSD, found in chapter 4 to be

$$\begin{aligned} W^i_{\mathrm{g,RSD}}(\chi) = {} & \frac{2\ell^2 + 2\ell - 1}{(2\ell - 1)(2\ell + 3)} \left[n^i f D\right](\chi) \\ & - \frac{(\ell - 1)\ell}{(2\ell - 1)\sqrt{(2\ell - 3)(2\ell + 1)}} \left[n^i f D\right]\left(\frac{2\ell - 3}{2\ell + 1}\chi\right) \\ & - \frac{(\ell + 1)(\ell + 2)}{(2\ell + 3)\sqrt{(2\ell + 1)(2\ell + 5)}} \left[n^i f D\right]\left(\frac{2\ell + 5}{2\ell + 1}\chi\right); \end{aligned} \tag{5.4}$$

and that of magnification bias,

$$W^i_{\mathrm{g,mag}}(\chi) = \frac{3\Omega_{\mathrm{m}} H_0^2}{c^2} \left[1 + z(\chi)\right] \chi \tilde{n}^i(\chi) \left[\mathcal{Q}(\chi) - 1\right] D(\chi). \tag{5.5}$$

5.2 Survey specifications

As mentioned in chapter 1, we decide to focus on radio continuum surveys, because they are an ideal test case for magnification, thanks to their unrivalled depth. The NRAO VLA Sky Survey (NVSS, Condon et al., 1998) has been the primary source of data for previous cosmological analyses based on radio continuum galaxies (e.g. Boughn and Crittenden, 2001; Overzier, R. A. et al., 2003; Boughn and Crittenden, 2004; Nolta et al., 2004; Smith, Zahn, and Doré, 2007; Raccanelli et al., 2008; Ho et al., 2008; Afshordi and Tolley, 2008; Xia et al., 2011; Rubart, M. and Schwarz, D. J., 2013; Giannantonio et al., 2014; Nusser and Tiwari, 2015; Planck Collaboration et al., 2016). The potentiality of oncoming radio continuum surveys for cosmology has

TABLE 5.1: Estimated number densities, galaxy bias, and magnification bias for EMU sources grouped in 2 redshift bins.

Bin	$z_{\rm min}$	$z_{\rm max}$	# of gal. ($\times 10^6$)	bias	mag. bias
1	0.0	1.0	10.68	0.833	1.050
2	1.0	6.0	11.58	2.270	1.298

also been extensively studied in recent years (Raccanelli et al., 2012; Camera et al., 2012; Raccanelli et al., 2015; Bertacca et al., 2011; Jarvis et al., 2015; Camera, Santos, and Maartens, 2015b; Ferramacho et al., 2014; Karagiannis et al., 2018; Scelfo et al., 2018; Ballardini et al., 2018; Bernal et al., 2019).

For the present analysis, we adopt the specifications of the Evolutionary Map of the Universe (EMU). EMU is a deep radio-continuum full-sky survey (Norris et al., 2011) at ASKAP (Johnston et al., 2007; Johnston et al., 2008), whose goal is to detect extragalactic objects in the continuum across the entire southern sky, up to $\delta = +30^\circ$. Even though ASKAP was designed as a precursor to the SKA, the large field of view, accurate pointing and angular resolution, and sensitive phased-array feeds will render it the foremost radio survey instrument in the frequency range around 1 GHz during the next decade. The EMU survey, covering such a wide area, and going much deeper than previous large-area radio continuum surveys, will be able to map the large-scale distribution of matter over a larger volume than has previously been possible, and so will be ideal to investigate extensions of the ΛCDM model (Raccanelli et al., 2012; Camera et al., 2012; Bernal et al., 2019).

EMU will cover an area of $30,000\,\mathrm{deg}^2$ with a sensitivity of $10\,\mu$Jy per beam rms, and a resolution of ~ 10 arcsec, over the frequency range of 800-1400 MHz. To estimate the redshift distribution $n(z)$ of active galactic nuclei and star-forming galaxies, a 10-sigma detection limit of 100 μJy is assumed, and galaxies are sampled from the mock catalogues generated by the SKA Simulated Skies (S-cubed)[1] simulations down to that limit. The distribution of redshifts and magnitudes from these mocks are used to estimate the overall $n(z)$, and also the magnification bias, $\mathcal{Q}(z)$.

Under the assumption that additional external data will be available for the redshifts of part of EMU galaxies (e.g. cross-identifications, McAlpine et al. 2012; Bayesian hierarchical models, Harrison, Lochner, and Brown 2017; or so-called clustering redshifts, Ménard et al. 2013), we here scrutinise two binning scenarios. The former, in which we assume we can differentiate only between low- and high-redshift galaxies (divide set at $z = 1$), is more conservative; the latter sees five redshift bins, four of which of width $\Delta z = 1$ below $z = 2$, and the fifth collecting all the galaxies above. The expected numbers for these settings are given in Table 5.1 and Table 5.2.

We discussed above that radio continuum surveys lack information in redshift and therefore the most realistic representation of the galaxy sampling in redshift space is that of residing in Gaussian bins. However, we decide to consider the case of sharp top-hat bins which are not correlated in redshift. We apply this mostly for

[1] http://s-cubed.physics.ox.ac.uk/

TABLE 5.2: Same as Table 5.1, but for EMU sources grouped in 5 redshift bins.

Bin	$z_{\rm min}$	$z_{\rm max}$	# of gal. ($\times 10^6$)	bias	mag. bias
1	0.0	0.5	5.55	1.000	0.953
2	0.5	1.0	5.13	1.124	1.273
3	1.0	1.5	4.43	1.920	1.569
4	1.5	2.0	2.70	3.250	1.176
5	2.0	6.0	4.05	4.046	0.964

the sake of fully exploring the potential of magnification. The magnification bias is expected to induce a correlation even between uncorrelated redshift bins, in a sense that the lower-z bins are the 'lenses' and the high-z bins the 'sources'. Thus, it is worth investigating magnification in this case, too, implemented at least at the ΛCDM scenario.

Given that $\mathrm{d}N$ is the number of galaxies inside a bin of width $\mathrm{d}z$, the redshift distribution of sources is $N(z) = \mathrm{d}N/\mathrm{d}z$.[2] Then, the $N(z)$ points are fitted with a 7th order polynomial, $n(z)$, by which we denote the total number counts of sources with redshift. The distribution of sources residing in the ith bin thus is $n^i(z)$, and the angular number counts of galaxies reads

$$\bar{n}^i = \int \mathrm{d}z\, n^i(z), \tag{5.6}$$

Therefore, the total number counts of galaxies is simply $\bar{n} = \sum_i \bar{n}^i$.[3] The final, fitted redshift distributions, convolved with the bins, are shown in Figure 5.1.

Top-hat bins (left panels of Figure 5.1) have been modelled by Equation 4.17 and we quote the formula again here for clarity,

$$n^i(z) = \frac{1}{2}\left\{1 - \tanh\left[\frac{|z - \bar{z}_i| - \sigma}{r\sigma}\right]\right\}, \tag{5.7}$$

where $\bar{z}_i$ is the centre of the ith bin, σ the half top-hat width, and r the smoothing edge, which we fix to 0.03. The smearing ensures the numerical stability in the integration over the bin. Instead, to model Gaussian bins, we consider the ranges $z_{\rm min}$ and $z_{\rm max}$ of Table 5.1 and Table 5.2, and definde

$$n^i(z) = \frac{1}{2} n(z) \left[\mathrm{erfc}\left(\frac{z^i_{\rm min} - z}{\sqrt{2}\sigma(z^i_{\rm min})}\right) - \mathrm{erfc}\left(\frac{z^i_{\rm max} - z}{\sqrt{2}\sigma(z^i_{\rm max})}\right)\right]. \tag{5.8}$$

Note that, in this latter case, we introduce a redshift dependence of the scatter of the distribution, $\sigma(z)$. Specifically, we adopt a quite large uncertainty, $\sigma(z) = 0.1(1+z)$. The Gaussian bins are shown in the right panels of Figure 5.1.

[2] The number of sources has also been calculated in very narrow 32 redshift bins, which are not shown here for clarity.

[3] Note again that $n^i(z)$ is normalised to unity in the equations of the previous section, like Equation 5.3, Equation 5.4, and Equation 5.5, meaning that it as to be read as $n^i(z)/\bar{n}^i$.

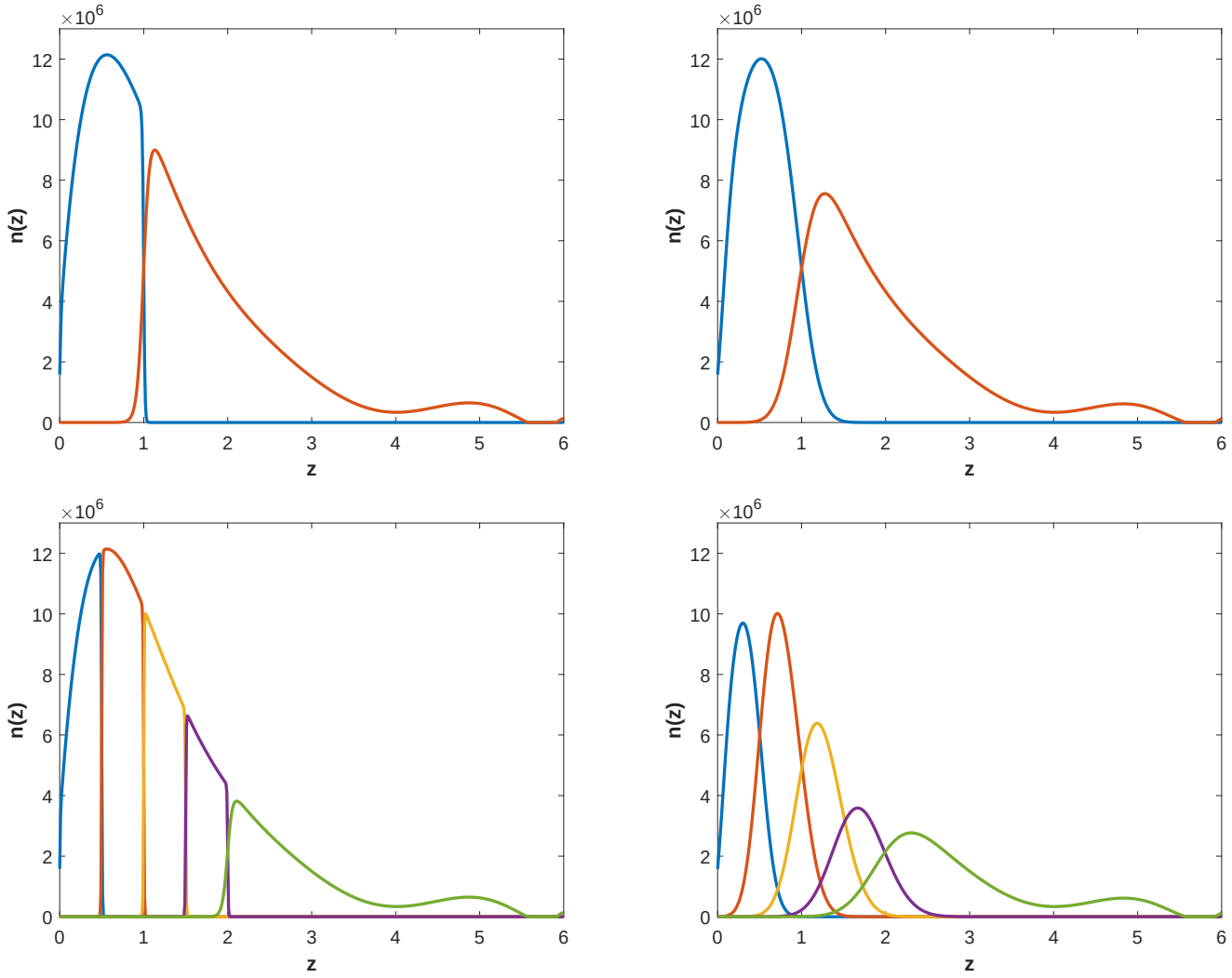

FIGURE 5.1: The EMU galaxy redshift distribution for top-hat (left panels) and Gaussian (right panels) binning. The top and bottom panels present the 2 and the 5 bins, respectively.

5.3 Cosmological models

In this work, we will investigate the vanilla ΛCDM model and two of its most popular extensions: the case of a dynamical DE component and a phenomenological modified gravity model. All the model parameters are summarised in Table 6.3. For ΛCDM, we present the constraints for the parameter set $\{\Omega_m, h, \sigma_8\}$ alone, whilst the other parameters are fixed to their fiducial values.

5.3.1 Dark energy

The first extension to the ΛCDM model is a dynamical DE model, where the DE equation of state is not constant throughout the cosmic history, but it is rather allowed to evolve with time. According to (Chevallier and Polarski, 2001; Linder, 2003), by Taylor expanding an evolving dark energy equation of state and keeping only the first order term we have

$$w_{\rm DE}(z) = w_0 + w_a \frac{z}{1+z}. \tag{5.9}$$

Therefore, we add to the ΛCDM model the parameter set both w_0 and w_a.

5.3.2 Modified gravity

An alternative explanation for the late-time accelerated cosmic expansion is offered by modified gravity theories (MG, hereafter). This approach sees the effects we ascribe to dark energy (and even dark matter) are in fact due to our wrong interpretation of the data in a regime where general relativity no longer holds (Clifton et al., 2012). For the purpose of our work, we assume a popular phenomenological parameterisation accounting for the peculiar effect of modified gravity on structure formation (Amendola, Kunz, and Sapone, 2008; Zhao et al., 2010; Dossett et al., 2015). Specifically, we can assume a modified Poisson equation

$$\nabla^2\Phi = 4\pi G Q a^2 \bar{\rho}\delta, \tag{5.10}$$

where Q is in principle a function of space and time, and acts as an effective gravitational constant. Moreover, the two metric potentials can be different, and the function R describes the ratio of the two, viz.

$$R = \frac{\Psi}{\Phi}. \tag{5.11}$$

Thus, we add as free parameters the two present-values of these quantities, Q_0 and R_0. In fact, given that they are degenerate, it is very convenient to define the derived parameter $\Sigma_0 = Q_0(1+R_0)/2$, and therefore use the parameter set $\{Q_0, \Sigma_0\}$ instead, along with the parameters of the ΛCDM model.

TABLE 5.3: Prior ranges and fiducial values on the nuisance and cosmological parameters (ΛCDM best-fit of Ade et al. 2016). Some parameters are purposely allowed to have wider or narrower prior ranges due to the difference in the constraining power of the results depending on the number of the bins considered. (When two sets of values are present, values in parentheses refer to the 5 bin case, as opposite to those outside that are relative to the 2 bin case.)

Parameter description	Parameter symbol	Fiducial value	Prior type	Prior range
Present-day fractional matter density	$\Omega_{\rm m}$	0.3089	Flat	$[0.1, 0.6]$
Dimensionless Hubble parameter	h	0.6774	Flat for 2(5) bins	$[0.3, 1.0]([0.5, 1.0])$
Amplitude of clustering‡	σ_8	0.8159	Flat for 2(5) bins	$[0.4, 1.4]([0.5, 1.2])$
Present-day fractional baryon density	$\Omega_{\rm b}$	0.0486	–	–
Slope of the primordial curvature power spectrum	$n_{\rm s}$	0.9667	–	–
Amplitude of the primordial curvature power spectrum‡	$\ln(10^{10} A_{\rm s})$	3.064	–	–
Optical depth to reionisation	$\tau_{\rm re}$	0.066	–	–
Bias amplitude parameter for the whole redshift range¶	$\alpha_{\rm EMU}$	1.0	Flat	$[0.4, 1.6]$
Free bias amplitude in each redshift bin§	b_i $i = 1 \dots 2(5)$	See Table 5.1(Table 5.2)	Flat for 2(5) bins	$[0.1, 3.5]([0.1, 9.0])$
Present-day dark energy equation of state	w_0	-1.0	Flat	$[-3.0, 2.0]$
Dark energy evolution parameter	w_a	0.0	Flat	$[-6.0, 4.0]$
Modified gravity parameter	Q_0	1.0	Flat	$[0.0, 8.0]$
Modified gravity parameter	R_0	1.0	Flat	$[-1.0, 8.0]$

‡ Instead of setting the prior on the parameter $A_{\rm s}$ accounting for the matter perturbations amplitude, we opt for σ_8, following the convention in LSS.
¶ The prior range reported on the parameter is applied in the 'realistic' scenario alone (notation mirrors chapter 4).
§ The prior range reported on the parameter is applied in the 'conservative' scenario alone.

5.4 Methodology

To forecast constraints on cosmological parameters, we follow a likelihood-based approach. The first step is to estimate the covariance matrix, $\mathbf{\Gamma}_{\ell\ell'}$, for our observable, namely the galaxy clustering power spectrum in harmonic space given in Equation 5.1. We use the analytical form of the Gaussian covariance matrix, as already implemented in `CosmoSIS`, and described by Equation 4.20. We employ $N_\ell = 20$ multipole bins (see subsection 5.4.1 for the range adopted), and for all redshift and multipole bin values we construct the full data vector $\boldsymbol{d}_\ell$ (see Equation 4.22), as well as the theory vector $\boldsymbol{t}_\ell(\boldsymbol{\theta})$, which is a function of the parameter set, $\boldsymbol{\theta}$. With all the above one can construct the Gaussian log-likelihood Equation 4.23 which is to be minimised for some specific values of the parameters.

5.4.1 Multipole cuts

Since Limber approximation is valid only at $\ell \gg 1$, we have derived the $\ell_{\rm min}$ below which we can trust no longer the angular power spectra values computed via Equation 5.1. To do so, we compare results computed by our modified `CosmoSIS` code with the full solution of the `CLASS` Boltzmann solver and keep only the multipoles where the relative error between the two codes is below 5% (see again chapter 4). We make this choice since this percentage offset is within the standard deviation of the signal measurement.

Additionally, we apply an upper cut at $\ell_{\rm max} = \chi(\bar{z}_i)k_{\rm max}$, since we ignore the nonlinear scales in our analysis. Here, $\bar{z}_i$ is the centre of the ith redshift bin, whilst the maximum wavenumber is chosen to be $k_{\rm max} = \pi/(2R_{\rm min})$, where $R_{\rm min}$ is the radius of a sphere inside which the over-density fluctuations at $z = 0$ have a value given by Equation 4.19. The matter density variance is chosen again to be $\sigma^2(R_{\rm min}) = 1$, yielding $k_{\rm max} = 0.25\ h\,{\rm Mpc}^{-1}$. We should note that we keep the same $k_{\rm max}$ value for all the analyses in this thesis for completeness.

The $\ell_{\rm min}$ and $\ell_{\rm max}$ cuts are applied to each bin pair according to the all the configurations of the EMU distribution (see again Figure 5.1), and are shown in Table 5.4, where RSD do not appear explicitly because we found that their inclusion does not affect the value of $\ell_{\rm min}$. (On the other hand, $\ell_{\rm max}$ does not depend on the terms included in Equation 5.1, as it is only a function of $k_{\rm max}$ and the central redshift of the bin.)

5.5 Results and discussion

Let us summarise again here the cosmological parameter sets for the three different cosmological models, $\boldsymbol{\theta}_{\Lambda{\rm CDM}} = \{\Omega_{\rm m}, h, \sigma_8\}$, $\boldsymbol{\theta}_{\rm DE} = \boldsymbol{\theta}_{\Lambda{\rm CDM}} \cup \{w_0, w_a\}$ and $\boldsymbol{\theta}_{\rm MG} = \boldsymbol{\theta}_{\Lambda{\rm CDM}} \cup \{Q_0, \Sigma_0\}$. In our forecasting analysis, we use the Bayesian sampler `Multinest` (Feroz, Hobson, and Bridges, 2009).

TABLE 5.4: The $\ell_{\rm min}$ and $\ell_{\rm max}$ values for all the EMU bin configurations. The former is specified as the point where the relative error between `CosmoSIS` and `CLASS` angular power spectra measurements is below 5%, while the latter in the limit where $\ell_{\rm max} = k_{\rm max}\chi(\bar{z}_i)$ with $\bar{z}_i$ the centre of the ith bin.

2 redshift bins					5 redshift bins				
$\ell_{\rm min}$				$\ell_{\rm max}$	$\ell_{\rm min}$				$\ell_{\rm max}$
Top-hat		Gaussian			Top-hat		Gaussian		
w/o mag	w/ mag	w/o mag	w/ mag		w/o mag	w/ mag	w/o mag	w/ mag	
3	2	2	2	480	2	2	2	2	257
10	12	10	10	1718	6	6	8	8	673
–	–	–	–	–	17	18	11	11	982
–	–	–	–	–	24	25	10	10	1215
–	–	–	–	–	24	25	9	9	1813

We forecast cosmological parameter constraints using both the incomplete $C^{\rm g,den}_{\ell\gg1}$ and the correct $C^{\rm g,den+mag}_{\ell\gg1}$ spectra for the different binning configurations of EMU, fitting the mock data using a likelihood of the form described in section 5.4. Note that for the moment we neglect RSD in the modelling of the synthetic data. The reason for this will be come clear afterwards, and we discuss the issue in subsection 5.5.6. The mock-data vector $\boldsymbol{d}_\ell$ is thus constructed assuming the density perturbations and the magnification bias described in section 5.1, according to the fiducial cosmology given in Table 5.3.

Additionally, we need to add a number of extra nuisance parameters to our analysis, that will be marginalised over, in addition to the cosmological parameters of interest. These nuisance parameters model our ignorance on some underlying quantity such as the galaxy bias, and depend also upon the binning strategy adopted. We introduce three cases:

1. An idealistic scenario, where the galaxy bias is perfectly known, keeping its fiducial values as in Table 5.1 and Table 5.2;

2. A realistic scenario, with an single bias amplitude parameter spanning the whole redshift range, which is taken as a free parameter;

3. A realistic, yet conservative scenario, allowing for a free galaxy bias parameter per each redshift bin.

Let us finally remark that the magnification bias for each redshift bin keeps its fiducial value as in Table 5.1 and Table 5.2, and it remains fixed throughout the analysis and for all the scenarios. Moreover, we choose to take the means of the posterior distribution instead of the best-fit values to allow for safer conclusions in the case of highly non-Gaussian posterior distributions (see section 4.4). The results are presented and discussed thoroughly in the next subsections where we uniformly opt to

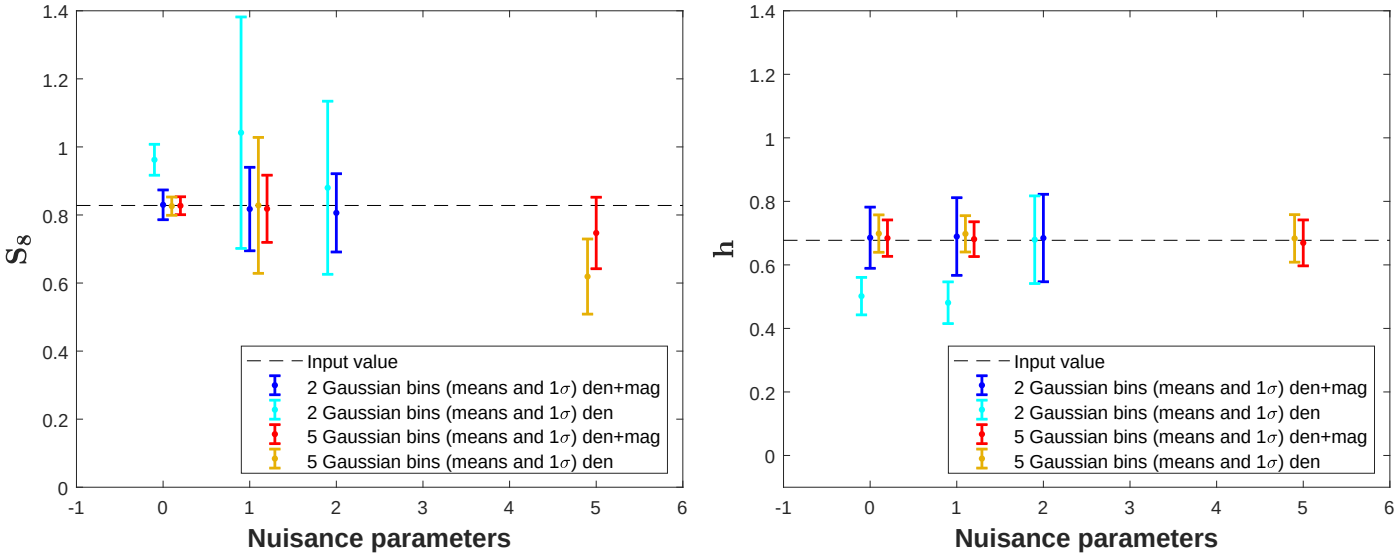

FIGURE 5.2: EMU mean and 68% confidence intervals on the derived S_8 (left) and h (right) cosmological parameter for Gaussian binning as a function of the number of nuisance parameters for the ΛCDM model. Note the different colors accounting for the number of bins and the combination of density and magnification in the theory vector.

show the constraints on the derived parameter

$$S_8 = \sigma_8 \sqrt{\frac{\Omega_m}{0.3}}, \tag{5.12}$$

which is better constrained than σ_8, and is not correlated with Ω_m. In all plots the means of the posterior along with the 68% marginal errors for each parameter are shown.

5.5.1 Constraints on ΛCDM

In Figure 5.2 we present the 68% marginal confidence intervals and the means on $\{S_8, h\}$ for 2 and 5 Gaussian bins—a binning scenario closer to reality. As a general remark, we shall see that whether we consider the realistic or the conservative scenarios, the constraining power that we get from the correct model (i.e. den+mag) is comparable. This is true for both binning configurations, and as we will see in the following sections, this feature remains the same in the cases of extensions of the ΛCDM model.

Results for top-hat bins are very similar to those obtained with more realistic Gaussian bins, so we report the corresponding figure and tables in section B.1, limiting ourselves to point out that the main difference between Gaussian and top-hat binning is that the latter sees mildly biased estimates for h even in the 5-bin, 1-nuisance parameter case. This is mainly due to the slightly tighter constraints obtained with top-hat bins in this configuration, meaning that the observable is more

sensitive to the Hubble constant thanks to the better redshift resolution. Besides this, on a general ground, we see no further, major difference between top-hat and Gaussian bins. This has to be attributed to the fact that the bins considered for the EMU distribution are quite wide regardless of the top-hat or Gaussian bin choice.

Nonetheless, the offsets in the parameter estimates obtained with Gaussian bins are always a bit more pronounced compared to top-hat bins. That is, Gaussian bins, given the poor redshift estimate, are wider than the sharp top-hats, and so have more sources with a significantly different dynamical time, along the line of sight in the same redshift bin. As a result, the wider the bin is, the larger the magnification bias is, inducing a larger offset in the results when excluded.

5.5.2 Two Gaussian bins

In the case where the galaxy bias is perfectly known—the idealistic scenario, marked by '0 nuisance parameters' on abscissas of Figure 5.2—it is evident that when we fit the mock data with the complete model (blue error bar), the input reference values are well within the 68% error interval calculated on both parameter, S_8 and h. On the other hand, when we assume the incomplete model (cyan error bar), namely ignoring the magnification contribution in the theory vector, the estimates of $\{S_8, h\}$ are clearly biased with respect to the input reference.

Then, in the realistic scenario we introduce a free galaxy bias parameter $\alpha_{\rm EMU}$ for the whole redshift range ('1 nuisance parameters' mark on the x-axis). The results presented on the cosmological set $\{S_8, h\}$ are then obtained after marginalising over this nuisance parameter. Interestingly, now the results on S_8 are different. That is, even with the incorrect model S_8 becomes totally unconstrained (cyan error bar). The reason for this is that the galaxy density field is highly sensitive to the galaxy bias. As a result, there is a degeneracy between the galaxy bias and the amplitude of matter fluctuations, S_8. Nonetheless, when we consider magnification, too (blue error bar), we lift this degeneracy considerably, and the error bar shrinks.

Now, we examine the conservative scenario, where we allow for a nuisance bias parameter for each redshift bin, b_i, in the range $[0.1, 3.5]$ to be marginalised over ('2 nuisance parameters' tick). Constraints on S_8 is quite similar to those of the realistic scenario, with the incomplete model yielding a degenerate S_8 (cyan error bar) estimate, in turn mitigated by the incorporation of the magnification bias (blue error bar) for the same reasons mentioned above. On the contrary, we see no deviance in the h for the wrong model (cyan error bar). This is probably due to the fact that we use a larger number of nuisance parameters, leading to an overall broadening of the confidence intervals.

The findings for the case of 2 Gaussian bins are quantitatively summarised in Table 5.5.

TABLE 5.5: Means and corresponding 68% marginal error intervals on cosmological parameters for the EMU radio continuum galaxy survey applying 2 Gaussian bins with the ΛCDM model.

2 Gaussian bins (ΛCDM)						
	Ideal scenario		Realistic scenario		Conservative scenario	
	den	den+mag	den	den+mag	den	den+mag
S_8	0.962 ± 0.045	0.830 ± 0.044	1.04 ± 0.34	0.82 ± 0.12	0.88 ± 0.25	0.81 ± 0.12
h	0.502 ± 0.059	0.686 ± 0.096	0.481 ± 0.066	0.69 ± 0.12	0.68 ± 0.14	0.68 ± 0.14

5.5.3 Five Gaussian bins

Let us now turn to the results obtained with 5 bins. Starting from the idealistic case, where the galaxy bias is known exactly, it is clear that there is no bias on any cosmological parameter of interest when using the wrong model (yellow error bar). After marginalising over the normalisation bias parameter for the whole redshift range (realistic scenario), a degeneracy between this $\alpha_{\rm EMU}$ and S_8 appears (yellow error bar), in a similar fashion to the 2 bin analysis with density only. In agreement with the previous results, the correction of the magnification effect yields more stringent constraints (red error bar). Also, h estimated with the incomplete model (yellow error bar) stays consistent with the fiducial cosmology for both the realistic and the conservative case.

It is worth noting that the picture changes in the conservative case (now allowing this prior range $[0.1, 9.0]$) concerning the estimate on S_8 with the wrong model (yellow error bar). In detail, this estimate is biased for more than 68% below the reference value. However, the inclusion of magnification corrects for this bias completely (red error bar). The last result on S_8 may seem a bit unexpected, as it is evident from the analysis with the 2 bins that both the realistic and the conservative scenarios yield comparable results on S_8 that are quite degenerate, yet not biased, with the density-only model.[4]

To understand this, let us draw the reader's attention to the galaxy bias fiducial values of Table 5.2, chosen for the reference cosmology to produce the mock data, it is evident that these values are quite large. This is normal since the EMU survey as a radio continuum experiment probes very high redshifts, where the galaxy bias is expected to be rather large. In addition to this, we have already proved that an incomplete model chosen to fit the correct data can sometimes be insufficient to describe it successfully, leading to a misplaced/biased peak of the posterior. This, along with the fact that the galaxy bias extends to high values, leads the incomplete model to make erroneous overestimates of the galaxy bias nuisance parameters, which are counterbalanced by a rather low and therefore biased measurement on σ_8, which is of course imprinted on S_8 as well.

[4]It is worth mentioning that this degeneracy is also shown on σ_8 for the cases of photometric and HI-galaxy surveys (see chapter 4), when one tries to fit mock data simulated assuming both density and RSD, against spectra including density fluctuations only.

TABLE 5.6: Same as Table 5.5, but for the case of 5 Gaussian bins.

5 Gaussian bins (ΛCDM)						
	Ideal scenario		Realistic scenario		Conservative scenario	
	den	den+mag	den	den+mag	den	den+mag
S_8	0.826 ± 0.027	0.827 ± 0.026	0.83 ± 0.20	0.818 ± 0.099	0.62 ± 0.11	0.75 ± 0.11
h	0.699 ± 0.059	0.684 ± 0.057	0.698 ± 0.057	0.680 ± 0.055	0.683 ± 0.075	0.669 ± 0.072

TABLE 5.7: Same as Table 5.5, but for DE.

2 Gaussian bins (DE)						
	Ideal scenario		Realistic scenario		Conservative scenario	
	den	den+mag	den	den+mag	den	den+mag
S_8	0.78 ± 0.10	0.883 ± 0.083	0.92 ± 0.30	0.84 ± 0.10	0.77 ± 0.25	0.82 ± 0.10
h	0.68 ± 0.16	0.61 ± 0.13	0.66 ± 0.13	0.58 ± 0.13	0.74 ± 0.15	0.66 ± 0.12
w_0	0.10 ± 0.66	-0.96 ± 0.63	0.02 ± 0.67	-1.22 ± 0.66	0.48 ± 0.55	-0.84 ± 0.78
w_a	-2.8 ± 1.5	-0.8 ± 1.8	-2.2 ± 1.4	-0.6 ± 1.4	-2.4 ± 1.1	-1.2 ± 1.6

Despite this peculiar result for the incomplete model in the conservative scenario for the 5 bins, generally the biased estimates with the wrong model are those in the analysis with 2 very wide bins described in the previous subsection. This leads to the conclusion that the magnification contributing to the galaxy clustering is very significant, and it may not be neglected when wide redshift bins are chosen. This makes sense, too, since the magnification bias of Equation 6.6 is an integrated effect, implying that the wider the redshift range of the sources who are inside the bin, the more enhanced the effect of the magnification will be, leading to important biases when it is not considered.

By comparing the results with the 2-bin case, one can easily appreciate that the constraints obtained with the five narrower bins are tighter, especially on h. This can be attributed to the fact that the parameter's effect on the power spectrum can be determined through an accurate determination of its redshift dependence, which is more precise with narrower redshift bins.

The findings for the case of 5 Gaussian bins are quantitatively summarised in Table 5.6.

5.5.4 Constraints on dark energy

Let us know move to the first extension to ΛCDM considered, namely dynamical DE as in subsection 5.3.1. The 68% marginal confidence intervals and means on the cosmological set $\{S_8, h, w_0, w_a\}$ are presented in Figure 5.3, Table 5.7, and Table 5.8.

Generally speaking, we find the same behaviour of constraints on S_8 and h as for ΛCDM, but there are a couple of points which nonetheless differ from the ΛCDM results. The former is that in this parameterisation, the density-alone model for the 5 bins yields a slightly biased result on h in the realistic scenario. The latter concerns

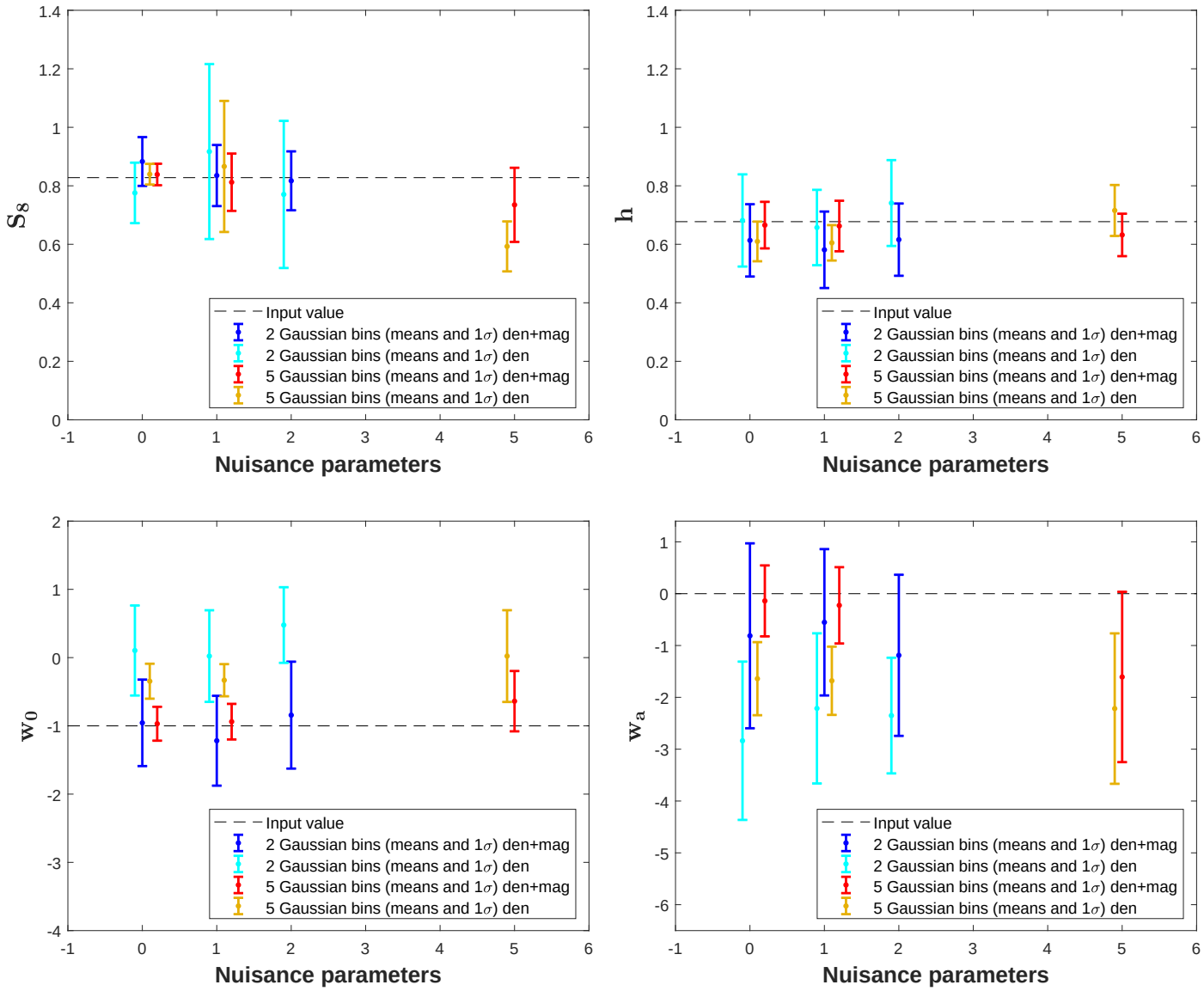

FIGURE 5.3: Same as Figure 5.2, but for the DE parameter set.

TABLE 5.8: Same as Table 5.6, but for DE.

	5 Gaussian bins (DE)					
	Ideal scenario		Realistic scenario		Conservative scenario	
	den	den+mag	den	den+mag	den	den+mag
S_8	0.840 ± 0.035	0.839 ± 0.037	0.87 ± 0.22	0.812 ± 0.098	0.593 ± 0.085	0.73 ± 0.13
h	0.610 ± 0.068	0.666 ± 0.080	0.605 ± 0.060	0.663 ± 0.086	0.716 ± 0.087	0.632 ± 0.072
w_0	-0.35 ± 0.26	-0.97 ± 0.25	-0.33 ± 0.24	-0.94 ± 0.26	0.02 ± 0.67	-0.64 ± 0.44
w_a	-1.64 ± 0.70	-0.14 ± 0.68	-1.68 ± 0.66	-0.22 ± 0.74	-2.2 ± 1.5	-1.6 ± 1.6

TABLE 5.9: Same as Table 5.5, but for modified gravity.

2 Gaussian bins (MG)						
	Ideal scenario		Realistic scenario		Conservative scenario	
	den	den+mag	den	den+mag	den	den+mag
S_8	0.897 ± 0.080	0.842 ± 0.062	0.97 ± 0.30	0.83 ± 0.11	0.84 ± 0.22	0.82 ± 0.11
h	0.60 ± 0.12	0.69 ± 0.12	0.59 ± 0.16	0.70 ± 0.13	0.70 ± 0.13	0.70 ± 0.13
Q_0	0.85 ± 0.23	0.77 ± 0.30	0.88 ± 0.23	0.80 ± 0.29	0.74 ± 0.32	0.73 ± 0.38
Σ_0	0.89 ± 0.12	0.89 ± 0.15	0.91 ± 0.12	0.91 ± 0.15	0.90 ± 0.15	0.91 ± 0.19

that, in particular, the idealistic case constraints are a bit weaker than the ΛCDM ones. This, of course, is due to the addition of the parameter set $\{w_0, w_a\}$, resulting in a larger statistical uncertainty in the posterior, keeping even the constraints for the wrong model and the 2 wide bins, consistent within 1σ from the reference cosmology. Apart from that, regardless of the binning, a correct modelling yields comparable results for the realist and the conservative case, within 68% from the fiducial values.

If we now focus on $\{w_0, w_a\}$, which constitutes one of the main points of our work. It is evident that for any binning applied in the density-only model, since the reconstructed results are always biased on both parameters whether we introduce nuisance parameters to be marginalised over or not. In detail, we see that the picture of the analysis with the 2 bins is independent of the status of knowledge of the galaxy bias. The same is true for the 5 bins, apart form the conservative case where we get weakened results. It is worth noticing again that from the two configurations, the 5-bin choice yields better constraints. Indeed, after having a look at the mean values estimated by the incomplete model, we can really appreciate that the bias is more pronounced with the wider bins (cyan error bars compared to yellow ones). Generally, it is obvious that the correct model (blue in the 2-bin and red in the 5-bin case) always accepts the fiducial values $w_0 = -1$ and $w_a = 0$ within the 68% marginal error.

Given these results, we infer that fitting the mock data with the complete model containing the same full information (density fluctuations and magnification) does not point to a spurious DE extension of the ΛCDM model, which would not otherwise be the case if we ignored the magnification. This demonstrates the fact that the inclusion of the magnification bias on the galaxy density field is indispensable, in order to avoid misinterpretation of the results on the cosmological parameter estimation.

5.5.5 Constraints on modified gravity

Finally, Figure 5.4, Table 5.9, and Table 5.10 present the parameter constraints on the modified gravity model parameters $\{S_8, h, Q_0, \Sigma_0\}$.

We see that for the 2-bins and for both the wrong (cyan error bar) and the correct (blue error bar) model, the results on $\{S_8, h\}$ are always within 68% from the fiducial

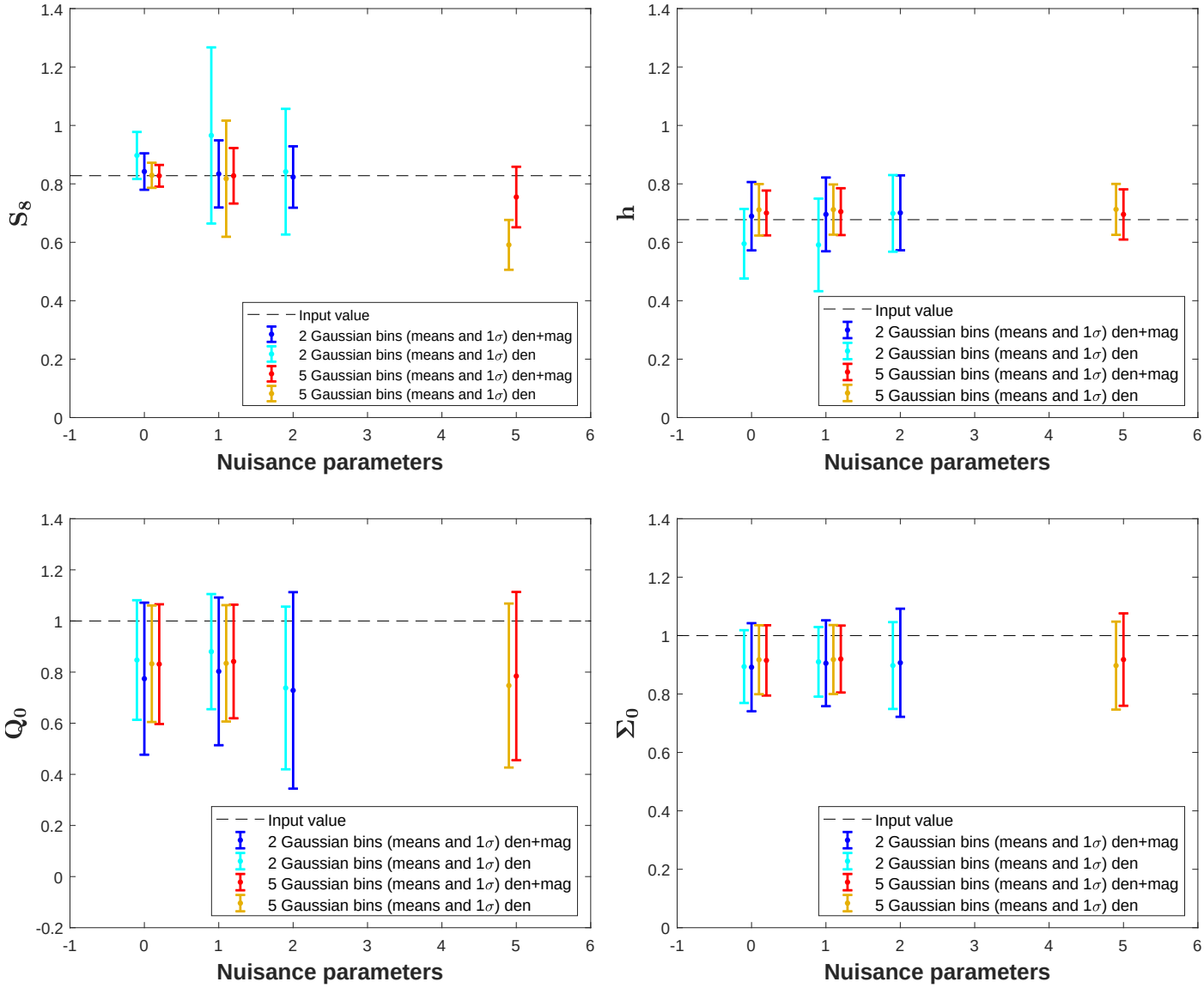

FIGURE 5.4: Same as Figure 5.2, but for the modified gravity parameter set.

TABLE 5.10: Same as Table 5.6, but for modified gravity.

	5 Gaussian bins (MG)					
	Ideal scenario		Realistic scenario		Conservative scenario	
	den	den+mag	den	den+mag	den	den+mag
S_8	0.829 ± 0.043	0.828 ± 0.037	0.82 ± 0.20	0.83 ± 0.095	0.591 ± 0.085	0.75 ± 0.10
h	0.711 ± 0.088	0.700 ± 0.077	0.712 ± 0.086	0.705 ± 0.080	0.713 ± 0.087	0.700 ± 0.086
Q_0	0.83 ± 0.23	0.83 ± 0.23	0.83 ± 0.23	0.84 ± 0.22	0.75 ± 0.32	0.78 ± 0.33
Σ_0	0.93 ± 0.12	0.92 ± 0.12	0.92 ± 0.12	0.92 ± 0.11	0.90 ± 0.15	0.92 ± 0.16

values, and once again the same pattern follows, with the degeneracy on S_8 and its alleviation after magnification is added in the realistic and the conservative case, which again give comparable results. When it comes to the narrower 5 bins, we have a similar behaviour with the exception that the constraints are more stringent, and there is a biased underestimation of the S_8 with the incomplete model (yellow error bar) in the conservative case. Also, the constraining power here for both binning scenarios on the set $\{S_8, h\}$ is similar to the case of DE.

Concerning the modified gravity parameters $\{Q_0, \Sigma_0\}$, if any of these two parameters deviates from unity, this would indicate that the ΛCDM model possibly needs to be replaced by a modified theory of gravity. Nonetheless, we can see for both binning configurations and both models that the results are comparable, while all the estimates are unbiased with respect to the fiducial input value. In addition, the narrower 5 redshift bins yield slightly tighter constraints than the 2-bin case.

Overall, we can conclude that even after ignoring the magnification correction in galaxy clustering, we are not able to see a biased result on the $\{Q_0, \Sigma_0\}$ that would, incorrectly of course, imply that the vanilla ΛCDM model is not the complete theory to describe the mock data.

5.5.6 Including RSD

At last, we examine the impact of RSD in the analysis. In chapter 4, we have already presented results that show, for optical/near-IR and radio HI-line galaxy surveys, that if one neglects RSD when fitting against the data, one can induce biases in the cosmological parameter estimation.

In this case, we create the mock data including all terms in Equation 5.2. We focus on the idealistic scenario, where the galaxy bias is perfectly known, as if no deviation from the results described above is found in this case, we even less expect to see any for the realistic and conservative cases. We constrain the parameter set $\{\Omega_m, h, \sigma_8\}$ with four different constructions of the theory vector: *i*) density only; *ii*) density and magnification (these two corresponding to what discussed in the previous subsections); *iii*) density and RSD; *iv*) and density, RSD, and magnification.

Figure 5.5 presents the results for the four different models considered. The left panels show the constraints on the set $\{S_8, h\}$ for the 2-bin case. It is clear that there are biased estimates when the theory model includes the density fluctuations alone or the density along with the RSD correction, neglecting in both cases the magnification bias. On the contrary, the theory model that contains the full information (density, RSD and magnification) as the mock data is well within 68% from the reference fiducial values, and so does the model which considers the density field and the magnification flux, but ignoring now RSD. As for the results of the 5-bin case shown in the right panels, it is obvious that the constraints are better on both S_8 and h, while there are no biased estimates at all with any of the three incomplete models tested.

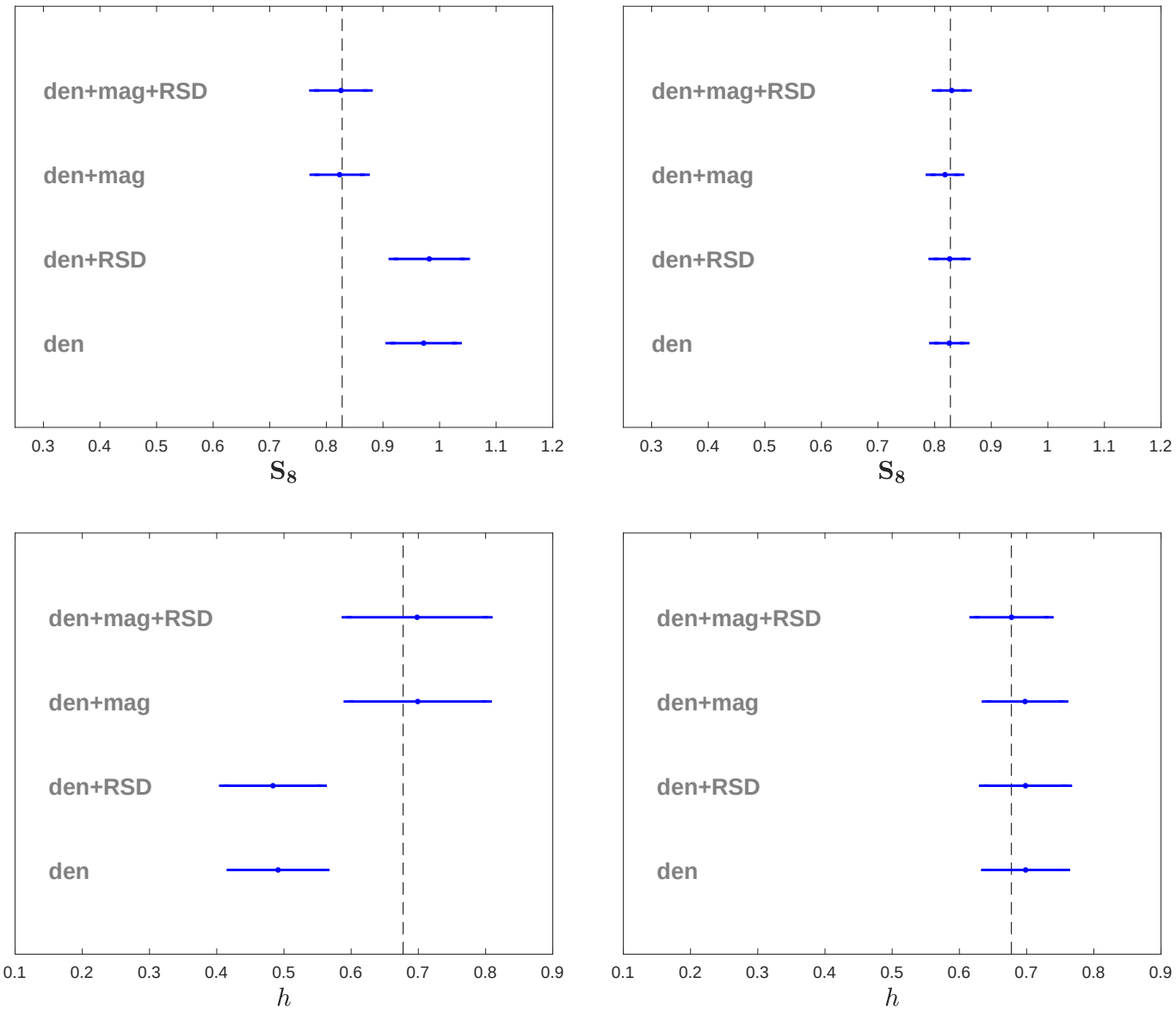

FIGURE 5.5: EMU mean and 68% constraints on the derived S_8 (top) and h (bottom), cosmological parameter for 2 (left) and 5 (right) Gaussian bins in a ΛCDM model where the galaxy bias is known exactly. Note that the data to be fitted are constructed incorporating both RSD and the magnification bias correction on the galaxy density field in a ΛCDM fiducial cosmology (vertical dashed line).

The above results, lead to the conclusion that the inclusion or the ignorance of the RSD correcting term on the galaxy number counts, cannot affect our analysis at any extend, and can be safely ignored in our study. The reason behind this is the very large width of the redshift bins. Even when subdividing the redshift galaxy distribution into 5 bins, they are still quite wide in the redshift space, thus leading to a washing out of the RSD effect. Oppositely, narrower bins call for the inclusion of RSD (see chapter 4). On the other hand, this test provides a further confirmation that in the case of radio continuum surveys like EMU, the magnification bias ought to be included in the modelling, in order to avoid potential biases in the cosmological parameter estimation.

Chapter 6

Implementing the multi-tracer technique to constrain neutrino masses

6.1 Formalism

Let us start with a set of:

- $N_{\rm tr}$ tracers of the underlying large-scale cosmic structure (different galaxy populations, in the present case), labelled by upper-case Latin letters from the beginning of the alphabet, viz. $A, B \ldots$;
- N_z^A redshift bins (for the Ath galaxy sample, in this case), labelled by lower-case Latin letters from the middle of the alphabet, e.g. $i, j \ldots$

Now, the harmonic-space power spectrum of the clustering between A-type galaxies in redshift bin i and B-type galaxies in redshift bin j, $C_\ell^{\rm g}(z_i^A, z_j^B)$ is given by Equation 3.131 and in the case of different galaxy samples is written as

$$\left\langle g_{\ell m}^{A,i} g^{*B,j}_{\ell' m'} \right\rangle = \delta^{\rm K}_{\ell\ell'} \delta^{\rm K}_{mm'} C_\ell^{\rm g}(z_i^A, z_j^B), \tag{6.1}$$

where e.g. $g_{\ell m}^{A,i}$ now indicates the spherical-harmonic expansion coefficients of the sky map of the distribution of the A-th tracer in the i-th redshift bin. Clearly, the case $A = B$ reduces to the standard single-tracer analysis, whereas $i = j$ means restricting to auto-bin correlations.

If we focus on the main contributions to galaxy number density fluctuations—namely matter density perturbations, RSD, and magnification (see e.g. Yoo, 2010; Challinor and Lewis, 2011a; Bonvin and Durrer, 2011)—the theoretical expectation of the harmonic-space power spectrum in a given cosmology can be computed in the Limber approximation as we have already seen in chapter 4 and chapter 5 (we write it again for clarity since we introduce different galaxy samples) via

$$C^{\rm g}_{\ell \gg 1}(z_i^A, z_j^B) = \int \frac{{\rm d}\chi}{\chi^2} \, W_{\rm g}^{A,i}(k_\ell, \chi) W_{\rm g}^{B,j}(k_\ell, \chi) P_{\rm lin}\left(k_\ell\right), \tag{6.2}$$

where $k_\ell = (\ell + 1/2)/\chi$, whilst

$$W_{\rm g}^{A,i}(k_\ell, \chi) = W_{\rm g,den}^{A,i}(k_\ell, \chi) + W_{\rm g,RSD}^{A,i}(k_\ell, \chi) + W_{\rm g,mag}^{A,i}(k_\ell, \chi) \tag{6.3}$$

is the total weight function for each galaxy population and redshift bin pair. The three terms of Equation 6.3 respectively read:

$$W_{\rm g,den}^{A,i}(k_\ell, \chi) = n_i^A(\chi) b_i^A(k_\ell, \chi) D(k_\ell, \chi), \tag{6.4}$$

for matter density fluctuations;

$$\begin{aligned} W_{\rm g,RSD}^{A,i}(k_\ell, \chi) = & \frac{2\ell^2 + 2\ell - 1}{(2\ell - 1)(2\ell + 3)} n_i^A(\chi) \left[fD\right](k_\ell, \chi) \\ & - \frac{(\ell - 1)\ell}{(2\ell - 1)\sqrt{(2\ell - 3)(2\ell + 1)}} n_i^A\left(\frac{2\ell - 3}{2\ell + 1}\chi\right) \left[fD\right]\left(k_\ell, \frac{2\ell - 3}{2\ell + 1}\chi\right) \\ & - \frac{(\ell + 1)(\ell + 2)}{(2\ell + 3)\sqrt{(2\ell + 1)(2\ell + 5)}} n_i^A\left(\frac{2\ell + 5}{2\ell + 1}\chi\right) \left[fD\right]\left(k_\ell, \frac{2\ell + 5}{2\ell + 1}\chi\right), \end{aligned} \tag{6.5}$$

for RSD; and

$$W_{\rm g,mag}^{A,i}(k_\ell, \chi) = \frac{3\Omega_{\rm m} H_0^2}{c^2} \left[1 + z(\chi)\right] \chi \tilde{n}_i^A(\chi) \left[\mathcal{Q}(\chi) - 1\right] D(k_\ell, \chi), \tag{6.6}$$

for magnification.

It is important to note that in Equation 6.2 and below we have included the scale dependence inside the kernels since we are interested in studying cosmology with massive neutrinos. The following new quantities are: ; the linear scale dependent galaxy bias, $b(k, z)$; the growth factor, defined as $D(k, z) = \sqrt{P_{\rm lin}(k, z)/P_{\rm lin}(k)}$; the growth rate of matter perturbations, $f(k, z) = -(1 + z)\mathrm{d} \ln T(k, z)/\mathrm{d}z$, with $T(k, z)$ the transfer function (and not just the growth factor $D(z)$ since now we introduce a scale dependence on the growth rate); the source redshift distribution of the A-th galaxy population in the i-th redshift bin, $n_i^A(z)$,[1] and in Equation 6.6 the lensing efficiency (given by Equation 3.120) for each redshift bin and galaxy population $\tilde{n}_i^A(\chi)$.

6.2 The survey

To investigate better the potentiality of multi-tracing, we choose to adopt as a reference experiment one that can simultaneously detect different galaxy populations. In particular, we focus on the DESI (Aghamousa et al., 2016), a ground-based large-scale structure experiment that has recently started its five year active period (as of the second half of 2020). It aims at measuring the baryon acoustic oscillations and the growth of structures via RSD. It will be a wide-area survey of $14,000\,\mathrm{deg}^2$ with a target list of galaxies and quasars observed spectroscopically. The target imaging objects are divided in three classes according to their redshift range. The very low

[1] Note again that for any source distribution $n(z)\,\mathrm{d}z = n(\chi)\,\mathrm{d}\chi$ holds.

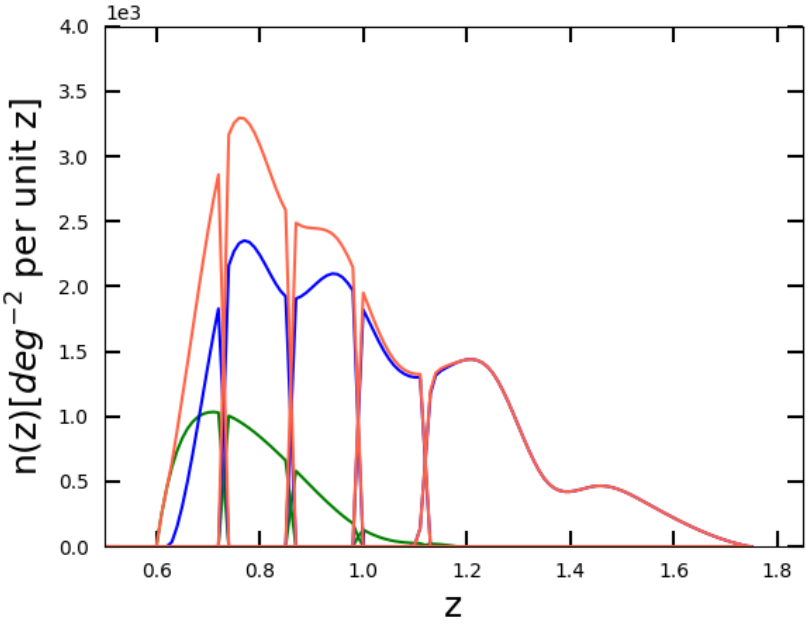

FIGURE 6.1: The total DESI (red) and the ELG (blue) and LRG (green) galaxy sub-sample distributions in redshift.

redshift objects ($z < 1$) will be the luminous red galaxies (hereafter LRG), whilst those in the intermediate redshifts ($1 < z < 1.7$) will be bright oxygen emission line galaxies (hereafter ELG). Finally, at very high redshifts ($2.1 < z < 3.5$), quasars will be traced thanks to their neutral hydrogen distribution using the Ly-α forest absorption lines. Here, however, we will only consider the ELG and LRG galaxy sub-samples, and shall refer to the total DESI galaxy sample as their summed distribution. The ELG and LRG distributions as a function of redshift are presented in Table 6.1. We divide both samples in such a way that each bin's edges coincide between the tracers, in order to fully exploit the overlap binning for the multi-tracer technique (see Figure 6.1). We consider four equi-spaced z-bins for each tracer apart form the last one, where the LRG number density is almost zero and the ELG extents to the end of the sample in redshift.

Let us consider that at a given redshift range $\mathrm{d}z$ the number of galaxies residing there is $\mathrm{d}N$, and the distribution of sources reads $n(z) = \mathrm{d}N/\mathrm{d}z$. Assuming that $N(z)$ are the points shown in Table 6.1, we can interpolate with a better sampled distribution $n(z)$ which will be the total source number counts as a function of redshift. Thus, inside a bin i of the A-th galaxy population, $n_i^A(z)$ galaxies reside, and the total number counts of galaxies is

$$\bar{n}^A = \sum_i \bar{n}_i^A, \tag{6.7}$$

TABLE 6.1: The DESI galaxy ELG and LRG sub-samples for an sky area coverage $14,000\,\mathrm{deg}^2$ as given in Aghamousa et al. (2016).

z	$\mathrm{d}N_{\mathrm{ELG}}/\mathrm{d}z/\mathrm{d}\Omega\,[\mathrm{deg}^{-2}]$	$\mathrm{d}N_{\mathrm{LRG}}/\mathrm{d}z/\mathrm{d}\Omega\,[\mathrm{deg}^{-2}]$
0.65	309	832
0.75	2269	986
0.85	1923	662
0.95	2094	272
1.05	1441	51
1.15	1353	17
1.25	1337	0
1.35	523	0
1.45	466	0
1.55	329	0
1.65	126	0
1.75	0	0
1.85	0	0

whilst each bin's angular number count of sources reads

$$\bar{n}_i^A = \int \mathrm{d}z\, n_i^A(z). \tag{6.8}$$

Since the galaxies will be observed spectroscopically we choose a top-hat modelling (given by Equation 4.17 and Equation 5.7 but we write it again here for clarity) for the binning such that

$$n_i^A(z) = \frac{1}{2}\left[1 - \tanh\left(\frac{|z-\bar{z}_i| - \Delta z/2}{r\Delta z/2}\right)\right], \tag{6.9}$$

with $\bar{z}_i$ the i-th bin centre, Δz the bin width, and r an edge smearing, which we chose to be 0.03. We note again that the smearing of the bin edges mostly ensures that the integration will be numerically stable.

The linear galaxy bias on scales $k \ll k_{\mathrm{nr}}$ for the ELG and LRG galaxy samples is given by (Aghamousa et al., 2016) as $b_{\mathrm{LRG}}(z) = 1.7/D(k \ll k_{\mathrm{nr}}, z)$ and $b_{\mathrm{ELG}}(z) = 0.84/D(k \ll k_{\mathrm{nr}}, z)$, whilst for the DESI distribution we choose a weighted average, i.e.

$$b_{\mathrm{DESI}}(z) = \frac{n_{\mathrm{LRG}}(z)b_{\mathrm{LRG}}(z) + n_{\mathrm{ELG}}(z)b_{\mathrm{ELG}}(z)}{n_{\mathrm{LRG}}(z) + n_{\mathrm{ELG}}(z)}. \tag{6.10}$$

6.3 Neutrinos free streaming length and scale dependent galaxy bias

The comoving free-streaming scale is a redshift dependent quantity defined as

$$k_{\mathrm{fs}}(z) = \sqrt{1.5}\frac{H(z)}{u_{\mathrm{th}}(1+z)}, \tag{6.11}$$

with $u_{\rm th}$ the neutrino thermal velocity. When neutrinos are relativistic, their $k_{\rm fs}$ decreases as in Equation 6.11. However, after neutrinos become non-relativistic, their thermal velocity starts to decay as

$$u_{\rm th} \approx \frac{3T_\nu}{m_\nu} \tag{6.12}$$

$$= 3(4/11)^{1/3}\frac{T_\gamma^0}{m_\nu}(1+z) \tag{6.13}$$

$$\approx 151(1+z)\left(\frac{1\,{\rm eV}}{m_\nu}\right)\,{\rm km\,s^{-1}}, \tag{6.14}$$

where m_ν the neutrino eigenstate mass in eV and $T_\gamma^0 = 2.725'\,{\rm K}$ the photon temperature today. Then, the free-streaming scale for the non-relativistic neutrinos becomes

$$k_{\rm fs} \approx 0.81\frac{\sqrt{\Omega_\Lambda + \Omega_{\rm m}(1+z)^3}}{(1+z)^2}\left(\frac{m_\nu}{1\,{\rm eV}}\right) h\,{\rm Mpc}^{-1}. \tag{6.15}$$

The redshift of the transition between relativistic and non-relativistic regimes is

$$1 + z_{\rm nr} \approx 1980\left(\frac{m_\nu}{1\,{\rm eV}}\right), \tag{6.16}$$

after which the free-streaming scale starts to grow, since $k_{\rm fs} \propto (1+z)^{-1/2}$, passing a minimum corresponding to

$$k_{\rm nr} \approx 0.018\left(\frac{m_\nu}{1\,{\rm eV}}\right)^{1/2}\sqrt{\Omega_{\rm m}}h\,{\rm Mpc}^{-1}. \tag{6.17}$$

Modes with $k > k_{\rm fs}$ result in the suppression of the growth of the CDM perturbations due to the weakening of the gravitational potential wells, whilst for $k < k_{\rm fs}$ perturbations are free to grow again. Free-streaming never affects modes with $k < k_{\rm nr}$, and the neutrino fluctuations evolve similarly to the CDM ones since the two fields are coupled. Nonetheless, the baryon perturbations remain suppressed and are free to grow in amplitude only after the matter-radiation decoupling, falling on the already formed gravitational neutrino damped CDM potentials. Thus, the galaxy bias, b, which is the amplitude of the matter clustering ought to be properly modelled accounting for scale dependence for studies concerning massive neutrinos. This is also true for the growth rate of structures, f, which is sensitive to neutrinos.

For the scale dependent galaxy bias due to massive neutrinos we use the recipe presented in Castorina et al., 2014. According to this, the galaxy bias can be written with two definitions depending on the choice of the total matter or just the CDM and the baryon component, namely

$$b^{\rm m} = \sqrt{P_{\rm lin}^{\rm g}/P_{\rm lin}}, \tag{6.18}$$

$$b^{\rm CDM+b} = \sqrt{P_{\rm lin}^{\rm g}/P_{\rm lin}^{\rm CDM+b}}, \tag{6.19}$$

with $P_{\rm lin}^{\rm g}$ and $P_{\rm lin}^{\rm CDM+b}$ the linear power spectra of clustering of galaxies and the

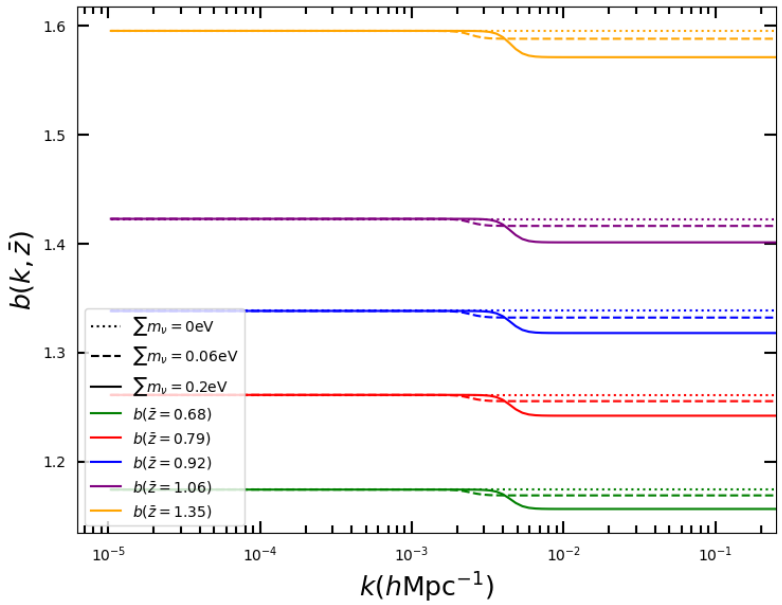

FIGURE 6.2: Scale dependent galaxy bias as a function of scale, with increasing redshift taken at the centre of each bin (see legend for colors). The scale-dependent bias is shown with dotted lines for $\sum m_\nu$=0eV, with dashed for $\sum m_\nu$=0.06eV and with solid for $\sum m_\nu$=0.2eV. The reference galaxy sample is the ELG catalogue.

CDM+baryon component, respectively. However, the galaxy formation is expected to be relevant for $k > k_{\rm fs}$, where neutrinos do not cluster. Thus, it is more precise to assume that the galaxies trace the field of the CDM+baryon perturbations and not the total matter field which includes neutrinos (Vagnozzi et al., 2018) and hence opt for $b^{\rm CDM+b}$ as a definition of the galaxy bias.

In the case of ΛCDM cosmology with massive neutrinos and for $k \ll k_{\rm nr}$, the $b^{\rm m}$ and $b^{\rm CDM+b}$ converge since the total matter power spectrum and the CDM+baryon power spectrum are the same, whilst for $k \gg k_{\rm nr}$ but well inside the linear regime we have the behaviour

$$b^{\rm m} \to b^{\rm CDM+b}(1 - f_\nu). \tag{6.20}$$

where $f_\nu = \Omega_\nu/\Omega_{\rm m}$ with $\Omega_\nu = \sum m_\nu/(93.14h^2)$. Apart from this recipe for the scale dependent galaxy bias in section C.1 we describe another one by (LoVerde, 2016).

In order to account for a smooth transition for the linear galaxy bias values between $k \ll k_{\rm nr}$ and $k \gg k_{\rm nr}$, we use the expression

$$b(k,z) = b_{k\ll k_{\rm nr}}(z) + \frac{[b_{k\gg k_{\rm nr}}(z) - b_{k\ll k_{\rm nr}}(z)]}{2}\left\{\tanh\left[\ln\left(\frac{k}{k_{\rm nr}}\right)^{\gamma}\right] + 1\right\}, \tag{6.21}$$

with $b_{k\ll k_{\rm nr}}$ or $b_{k\gg k_{\rm nr}}$ the galaxy bias in the two asymptotic regimes and γ setting the sharpness of the transition, for which we choose the value of 5—note that the

actual value of γ does not impact the results. In Figure 6.2, we show the galaxy bias as a function of scale for different redshifts corresponding to the centres of each bin for the ELG galaxy sample (for colors, see legend). Solid, dashed and dotted lines are for $\sum m_\nu = 0.2, 0.06, 0\,\mathrm{eV}$, respectively. It is evident that the amplitude of the transition and its position in scale is strongly dependent on the neutrino mass (see Equation 6.17 and Equation 6.20).

6.4 Likelihood and scale cuts

Similarly to chapter 4 and chapter 5, we plan to forecast cosmological parameters with a Bayesian approach. For that purpose, we set up a Monte Carlo Markov Chain sampling of the parameter posterior in the cosmological+nuisance parameter hyper-space. We assume the familiar Gaussian likelihood for the data and minimise the chi-square function (we write again the quantities for the clarity of the multi-tracer method)

$$\chi^2(\boldsymbol{\theta}) = \sum_{\ell,\ell'=\ell_{\rm min}}^{\ell_{\rm max}} \left[\boldsymbol{d}_\ell^{AB} - \boldsymbol{t}_\ell^{AB}(\boldsymbol{\theta})\right]^{\mathsf{T}} \left(\boldsymbol{\Gamma}_{\ell\ell'}^{AB}\right)^{-1} \left[\boldsymbol{d}_\ell^{AB} - \boldsymbol{t}_\ell^{AB}(\boldsymbol{\theta})\right]. \tag{6.22}$$

In Equation 6.22, $\boldsymbol{d}_\ell^{AB} = [\boldsymbol{C}_\ell^{\rm g}(z_i^A, z_j^B)]$ is the data vector, constructed for our fiducial cosmological model at $\boldsymbol{\theta}_{\rm fid}$ by flattening the $N_z^A \times N_z^B$ tomographic matrix in each of its N_ℓ multipole bins; $\boldsymbol{t}_\ell^{AB}(\boldsymbol{\theta})$ is the corresponding theory vector. We remind the reader that A, B label the galaxy sample, namely ELG or LRG.

For the data, we assume a Gaussian covariance matrix, which takes the signal input of Equation 6.2 and reads

$$\Gamma_{\ell\ell'}^{ij,A;mn,B} = \frac{\delta_{\rm K}^{\ell\ell'}}{2\ell\Delta\ell f_{\rm sky}} \times \left[\widetilde{C}_\ell^{\rm g}(z_i^A, z_m^B)\widetilde{C}_\ell^{\rm g}(z_j^A, z_n^B) + \widetilde{C}_\ell^{\rm g}(z_i^A, z_n^B)\widetilde{C}_\ell^{\rm g}(z_j^A, z_m^B)\right], \tag{6.23}$$

and

$$\widetilde{C}_\ell^{\rm g}(z_i^A, z_j^B) = C_\ell^{\rm g}(z_i^A, z_j^B) + \frac{\delta_{\rm K}^{ij}\delta_{\rm K}^{AB}}{\bar{n}_i^A}, \tag{6.24}$$

is the observed signal+noise, with $\bar{n}_i^A$ defined in Equation 6.8.

It is worth remarking that:

- $A = B$ represents the two single-tracer cases of ELG-ELG and LRG-LRG auto-correlation power spectra;
- $A \neq B$ is the ELG-LRG cross-correlation;
- the multi-tracer case is obtained by flattening the data and theory vectors, as well as the covariance matrix, along the A, B indexes, too, thus considering at the same time all auto- and cross-correlations between the different galaxy samples.

TABLE 6.2: The lower and upper multipole cuts for the LRG, ELG galaxy samples, and their summed total DESI distribution. The $\ell_{\rm min}$ is set as the point where the relative error between the angular power spectra measurement of `CosmoSIS` and `CLASS` is less than 5%, whilst in the linear regime limit the upper cut is specified as $\ell_{\rm max} = \chi(\bar{z}_i)k_{\rm max}$, where $\bar{z}_i$ is the ith bin centre.

$\ell_{\rm min}$			$\ell_{\rm max}$
LRG	ELG	DESI	
63	124	119	611
78	82	108	705
98	99	125	791
166	133	170	872
176	20	20	(946)1075

The multipole range where the angular power spectra of Equation 6.2 are calculated is comprised between a lower $\ell_{\rm min}$ and an upper $\ell_{\rm max}$ cut. The lower limit is set due to the fact that the Limber approximation holds for $\ell \gg 1$. Following the same fashion of chapter 4 and chapter 6, we compare our Limber approximated `CosmoSIS` spectra with the full spectra provided by `CLASS` (Lesgourgues, 2011; Blas, Lesgourgues, and Tram, 2011; Di Dio et al., 2013), and hence set the $\ell_{\rm min}$ where the relative error between the two spectra is less than 5%. We note again that this choice is justified since this difference is always inside the 1σ theory error bar of the signal measurement. The choice of the upper bound $\ell_{\rm max}$ is made due to the fact that we consider only the linear scales in our analysis. This cut is defined as $\ell_{\rm max} = \chi(\bar{z}_i)k_{\rm max}$, where $\bar{z}_i$ is the centre of each redshift bin and the maximum wavelength reads $k_{\rm max} = \pi/(2R_{\rm min})$, with $R_{\rm min}$ the sphere radius inside which the overdensity perturbations at present have a variance given by Equation 4.19 and is set to $\sigma^2(R_{\rm min}) = 1$ corresponding the $k_{\rm max} = 0.25\,h\,{\rm Mpc}^{-1}$. The lower and the upper multipole cuts (shown in Table 6.2) are imposed in all the redshift bins of the LRG and ELG galaxy samples, as well as their summed total DESI distribution (see again Figure 6.1). We should note that the ℓ_{max} for the 5-th bin of the LRG sample is different than that of the ELG and DESI due to the lower $\bar{z}$ considered. This choice is reasonable since the LRG number density of galaxies in that bin goes quickly to zero as already explained in section 6.2. In this analysis, we employ N_ℓ=20 log-spaced multipole bins.

We have checked that for the particular spectroscopic binning width choice the magnification bias correction is not affecting our analysis and therefore its contribution can be safely neglected (more about the importance of this effect on chapter 5). This is in agreement with the findings of Jelic-Cizmek et al., 2020.

6.5 Results

To test the multi-tracer technique applied to harmonic-space power spectra and our data analysis pipeline, we here aim to compare the constraints on the cosmological

TABLE 6.3: Cosmological and nuisance parameters fiducial values (the ΛCDM best-fit of Ade et al. 2016) with their priors. We consider on top of the ΛCDM model the case of 1 massive and 2 massless neutrinos with a fiducial value set to the minimum mass $\sum m_\nu$=0.06eV.

Parameter description	Parameter symbol	Fiducial value	Prior type	Prior range
Present-day fractional matter density	$\Omega_{\rm m}$	0.3089	Flat	$[0.1, 0.6]$
Dimensionless Hubble parameter	h	0.6774	Flat	$[0.5, 1.0]$
Amplitude of clustering‡	σ_8	0.8159	Flat	$[0.4, 1.2]$
Present-day physical fractional neutrino density	$\Omega_\nu h^2$	0.00064 ($\sum m_\nu$=0.06eV)	Flat	$[0.00064, 0.05]$
Present-day fractional baryon density	$\Omega_{\rm b}$	0.0486	–	–
Slope of the primordial curvature power spectrum	n_s	0.9667	–	–
Amplitude of the primordial curvature power spectrum‡	$\ln(10^{10}A_{\rm s})$	3.064	–	–
Optical depth to reionisation	$\tau_{\rm re}$	0.066	–	–
Overall redshift range amplitude bias parameter¶	α	1.0	Flat	$[0.1, 2.0]$
Per redshift bin amplitude bias parameter§	b_i $i = 1 \ldots 5$(10 for multi-tracing)	1.0	Flat	$[0.1, 2.0]$

‡ Following the LSS convention, we choose to sample on the σ_8 parameter to account for the matter perturbations amplitude and not on the primordial amplitude $A_{\rm s}$.
¶ Applied parameter prior range for the 'realistic' scenario (notation mirrors that of chapter 4, chapter 5).
§ Applied parameter prior range for the 'conservative' scenario .

parameter set $\boldsymbol{\theta}_{\Lambda\text{CDM}+\sum m_\nu} = \{\Omega_{\rm m}, h, \sigma_8, \Omega_\nu h^2\}$

(where we include 1 massive and 2 massless neutrinos) provided by the LRG and ELG galaxy sub-samples, the DESI total sample, and multi-tracing between LRG and ELG. We include nuisance parameters that need to be marginalised over, to account for the ignorance that we have on the galaxy bias. In this respect, we explore both of the following scenarios:

1. A realistic case, with an overall normalisation nuisance parameter spanning the whole redshift range.

2. A conservative choice of a nuisance parameter per redshift bin.

It is important to note that, as optimistic as the realistic case may seem, the analysis done in chapter 4 showed no substantial difference with the conservative choice in the final results and therefore we deem this case worthy of investigation here.

For the forecasting analysis, we use the Bayesian sampler `emcee` (Foreman-Mackey et al., 2013). For the four aforementioned galaxy samples, we construct the mock observables (data vector $\boldsymbol{d}_\ell^{AB}$ and covariance matrix given by Equation 6.23) within a fiducial ΛCDM+$\sum m_\nu$ with fixed scale dependent galaxy bias considering the RSD correction on the galaxy density field (the fiducial values are shown in Table 6.3). Then, we explore the parameter space of the set $\boldsymbol{\theta}_{\Lambda\text{CDM}+\sum m_\nu}$ along with the nuisance parameters (for the priors see again Table 6.3) until we reach convergence with the sampler. In the analysis of chapter 4 and chapter 5 we studied the effect of ignoring galaxy clustering corrections like RSD and magnification bias on the estimated cosmological parameter set. Thus, the resulting posteriors were expected to be biased described by highly non-Gaussian and/or bimodal shapes due to the incomplete information in our modelling. For that reason in the previous pieces of work we opted for the means. In the analysis here, however, we always fit the synthetic data with the same model (which is RSD on the density field and ΛCDM+$\sum m_\nu$ cosmology) and therefore feel safe to opt for the 1D marginalised peaks.

6.5.1 Realistic case

In Figure 6.3 we present the 1σ and 2σ contours on the parameter set $\{\Omega_\mathrm{m}, h, \sigma_8, \sum m_\nu\}$ for the LRG (green), ELG (blue), the multi-tracing (grey) and DESI (red) considering the realistic case with the galaxy bias as given by Equation 6.20. We keep the same contour colors in the whole analysis. The fiducial values used to generate the mock data and the priors for the Bayesian analysis are shown in Table 6.3 where we always include the RSDs correction on the galaxy density field. It is worth mentioning that the 2D contour of the Ω_m-h plane is quite skewed on the Ω_m direction. This is natural, since the neutrino fraction in the case of massive neutrinos is included in the total matter component and the uncertainty on the upper bound of their mass allows a higher Ω_m as well.

In detail, we see that constraints on the parameters of interest, namely the Ω_m, h, σ_8, and $\sum m_\nu$, from LRG are the weakest. The ELG distribution yields tighter constraints on the all the aforementioned parameters. This is expected, since the ELG has higher galaxy number density and the sample extents to a higher redshift range—note that the fifth bin for LRG is almost empty—containing in this way more cosmological information. The DESI combined distribution, as we have already mentioned, is the ELG and the LRG summed number density distribution with a weighted average galaxy bias given by Equation 6.10, and naturally yields better results on the whole parameter set than the two separate samples.

Finally, when we consider multi-tracing between LRG and ELG, we get even tighter constraints, particularly on the 2σ upper bound on the sum of the neutrino masses. This effectively means an enhancement of 24% with respect to the DESI bound. This is a major point in our analysis, attesting that with the multi-tracer technique we are able to considerably improve the results on the sum of the neutrino masses.

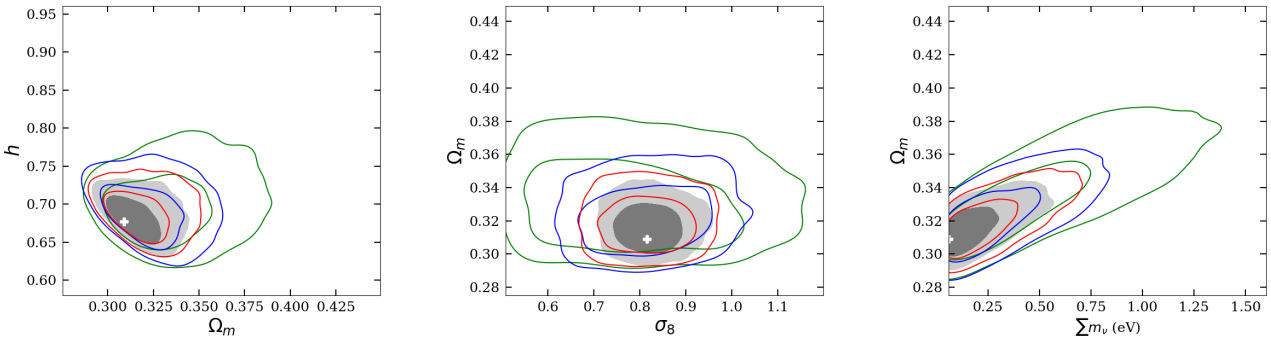

FIGURE 6.3: Cosmological parameter constraints for the realistic galaxy bias case relation. The outer and inner contours are respectively the 95% and 68% C.L. on the marginal joint two-dimensional parameter space. The green, blue, and red empty contours correspond to the LRG, ELG, and DESI whilst the multi-tracer is presented with grey filled contours. The white cross stands for the fiducial cosmology considered for the generation of the synthetic data.

In addition, the more precise measurement on the scale dependent galaxy bias thanks to multi-tracing is clear by looking at the left panel of Figure 6.5 where we see the marginalised 1D peak and the 1σ error on the normalisation galaxy bias parameter. Here we can appreciate that the multi-tracing (black) yields better constraints compared to those of the summed DESI galaxy distribution (red) by 30%. A similar trend can also be noticed on the σ_8 parameter (central panel of Figure 6.3), which is the normalisation of the power spectrum and is generally known to be degenerate with the galaxy bias (see again chapter 4 and chapter 5).

In subsection C.1.1 we present and discuss the results obtained using the recipe provided by LoVerde, 2016 in the realistic scenario. The general outcome is that we are not able to distinguish between the different galaxy sample cases and therefore we do not proceed with the conservative case following this recipe.

6.5.2 Conservative case

Similarly to the previous subsection, Figure 6.4 presents the constraints on the cosmological parameter set of interest for all the galaxy samples, adopting a realistic yet conservative scenario with a nuisance parameter per redshift bin ought to be marginalised over.

The results in the conservative case are quite similar to those obtained with the realistic scenario with the exception that the upper bounds on the sum of neutrino masses is weaker. This is a consequence of the fact that we have included more nuisance parameters in our modelling, and in particular galaxy bias parameters to which the neutrino masses are very sensitive, increasing in this way the measured error on this parameter. Generally, LRG yield again the weakest results, whilst better but comparable with each other are now the results obtained with ELG and DESI. This could also be attributed to the larger errorbars thanks to the extra parameters.

TABLE 6.4: Marginalised 1D peak values along with their 68% confidence level intervals on the cosmological parameter set $\{\Omega_m, h, \sigma_8\}$ as well as the 2σ (%95 CL) upper bound on the neutrino mass in eV. The results are obtained for the realistic scenario considering the LRG, and ELG galaxy sub-samples, the multi-tracer technique between them and the DESI total galaxy distribution.

	Realistic scenario			
	LRG	ELG	DESI	Multi-tracer
Ω_m	$0.3213^{+0.0251}_{-0.0146}$	$0.3206^{+0.0135}_{-0.0167}$	$0.3134^{+0.0154}_{-0.0086}$	$0.3166^{+0.0092}_{-0.0109}$
h	$0.6833^{+0.0394}_{-0.0258}$	$0.6854^{+0.0315}_{-0.0263}$	$0.6835^{+0.0257}_{-0.0197}$	$0.6801^{+0.0221}_{-0.0191}$
σ_8	$0.7310^{+0.1496}_{-0.1635}$	$0.8132^{+0.0981}_{-0.0990}$	$0.7872^{+0.0989}_{-0.0413}$	$0.8083^{+0.0577}_{-0.0410}$
$\sum m_\nu$ (95%CL)	<0.9801	<0.5782	<0.4857	<0.3686

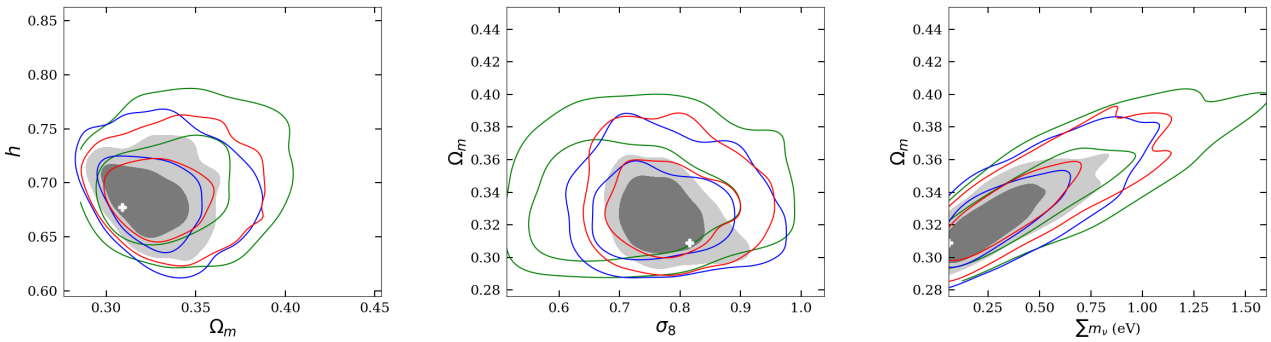

FIGURE 6.4: Same as Figure 6.3 but for the conservative scenario

The result of multi-tracing, however, are overall the most constraining again, having now a percentage gain of 44% with respect to the DESI upper 2σ bound on the sum of the neutrino masses.

Let us now focus on the constraints on the normalisation galaxy bias parameter per redshift bin, presented in the right panel of Figure 6.5. Here, we can appreciate that the 1σ error bars obtained with the multi-tracing corresponding to either the first tracer LRG (solid black line) or the second tracer ELG (dotted black line) are tighter than the the DESI error bars (solid red line) by $\sim$ 30%. This holds also true for the normalisation of the power spectrum σ_8, as we can see in the central panel of Figure 6.4. Finally, it is worth noting that the normalisation galaxy bias marginalised 1D peak values although consistent within 1σ with the fiducial value are slightly larger, counter balancing in this way the σ_8 marginalised 1D peak values which are oppositely a bit lower than the fiducial.

TABLE 6.5: Same as Table 6.4 the conservative scale dependent bias scenario

	Conservative scenario			
	LRG	ELG	DESI	Multi-tracer
Ω_m	$0.3159^{+0.0397}_{-0.0111}$	$0.3277^{+0.0159}_{-0.0230}$	$0.3257^{+0.0226}_{-0.0174}$	$0.3203^{+0.0192}_{-0.0135}$
h	$0.6868^{+0.0365}_{-0.0293}$	$0.6843^{+0.0279}_{-0.0227}$	$0.6835^{+0.0257}_{-0.0197}$	$0.6830^{+0.0271}_{-0.0178}$
σ_8	$0.6495^{+0.1673}_{-0.0536}$	$0.7165^{+0.1192}_{-0.0352}$	$0.7814^{+0.0509}_{-0.0845}$	$0.7656^{+0.0512}_{-0.0423}$
$\sum m_\nu$ (95%CL)	<1.1342	<0.7161	<0.7470	<0.4198

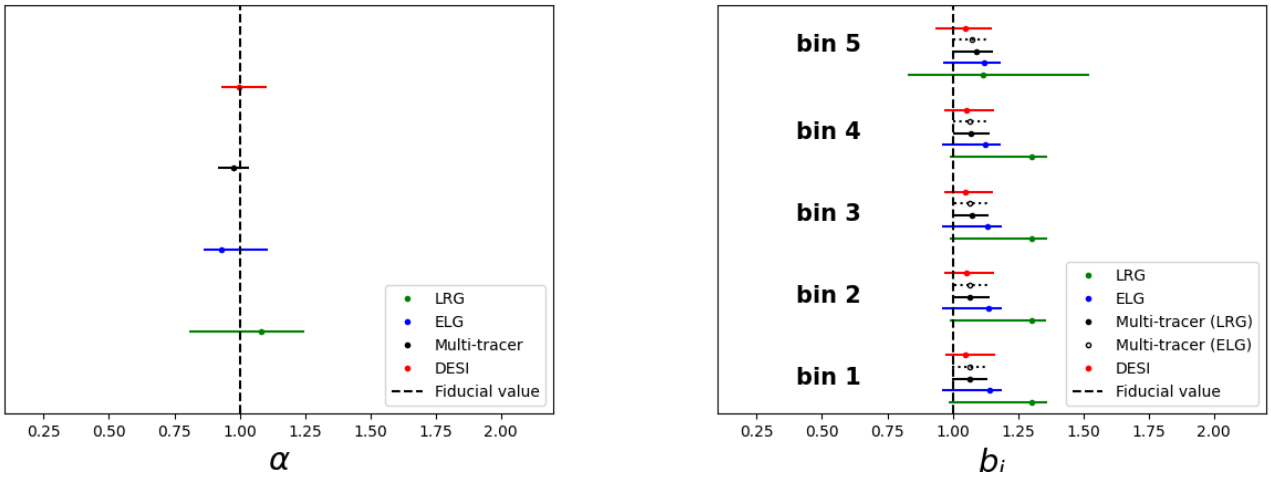

FIGURE 6.5: Marginalised 1D peak values (bullets) and the 68% confidence level asymmetric error bars (horizondal lines) for the realistic (left panel) and the conservative (right panel) amplitude galaxy bias parameters, considering the relation described by Equation 6.20. We denote with green the LRG, with blue the ELG, with black the multi-tracer, and with red the DESI results. Note on the right panel the solid and dotted black error bars corresponding to the bias parameters of the first (LRG) and the second (ELG) tracer respectively in the multi-tracer technique. The vertical dashed black line stands for the fiducial cosmology value.

Chapter 7

Conclusions

This PhD thesis is dedicated to the development of a unified pipeline of large-scale structure data analysis with galaxy number count angular power spectra. The project led to the publication of three articles whose analyses have been presented in chapter 4, chapter 5 and chapter 6. Here, we briefly discuss and highlight the most important results we obtained.

In the work done in chapter 4, we have studied the effect of redshift-space distortions (RSD) on the tomographic angular power spectrum of galaxy number count fluctuations (in the linear regime). In detail, we estimated to what extent the information encoded in the RSD term can affect a cosmological analysis. To this purpose, we have introduced, for the first time to our knowledge, the full expression of the RSD along with the density perturbations in the Limber approximation. We have modified the publicly available `CosmoSIS` code, and we have validated it at given redshift and multipole ranges against the Boltzmann solver code `CLASS`.

In order to study the impact of RSD, we have followed this rationale. First, we construct mock observables in the form of galaxy number count tomographic angular power spectra, $C_\ell^{\rm g}(z_i, z_j)$, including both density fluctuations and RSD. Then, we fit this synthetic data with two theoretical models:

- A model that incorporates exactly the same information as in the mock data set;
- A model that ignores RSD.

For this analysis, we have adopted two planned galaxy surveys, one as a proxy for future photometric missions in the optical/near-infrared waveband, and another as a representative of oncoming spectroscopic experiments at radio frequencies. The former follows the specifications of a *Euclid*-like satellite, whereas for the latter we have considered HI-line galaxy observations as performed by SKA1 (the first phase of the SKA radio telescope). In order to opt between an equi-populated and an equi-spaced redshift binning, we have performed a Fisher matrix test and a preliminary MCMC analysis on the cosmological set $\{\Omega_{\rm m}, h, \sigma_8\}$. After choosing the former as the optimal binning configuration, we have proceeded to a more extensive Bayesian analysis. For the final analysis, we have considered:

i) An ideal scenario, with no nuisance parameter to model the galaxy bias;

ii) A realistic scenario, with an overall normalisation and a redshift dependence to account for a certain ignorance of the bias;

iii) A conservative scenario, where the bias can evolve freely over the redshift range.

Given these cases we can summarise our basic results as:

- The discrepancy on the estimated mean values of cosmological parameters between an analysis with and without RSD is statistically significant for both our proxy surveys, especially for the parameters $\{\Omega_{\rm m}, \sigma_8\}$. This holds true for both the ideal, the realistic and the conservative scenario (see Figure 4.7, Figure 4.9 and Figure 4.11).

- The wrong theoretical model (including only density perturbations) yields very degenerate results on σ_8, since the normalisation of the matter power spectrum and the overall normalisation of the bias are completely degenerate. This happens in a similar fashion when we consider bias nuisance parameters per redshift bin. We partially lift this degeneracy when we add RSD, which are insensitive to the galaxy bias.

- Overall, SKA1 is less informative than *Euclid* due to the lower SNR ascribed to the shorter multipole range and the smaller sky coverage.

These results demonstrate that the inclusion of RSD on top of the density fluctuations in our theoretical predictions is of great importance in order to avoid large biases which dominate the statistics and inevitably lead to selecting erroneous cosmological models. Moreover, given the fact that RSD are insensitive to the galaxy bias, one can yield tighter constraints on the measurements of the amplitude of the density perturbations in the power spectrum σ_8.

Then, in chapter 5 we have aimed to assess the effect of correctly including the weak lensing effect of magnification bias in galaxy number counts in a fully likelihood-based parameter estimation analysis. We have not only investigated standard ΛCDM parameters, as well compelling extensions such as dynamical dark energy and a phenomenological parameterisation to modified gravity. To maximise the impact of magnification—which, being lensing, is an integrated effect—we have focussed the analysis on the specifications of deep radio continuum surveys using the Evolutionary Map of the Universe as a reference, for which we chose both two (very wide) and five (narrower yet broad) redshift bins. Again, we have restricted the harmonic-space angular power spectrum to the Limber approximation and the linear scales, and according to that, applied cuts on the multipole range. Then, we have created mock data including the magnification in the galaxy clustering and fit it with two theory vector constructions: one correctly including magnification bias, and another neglecting lensing.

In addition to that, we introduced a number of scenarios regarding the knowledge we have on the galaxy bias:

1. An idealistic scenario where the galaxy bias is perfectly known;
2. A pessimistic scenario where a free normalisation galaxy bias parameter is introduced at the whole redshift range;
3. A conservative scenario that allows for a nuisance galaxy bias parameter for each bin.

Considering all these cases, we summarise here the most important results obtained with the different cosmological models:

ΛCDM – Here, the results we obtained with both binning configurations (Gaussian and top-hat) are comparable since the bins are always wide enough. In detail, we saw that there are biased estimates for the parameters $\{S_8, h\}$ when the galaxy bias is know exactly and if we neglect the magnification effect. This bias is not seen when we include nuisance parameters, but it is evident that the wrong theoretical model yields unconstrained results on the normalisation of the power spectrum σ_8 which is degenerate with galaxy bias. We lift this bias when we consider the magnification flux which is independent on the galaxy bias. Another point is that when the narrower binning is chosen, the parameters are more constrained due to the better redshift precision on the power spectrum. In addition to that, we appreciate in this case that there is a biased measurement in the conservative case with the incomplete model on S_8 owing to the overestimate of the nuisance galaxy bias parameters. This is also true for the following cosmological models that we examined. The results from now on were obtained adopting the more realistic case for the Gaussian redshift bins.

DE – Regarding the constraints on this CPL Dark Energy model, the biased estimates are not seen when we include the wrong theory vector in the 2-bin case, except the biased result on h in the pessimistic scenario with the 5-bins. Overall, as in the ΛCDM model, there are better constraints with the narrow binning over the wide one, and also degeneracy on S_8 which is alleviated with the magnification flux in the pessimistic and the conservative scenarios. As for the results on $\{w_0, w_a\}$, in the all the cases and the scenarios considered, the estimates with the incomplete model are biased. In the wide binning, the bias is slightly more enhanced since the magnification flux as a lensing effect becomes more important.

MG – When we examine the Modified Gravity model, the results on $\{S_8, h\}$ are similar to those of the CPL, but with the only bias now seen only for the 5-bin conservative case on S_8. There are no biases on any parameter out of the set $\{Q_0, \Sigma_0\}$.

In the final test we considered, we proved that the inclusion of the RSD correction in the galaxy clustering is not important in the case of radio continuum surveys like EMU, since the very poor redshift knowledge leads to the dilution of the effect.

All the above results stress the importance that for the radio continuum surveys, the incorporation of the magnification flux is is necessary on the one hand, to avoid biases on the estimated parameters, and on the other hand, to break the degenerate relation between σ_8 and the galaxy bias. Also these biased estimates tend to increase when very wide bins are considered, a results that demonstrates the fact that the magnification effect becomes more important with time.

Finally in chapter 6 we implemented the multi-tracer technique with a likelihood-based approach for harmonic-space power spectra, and investigated the potential of improving the 2σ bound on the sum of the neutrino masses within a ΛCDM model. For that purpose, we considered the luminous red galaxy (LRG) and the emission-line galaxy (ELG) samples of the Dark Energy Spectroscopic Instrument (DESI). We conducted mock data fitting with the `emcee` sampler, and we included the RSDs correction on the galaxy density fluctuations. Since the contribution of the massive neutrinos introduces a scale dependence on the growth factor and the growth rate of structures, so does on the linear galaxy bias. For that purpose we examined the scale dependence in the galaxy bias as described in Castorina et al., 2014. (and LoVerde, 2016 in section C.1). The modified `CosmoSIS` code including all the adds-on is presented in section D.1.

The produced angular power spectra were Limber approximated and in the linear regime, so we applied multipole scale cuts where the scales under consideration are valid. We did this for the case of four galaxy distributions. The LRG and ELG galaxy sub-samples, their multi-tracing, and their summed DESI distribution with a weighed average galaxy bias. Given that we adopted two realistic scenarios to account for the ignorance on the galaxy bias with the introduction of nuisance parameters that should be marginalised over, namely: i) a nuisance normalisation parameter spanning the whole redshift range; and ii) A conservative case with nuisance parameter per bin.

We can briefly summarise our results as following:

- Implementing the galaxy bias of LoVerde, 2016 we see unnaturally tight constraints on the sum of the neutrino masses and the total matter fraction, rendering the comparison of the constraining power between the different galaxy distributions impossible.

- In the realistic scenario (Castorina et al., 2014) we can appreciate a difference between the cases. The results obtained with the multi-tracing are overall the strongest with an enhancement of 24% on the upper 2σ bound of the sum of neutrino masses with respect to DESI. Also the 1σ errors for the galaxy bias nuisance parameter and for $\sigma 8$ are tighter by 30%.

- Finally the results of the conservative scenario (Castorina et al., 2014) are comparable with those of the realistic one. One difference is the worsening of the upper bound on the sum of the neutrino mass due to the larger parameter set in the likelihood. Still, multi-tracing in this case improves the 2σ upper bound

of the sum of the neutrino masses at 44% better than DESI. Again we see better results on the 1σ error of the nuisance bias parameters and the σ_8 parameter by $\sim 30\%$.

The above results demonstrate that the multi-tracer analysis between at least two different tracers results in the improvement on the cosmological parameters and especially on the 2σ upper bound on the sum of neutrino masses up to 44% compared with the constraints considering a single tracer.

Appendix A

A.1 Derivation of Eq. (10) for RSD

We apply the recurrence relations for the spherical Bessel functions to express $j_\ell''(k\chi)$ in terms of j functions at different multipoles (see e.g. Grasshorn Gebhardt and Jeong, 2018). Thence, we obtain

$$C_{\ell\gg1}^{\mathrm{g,den+RSD}}(z_i,z_j)=\int\frac{\mathrm{d}\chi}{\chi^2}\sum_A K_A^{ij}(\chi)P_{\mathrm{lin}}\left(k=\frac{\ell+A}{\chi}\right), \tag{A.1}$$

where A is an index that can only take values $1/2$, $-3/2$, or $5/2$, and $K_A^{ij}(\chi)$ is the kernel related to the redshift bin pair $i-j$. We have

$$\begin{aligned}K_{1/2}^{ij}(\chi)=&\,a_0W_b^i(\chi)W_b^j(\chi)+a_1W_f^i(\chi)W_f^j(\chi)+a_2W_b^i(\chi)W_f^j(\chi)+a_3W_f^i(\chi)W_b^j(\chi)\\&+a_4W_b^i(\chi)W_f^j\left(\frac{\ell-3/2}{\ell+1/2}\chi\right)+a_5W_b^i(\chi)W_f^j\left(\frac{\ell+5/2}{\ell+1/2}\chi\right)\\&+a_6W_f^i(\chi)W_f^j\left(\frac{\ell-3/2}{\ell+1/2}\chi\right)+a_7W_f^i(\chi)W_f^j\left(\frac{\ell+5/2}{\ell+1/2}\chi\right),\end{aligned} \tag{A.2}$$

where we recognise the first term as that in Equation 4.5; this implies $a_0=1$. Then,

$$\begin{aligned}K_{-3/2}^{ij}(\chi)=&\,a_8W_f^i(\chi)W_b^j\left(\frac{\ell+1/2}{\ell-3/2}\chi\right)+a_9W_f^i(\chi)W_f^j(\chi)\\&+a_{10}W_f^i(\chi)W_f^j\left(\frac{\ell+1/2}{\ell-3/2}\chi\right)+a_{11}W_f^i(\chi)W_f^j\left(\frac{\ell+5/2}{\ell-3/2}\chi\right),\end{aligned} \tag{A.3}$$

and finally,

$$\begin{aligned}K_{5/2}^{ij}(\chi)=&\,a_{12}W_f^i(\chi)W_b^j\left(\frac{\ell+1/2}{\ell+5/2}\chi\right)+a_{13}W_f^i(\chi)W_f^j(\chi)\\&+a_{14}W_f^i(\chi)W_f^j\left(\frac{\ell+1/2}{\ell+5/2}\chi\right)+a_{15}W_f^i(\chi)W_f^j\left(\frac{\ell-3/2}{\ell+5/2}\chi\right),\end{aligned} \tag{A.4}$$

The coefficients a_i are presented in subsection A.1.1. Now, if we perform a change of variable $\tilde{\chi}=[(\ell+A)/(\ell+1/2)]\chi$, Equation A.1 can be further simplified so that

only the usual Limber identity $k = (\ell + 1/2)/\chi$ appears. Thus, we have

$$
\begin{aligned}
C_{\ell\gg1}^{\mathrm{g,den+RSD}}(z_i, z_j) = \int \frac{\mathrm{d}\chi}{\chi^2} P_{\mathrm{lin}}\left(k = \frac{\ell+1/2}{\chi}\right) \Bigg[& \tilde{a}_0 W_b^i(\chi) W_b^j(\chi) + \tilde{a}_1 W_f^i(\chi) W_f^j(\chi) \\
& + \tilde{a}_2 W_b^i(\chi) W_f^j(\chi) + \tilde{a}_3 W_f^i(\chi) W_b^j(\chi) + \tilde{a}_4 W_b^i(\chi) W_f^j\left(\frac{2\ell-3}{2\ell+1}\chi\right) \\
& + \tilde{a}_5 W_b^i(\chi) W_f^j\left(\frac{2\ell+5}{2\ell+1}\chi\right) + \tilde{a}_6 W_f^i(\chi) W_f^j\left(\frac{2\ell-3}{2\ell+1}\chi\right) + \tilde{a}_7 W_f^i(\chi) W_f^j\left(\frac{2\ell+5}{2\ell+1}\chi\right) \\
& + \tilde{a}_8 W_f^i\left(\frac{2\ell-3}{2\ell+1}\chi\right) W_b^j(\chi) + \tilde{a}_9 W_f^i\left(\frac{2\ell-3}{2\ell+1}\chi\right) W_f^j\left(\frac{2\ell-3}{2\ell+1}\chi\right) \\
& + \tilde{a}_{10} W_f^i\left(\frac{2\ell-3}{2\ell+1}\chi\right) W_f^j(\chi) + \tilde{a}_{11} W_f^i\left(\frac{2\ell-3}{2\ell+1}\chi\right) W_f^j\left(\frac{2\ell+5}{2\ell+1}\chi\right) \\
& + \tilde{a}_{12} W_f^i\left(\frac{2\ell+5}{2\ell+1}\chi\right) W_b^j(\chi) + \tilde{a}_{13} W_f^i\left(\frac{2\ell+5}{2\ell+1}\chi\right) W_f^j\left(\frac{2\ell+5}{2\ell+1}\chi\right) \\
& + \tilde{a}_{14} W_f^i\left(\frac{2\ell+5}{2\ell+1}\chi\right) W_f^j(\chi) + \tilde{a}_{15} W_f^i\left(\frac{2\ell+5}{2\ell+1}\chi\right) W_f^j\left(\frac{2\ell-3}{2\ell+1}\chi\right) \Bigg], \qquad \text{(A.5)}
\end{aligned}
$$

where $\{\tilde{a}_0, \ldots, \tilde{a}_7\} = \{a_0, \ldots, a_7\}$, $\{\tilde{a}_8, \ldots, \tilde{a}_{11}\} = (2\ell+1)/(2\ell-3)\{a_8, \ldots, a_{11}\}$, and $\{\tilde{a}_{12}, \ldots, \tilde{a}_{15}\} = (2\ell+1)/(2\ell+5)\{a_{12}, \ldots, a_{15}\}$. Eventually, by defining the global den+RSD window function $W^i(\chi)$ of Equation 4.8, we can recast Equation A.5 in the more compact form of Equation 4.9.

A.1.1

$$a_0 = 1, \tag{A.6}$$

$$a_1 = \left[\frac{2\ell^2 + 2\ell - 1}{(2\ell - 1)(2\ell + 3)}\right]^2, \tag{A.7}$$

$$a_2 = \sqrt{a_1}, \tag{A.8}$$

$$a_3 = a_2, \tag{A.9}$$

$$a_4 = -\frac{\ell(\ell - 1)}{(2\ell - 1)\sqrt{(2\ell + 1)(2\ell - 3)}}, \tag{A.10}$$

$$a_5 = -\frac{(\ell + 1)(\ell + 2)}{(2\ell + 3)\sqrt{(2\ell + 1)(2\ell + 5)}}, \tag{A.11}$$

$$a_6 = a_2 a_4, \tag{A.12}$$

$$a_7 = a_2 a_5, \tag{A.13}$$

$$a_8 = \frac{2\ell - 3}{2\ell + 1} a_4, \tag{A.14}$$

$$a_9 = \left[\frac{\ell(\ell - 1)}{(2\ell - 1)(2\ell + 1)}\right]^2, \tag{A.15}$$

$$a_{10} = a_2 a_8, \tag{A.16}$$

$$a_{11} = \frac{2\ell - 3}{\sqrt{(2\ell + 5)(2\ell - 3)}} \sqrt{a_9 a_{13}}, \tag{A.17}$$

$$a_{12} = \frac{2\ell + 5}{2\ell + 1} a_5, \tag{A.18}$$

$$a_{13} = \left[\frac{(\ell + 1)(\ell + 2)}{(2\ell + 1)(2\ell + 3)}\right]^2, \tag{A.19}$$

$$a_{14} = a_2 a_{12}, \tag{A.20}$$

$$a_{15} = \frac{2\ell + 5}{2\ell + 1} \frac{a_{11} a_4}{a_8} \tag{A.21}$$

Appendix B

B.1 EMU: Top-hat bins

Here, we present in Figure B.1 and Table B.1 the means and their corresponding 1σ confidence levels on the cosmological set $\{S_8, h\}$ in the case of 2 wide and 5 narrower top-hat bins for the ideal, the pessimistic and the conservative scenario.

TABLE B.1: Means and corresponding 68% marginal error intervals on cosmological parameters for the EMU radio continuum galaxy survey applying 2 (5) top-hat bins with the ΛCDM model on the top table (on the bottom table).

2 top-hat bins (ΛCDM)						
	Ideal scenario		Realistic scenario		Conservative scenario	
	den	den+mag	den	den+mag	den	den+mag
S_8	0.9415 ± 0.0560	0.8298 ± 0.0422	0.9960 ± 0.3248	0.8245 ± 0.1185	0.8379 ± 0.2269	0.8031 ± 0.1101
h	0.5244 ± 0.0763	0.6847 ± 0.0915	0.5281 ± 0.07530	0.7008 ± 0.1161	0.6857 ± 0.1296	0.6883 ± 0.1296
5 top-hat bins (ΛCDM)						
	Ideal scenario		Realistic scenario		Conservative scenario	
	den	den+mag	den	den+mag	den	den+mag
S_8	0.8119 ± 0.0205	0.8191 ± 0.0195	0.7996 ± 0.1921	0.8150 ± 0.1216	0.6204 ± 0.1003	0.7570 ± 0.0950
h	0.7191 ± 0.0435	0.6969 ± 0.0419	0.7199 ± 0.0436	0.6976 ± 0.0408	0.7003 ± 0.0547	0.6867 ± 0.0491

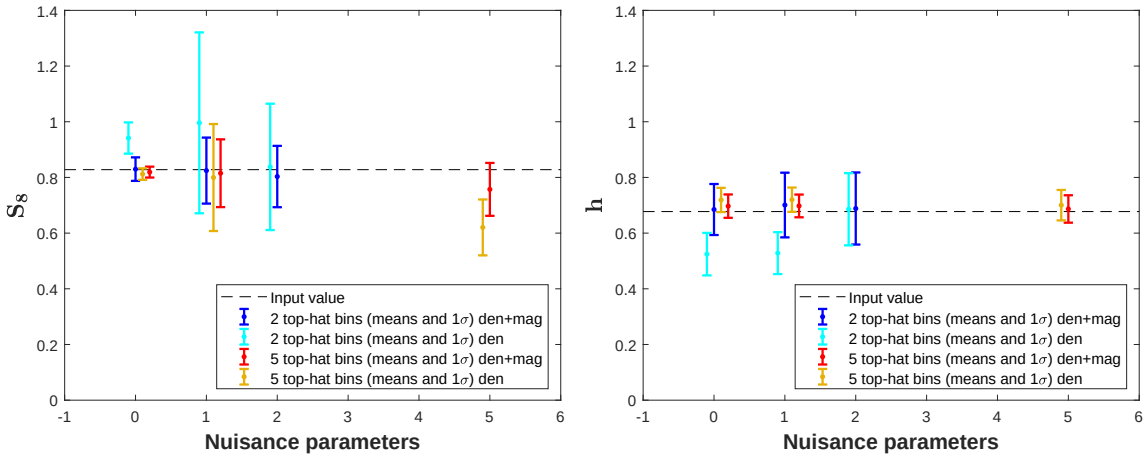

FIGURE B.1: EMU mean and 68% constraints on the derived S_8 (left) and h (right) cosmological parameter in top-hat (top) and Gaussian (bottom) bins as a function of the number of nuisance parameters for the ΛCDM model. Note the different colors accounting for the number of bins and the density w/o magnification spectra fitting

Appendix C

C.1 Scale dependent galaxy bias by (LoVerde, 2016)

This is described by

$$b(k,z) = \begin{cases} b(z) - qf_\nu(b(z)-1) & k \ll k_{\rm fs} \\ b(z) + b(z)f_\nu & k \gg k_{\rm fs} \end{cases} \tag{C.1}$$

where $b(z)$ the usual scale-independent galaxy bias and $q_0 \approx 0.6$.

C.1.1 Results

In Figure C.1 we present the 1σ and 2σ contours on the parameter set $\{\Omega_{\rm m}, h, \sigma_8, \sum m_\nu\}$ for the 4 galaxy samples considering the realistic case and the LoVerde's recipe for the galaxy bias as given by Equation C.1. We mention again that the fiducial values used to generate the mock data and the priors for the Bayesian analysis are shown in Table 6.3 where we always include the RSDs correction on the galaxy density field.

It is clear that the constraints on the parameters are quite stringent and similar for all the galaxy distribution cases with the exception that the multi-tracing and the DESI yield slightly tighter constraints on h and $\Omega_{\rm m}$. Most importantly, it is worth mentioning that the results on the upper bound of the neutrino mass are somewhat unexpected since they seem unnaturally strict. This is a consequence of the relation Equation C.1 which imposes only very small values on the Ω_ν parameter during the `emcee` likelihood evaluation. This, in turn, affects the result on the $\Omega_{\rm m}$ parameter as well, since it includes the massive neutrino contribution, and is therefore not allowed to vary on the parameter space. As a result we are not able to estimate the difference in the constraining power between all the galaxy distribution cases and therefore we do not proceed with the conservative bias case.

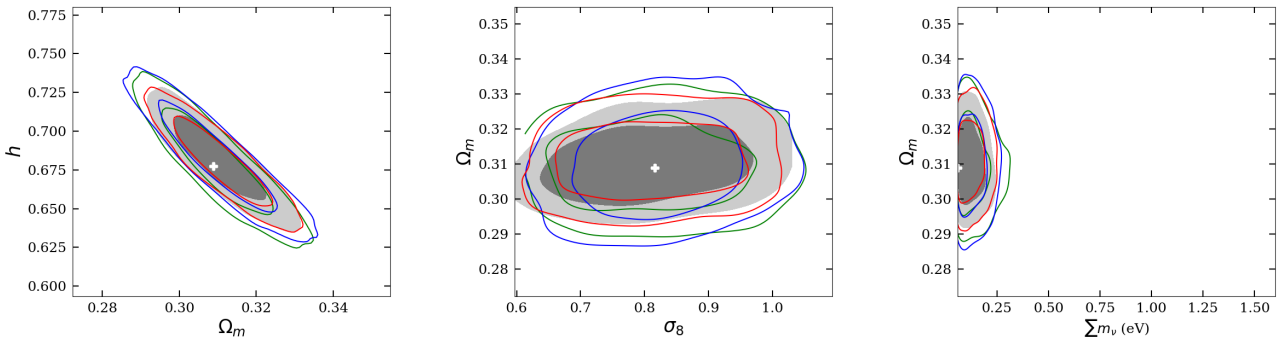

FIGURE C.1: Same as Figure 6.3 but for the galaxy bias given by Equation C.1

TABLE C.1: Same as Table 6.4 but for the galaxy bias given by Equation C.1

	Realistic scenario			
	LRG	ELG	DESI	Multi-tracer
Ω_m	$0.3124^{+0.0061}_{-0.0125}$	$0.3106^{+0.0095}_{-0.0107}$	$0.3113^{+0.0076}_{-0.0091}$	$0.3062^{+0.0106}_{-0.0050}$
h	$0.6708^{+0.0306}_{-0.0153}$	$0.6836^{+0.0213}_{-0.0265}$	$0.6794^{+0.0184}_{-0.0191}$	$0.6706^{+0.0288}_{-0.0073}$
σ_8	$0.8159^{+0.0739}_{-0.1362}$	$0.8147^{+0.0946}_{-0.0832}$	$0.7901^{+0.1191}_{-0.0822}$	$0.7448^{+0.1543}_{-0.0628}$
$\sum m_\nu$ (95%CL)	<0.1831	<0.1366	<0.1426	<0.1040

Appendix D

D.1 The public code

Our public code can be downloaded from the github repository `https://github.com/ktanidis/Modified_CosmoSIS_for_galaxy_number_count_angular_power_spectra`. This is a modified version of the publicly available code `CosmoSIS`. In this version the galaxy number count Limber approximated angular power spectra are calculated in the linear regime allowing for single and multi-tracers and including the density fluctuations, RSDs and magnification bias corrections. Inside the same repository we provide installation instructions in the `README.md` file. Particularly, we describe the required package dependencies and the set-up process. The physical framework of the code is described in section 6.1.

To account for single or multi-tracer analysis, we use the `CosmoSIS` module load_nz. This module reads from a txt file the distributions for the i-th bin of the tracer A with the format: 1st column redshift z, and the rest the $N_i^A(z)$ bins. For example for two tracers A,B each having 2 bins in the redshift z range the columns read : z, tracerA:bin1, tracerA:bin2, tracerB:bin1, tracerB:bin2

The modified part of the code is the `project_2d` module (for the original `CosmoSIS` module version see project_2d), and more specifically:

- `utils.c`: Loads the function $P_{\rm lin}(k_\ell)$, and calculates $D(k_\ell, z)$, $f(k_\ell, z)$, $b(k_\ell, z)$ (based on Equation 6.20)
- `kernel.c`: Specifies the considered galaxy number count contributions under the names `DEN` for the galaxy density field, `RSD` for redshift-space distortions and `MAG` for the weak lensing magnification. It also calculates the corresponding normalized N_i^A and some prefacors (in the case of weak lensing magnification)
- `limber.c`: Calculates the $C^{\rm g}_{\ell\gg1}(z_i^A, z_j^B)$ assuming Equation 6.3.

In addition to these, the python interface of the code is modified as well:

- `limber.py`: loads the source code functions
- `project_2d.py`: provides the output $C^{\rm g}_{\ell\gg1}(z_i^A, z_j^B)$. Three kernels are implemented with the names `W_source`, `F_source` and `M_source` accounting for `DEN`, `RSD` and `MAG` respectively.

NOTE: The current modified `CosmoSIS` version is valid for galaxy clustering ONLY under the entry `galcl-galcl=source-source-source` (see the example ini file provided in the `README.md`). DO NOT attempt to ask output for the section names like `CMB_kappa`, `Shear` or `Intrinsic alignments, etc` (for these see again the original module project_2d).

Finally, we modified the Gaussian likelihood module 2pt to account for the output name `galcl`.

In order to test the code we provide an example ini file (for more details see `README.md` and ini file provided). The pipeline specified there gives the output mock data (data vector and covariance matrix) of multi-tracer galaxy number count angular spectra between the LRG and the ELG samples of the DESI (Aghamousa et al., 2016) given a fiducial cosmological model. The cosmological parameter values are read from another `values.ini` file. There we can also declare whether we will include or not the density fluctuations, the redshift-space distortions and weak lensing magnification contributions by specifying the value 1 or 0 respectively for the parameters `DEN`, `RSD` and `MAG` (default is 1).

Bibliography

Abazajian, Kevork N. et al. (2009). "The Seventh Data Release of the Sloan Digital Sky Survey". In: *Astrophys. J. Suppl.* 182, pp. 543–558. DOI: 10.1088/0067-0049/182/2/543. arXiv: 0812.0649 [astro-ph].

Abbott, T. M. C. et al. (2018a). "Dark Energy Survey year 1 results: Cosmological constraints from galaxy clustering and weak lensing". In: *Phys. Rev.* D98.4, p. 043526. DOI: 10.1103/PhysRevD.98.043526. arXiv: 1708.01530 [astro-ph.CO].

— (2018b). "Dark Energy Survey Year 1 Results: Joint Analysis of Galaxy Clustering, Galaxy Lensing, and CMB Lensing Two-point Functions". In: arXiv: 1810.02322 [astro-ph.CO].

Abdalla, Filipe B. et al. (2015). "Cosmology from HI galaxy surveys with the SKA". In: *ArXiv e-prints* PoS AASKA14, p. 017. arXiv: 1501.04035 [astro-ph.CO].

Addison, G. E. et al. (2016). "Quantifying discordance in the 2015 Planck CMB spectrum". In: *Astrophys. J.* 818.2, p. 132. DOI: 10.3847/0004-637X/818/2/132. arXiv: 1511.00055 [astro-ph.CO].

Ade, P. A. R. et al. (2014). "Planck 2013 results. I. Overview of products and scientific results". In: *Astron. Astrophys.* 571, A1. DOI: 10.1051/0004-6361/201321529. arXiv: 1303.5062 [astro-ph.CO].

— (2015). "Joint Analysis of BICEP2/Keck Array and Planck Data". In: *Phys. Rev. Lett.* 114, p. 101301. DOI: 10.1103/PhysRevLett.114.101301. arXiv: 1502.00612 [astro-ph.CO].

— (2016). "Planck 2015 results. XIII. Cosmological parameters". In: *Astron. Astrophys.* 594, A13. DOI: 10.1051/0004-6361/201525830. arXiv: 1502.01589 [astro-ph.CO].

Afshordi, Niayesh and Andrew J. Tolley (2008). "Primordial non-Gaussianity, statistics of collapsed objects, and the integrated Sachs-Wolfe effect". In: *Phys. Rev. D* 78 (12), p. 123507. DOI: 10.1103/PhysRevD.78.123507. URL: https://link.aps.org/doi/10.1103/PhysRevD.78.123507.

Aghamousa, Amir et al. (2016). "The DESI Experiment Part I: Science,Targeting, and Survey Design". In: *ArXiv e-prints*. arXiv: 1611.00036 [astro-ph.IM].

Aghanim, N. et al. (2020). "Planck 2018 results". In: *Astronomy & Astrophysics* 641, A6. ISSN: 1432-0746. DOI: 10.1051/0004-6361/201833910. URL: http://dx.doi.org/10.1051/0004-6361/201833910.

Amendola, Luca, Martin Kunz, and Domenico Sapone (2008). "Measuring the dark side (with weak lensing)". In: *JCAP* 0804, p. 013. DOI: 10.1088/1475-7516/2008/04/013. arXiv: 0704.2421 [astro-ph].

Amendola, Luca et al. (2013). "Cosmology and fundamental physics with the Euclid satellite". In: *Living Rev. Rel.* 16, p. 6. DOI: 10.12942/lrr-2013-6. arXiv: 1206.1225 [astro-ph.CO].

— (2018). "Cosmology and fundamental physics with the Euclid satellite". In: *Living Rev. Rel.* 21.1, p. 2. DOI: 10.1007/s41114-017-0010-3. arXiv: 1606.00180 [astro-ph.CO].

Bacon, David J. et al. (2018). "Cosmology with Phase 1 of the Square Kilometre Array: Red Book 2018: Technical specifications and performance forecasts". In: *ArXiv e-prints* Submitted to: Publ. Astron. Soc. Austral. arXiv: 1811.02743 [astro-ph.CO].

Balaguera-Antolínez, A. et al. (2018). "Extracting cosmological information from the angular power spectrum of the 2MASS Photometric Redshift catalogue". In: *Mon. Not. Roy. Astron. Soc.* 476.1, pp. 1050–1070. DOI: 10.1093/mnras/sty262. arXiv: 1711.04583 [astro-ph.CO].

Ballardini, M. et al. (2018). "Probing primordial features with next-generation photometric and radio surveys". In: *Journal of Cosmology and Astroparticle Physics* 2018.04, pp. 044–044. DOI: 10.1088/1475-7516/2018/04/044. URL: https://doi.org/10.1088%2F1475-7516%2F2018%2F04%2F044.

Bartelmann, M. and P. Schneider (Jan. 2001). "Weak gravitational lensing". In: *physrep* 340, pp. 291–472. DOI: 10.1016/S0370-1573(00)00082-X. eprint: astro-ph/9912508.

Bartelmann, Matthias and Peter Schneider (2001). "Weak gravitational lensing". In: *Physics Reports* 340.4, pp. 291 –472. ISSN: 0370-1573. DOI: https://doi.org/10.1016/S0370-1573(00)00082-X. URL: http://www.sciencedirect.com/science/article/pii/S037015730000082X.

Battye, Richard A., Tom Charnock, and Adam Moss (2015). "Tension between the power spectrum of density perturbations measured on large and small scales". In: *Phys. Rev.* D91.10, p. 103508. DOI: 10.1103/PhysRevD.91.103508. arXiv: 1409.2769 [astro-ph.CO].

Bennett, C. L. et al. (2003). "First-Year Wilkinson Microwave Anisotropy Probe (WMAP) Observations: Preliminary Maps and Basic Results". In: *The Astrophysical Journal Supplement Series* 148.1, pp. 1–27. DOI: 10.1086/377253. URL: https://doi.org/10.10862F377253.

Benoist, C. et al. (1996). "Biasing in the Galaxy Distribution". In: *The Astrophysical Journal* 472.2, pp. 452–459. DOI: 10.1086/178078. URL: https://doi.org/10.1086%2F178078.

Bernal, José Luis et al. (2019). "Probing LambdaCDM cosmology with the Evolutionary Map of the Universe survey". In: *Journal of Cosmology and Astroparticle Physics* 2019.02, pp. 030–030. DOI: 10.1088/1475-7516/2019/02/030. URL: https://doi.org/10.1088%2F1475-7516%2F2019%2F02%2F030.

Bernstein, Gary M. (2009). "Comprehensive Two-Point Analyses of Weak Gravitational Lensing Surveys". In: *Astrophys. J.* 695, pp. 652–665. DOI: 10.1088/0004-637X/695/1/652. arXiv: 0808.3400 [astro-ph].

Bernstein, Gary M. and Yan-Chuan Cai (Sept. 2011). "Cosmology without cosmic variance". In: *Monthly Notices of the Royal Astronomical Society* 416.4, pp. 3009–3016. ISSN: 0035-8711. DOI: 10.1111/j.1365-2966.2011.19249.x. eprint: https://academic.oup.com/mnras/article-pdf/416/4/3009/2984860/mnras0416-3009.pdf. URL: https://doi.org/10.1111/j.1365-2966.2011.19249.x.

Bertacca, Daniele et al. (2011). "CMB-galaxy correlation in Unified Dark Matter scalar field cosmologies". In: *Journal of Cosmology and Astroparticle Physics* 2011.03, pp. 039–039. DOI: 10.1088/1475-7516/2011/03/039. URL: https://doi.org/10.1088%2F1475-7516%2F2011%2F03%2F039.

Betoule, M. et al. (2014). "Improved cosmological constraints from a joint analysis of the SDSS-II and SNLS supernova samples". In: *A&A* 568, A22. DOI: 10.1051/0004-6361/201423413. URL: https://doi.org/10.1051/0004-6361/201423413.

Blake, Chris et al. (Jan. 2007). "Cosmological baryonic and matter densities from 600 000 SDSS luminous red galaxies with photometric redshifts". In: *Monthly Notices of the Royal Astronomical Society* 374.4, pp. 1527–1548. ISSN: 0035-8711. DOI: 10.1111/j.1365-2966.2006.11263.x. eprint: http://oup.prod.sis.lan/mnras/article-pdf/374/4/1527/2876307/mnras0374-1527.pdf. URL: https://dx.doi.org/10.1111/j.1365-2966.2006.11263.x.

Blas, Diego, Julien Lesgourgues, and Thomas Tram (2011). "The Cosmic Linear Anisotropy Solving System (CLASS) II: Approximation schemes". In: *JCAP* 1107, p. 034. DOI: 10.1088/1475-7516/2011/07/034. arXiv: 1104.2933 [astro-ph.CO].

Blennow, Mattias (2014). "On the Bayesian approach to neutrino mass ordering". In: *Journal of High Energy Physics* 2014.1. ISSN: 1029-8479. DOI: 10.1007/jhep01(2014)139. URL: http://dx.doi.org/10.1007/JHEP01(2014)139.

Bonvin, Camille and Ruth Durrer (2011). "What galaxy surveys really measure". In: *Phys. Rev.* D84, p. 063505. DOI: 10.1103/PhysRevD.84.063505. arXiv: 1105.5280 [astro-ph.CO].

Boughn, S and Robert Crittenden (Feb. 2004). "A correlation between the cosmic microwave background and large-scale structure in the Universe". In: *Nature* 427, pp. 45–7. DOI: 10.1038/nature02139.

Boughn, S. P. and R. G. Crittenden (2001). "Cross Correlation of the Cosmic Microwave Background with Radio Sources: Constraints on an Accelerating Universe". In: *Phys. Rev. Lett.* 88 (2), p. 021302. DOI: 10.1103/PhysRevLett.88.021302. URL: https://link.aps.org/doi/10.1103/PhysRevLett.88.021302.

Cacciato, Marcello et al. (2013). "Cosmological Constraints from a Combination of Galaxy Clustering and Lensing – III. Application to SDSS Data". In: *Mon. Not. Roy. Astron. Soc.* 430, p. 767. DOI: 10.1093/mnras/sts525. arXiv: 1207.0503 [astro-ph.CO].

Camera, S., C. Fedeli, and L. Moscardini (2014). "Magnification bias as a novel probe for primordial magnetic fields". In: *IOP Publishing* 2014.03, pp. 027–027. DOI: 10.1088/1475-7516/2014/03/027. URL: https://doi.org/10.1088%2F1475-7516%2F2014%2F03%2F027.

Camera, Stefano, Roy Maartens, and Mario G. Santos (2015a). "Einstein's legacy in galaxy surveys". In: *Mon. Not. Roy. Astron. Soc.* 451.1, pp. L80–L84. DOI: 10.1093/mnrasl/slv069. arXiv: 1412.4781 [astro-ph.CO].

— (2015b). "Einstein's legacy in galaxy surveys". In: *Mon. Not. Roy. Astron. Soc.* 451, p. L80. DOI: 10.1093/mnrasl/slv069. arXiv: 1412.4781 [astro-ph.CO].

Camera, Stefano, Matteo Martinelli, and Daniele Bertacca (2019). "Does quartessence ease cosmic tensions?" In: *Phys. Dark Univ.* 23, p. 100247. DOI: 10.1016/j.dark.2018.11.008. arXiv: 1704.06277 [astro-ph.CO].

Camera, Stefano, Mario G. Santos, and Roy Maartens (2015a). "Probing primordial non-Gaussianity with SKA galaxy redshift surveys: a fully relativistic analysis". In: *Mon. Not. Roy. Astron. Soc.* 448.2. [Erratum: Mon. Not. Roy. Astron. Soc.467,no.2,1505(2017)], pp. 1035–1043. DOI: 10.1093/mnras/stv040,10.1093/mnras/stx159. arXiv: 1409.8286 [astro-ph.CO].

Camera, Stefano, Mário G. Santos, and Roy Maartens (Feb. 2015b). "Probing primordial non-Gaussianity with SKA galaxy redshift surveys: a fully relativistic analysis". In: *Monthly Notices of the Royal Astronomical Society* 448.2, pp. 1035–1043. ISSN: 0035-8711. DOI: 10.1093/mnras/stv040. eprint: http://oup.prod.sis.lan/mnras/article-pdf/448/2/1035/3587443/stv040.pdf. URL: https://doi.org/10.1093/mnras/stv040.

Camera, Stefano et al. (Dec. 2012). "Impact of redshift information on cosmological applications with next-generation radio surveys". In: *Monthly Notices of the Royal Astronomical Society* 427.3, pp. 2079–2088. ISSN: 0035-8711. DOI: 10.1111/j.1365-2966.2012.22073.x. eprint: http://oup.prod.sis.lan/mnras/article-pdf/427/3/2079/3833350/427-3-2079.pdf. URL: https://doi.org/10.1111/j.1365-2966.2012.22073.x.

Camera, Stefano et al. (2017). "SKA weak lensing – III. Added value of multiwavelength synergies for the mitigation of systematics". In: *Mon. Not. Roy. Astron. Soc.* 464.4, pp. 4747–4760. DOI: 10.1093/mnras/stw2688. arXiv: 1606.03451 [astro-ph.CO].

Camera, Stefano et al. (2018). "Optimized angular power spectra for spectroscopic galaxy surveys". In: *Mon. Not. Roy. Astron. Soc.* 481.1, pp. 1251–1261. DOI: 10.1093/mnras/sty2284. arXiv: 1803.10773 [astro-ph.CO].

Campagne, J.-E., Neveu, J., and Plaszczynski, S. (2017). "Angpow: a software for the fast computation of accurate tomographic power spectra". In: *A&A* 602, A72. DOI: 10.1051/0004-6361/201730399. URL: https://doi.org/10.1051/0004-6361/201730399.

Capozzi, F. et al. (2016). "Neutrino masses and mixings: Status of known and unknown 3 parameters". In: *Nuclear Physics B* 908. Neutrino Oscillations: Celebrating the Nobel Prize in Physics 2015, pp. 218 –234. ISSN: 0550-3213. DOI: https://doi.org/10.1016/j.nuclphysb.2016.02.016. URL: http://www.sciencedirect.com/science/article/pii/S0550321316000602.

Capozzi, Francesco et al. (2017). "Global constraints on absolute neutrino masses and their ordering". In: *Phys. Rev. D* 95 (9), p. 096014. DOI: 10.1103/PhysRevD.95.096014. URL: https://link.aps.org/doi/10.1103/PhysRevD.95.096014.

Castorina, Emanuele et al. (2014). "Cosmology with massive neutrinos II: on the universality of the halo mass function and bias". In: *Journal of Cosmology and Astroparticle Physics* 2014.02, pp. 049–049. DOI: 10.1088/1475-7516/2014/02/049. URL: https://doi.org/10.1088%2F1475-7516%2F2014%2F02%2F049.

Challinor, Anthony and Antony Lewis (2011a). "Linear power spectrum of observed source number counts". In: *Phys. Rev. D* 84 (4), p. 043516. DOI: 10.1103/PhysRevD.84.043516. URL: https://link.aps.org/doi/10.1103/PhysRevD.84.043516.

— (2011b). "The linear power spectrum of observed source number counts". In: *Phys. Rev.* D84, p. 043516. DOI: 10.1103/PhysRevD.84.043516. arXiv: 1105.5292 [astro-ph.CO].

Charnock, Tom, Richard A. Battye, and Adam Moss (2017). "Planck data versus large scale structure". In: *Phys. Rev.* D95.12, p. 123535. DOI: 10.1103/PhysRevD.95.123535. arXiv: 1703.05959 [astro-ph.CO].

Chaves-Montero, Jonás, Carlos Hernández-Monteagudo, and Raúl E Angulo (Apr. 2018). "The effect of photometric redshift uncertainties on galaxy clustering and baryonic acoustic oscillations". In: *Monthly Notices of the Royal Astronomical Society* 477.3, pp. 3892–3909. ISSN: 0035-8711. DOI: 10.1093/mnras/sty924. eprint: http://oup.prod.sis.lan/mnras/article-pdf/477/3/3892/24812692/sty924.pdf. URL: https://dx.doi.org/10.1093/mnras/sty924.

Chevallier and Polarski (2001). "ACCELERATING UNIVERSES WITH SCALING DARK MATTER". In: *International Journal of Modern Physics D* 10.02, pp. 213–223. DOI: 10.1142/S0218271801000822. eprint: https://doi.org/10.1142/S0218271801000822. URL: https://doi.org/10.1142/S0218271801000822.

Chisari, Nora Elisa et al. (2019). "Core Cosmology Library: Precision Cosmological Predictions for LSST". In: *The Astrophysical Journal Supplement Series* 242.1, p. 2. DOI: 10.3847/1538-4365/ab1658. URL: https://doi.org/10.3847%2F1538-4365%2Fab1658.

Clarkson, Chris (2016). "Roulettes: A weak lensing formalism for strong lensing - II. Derivation and analysis". In: *Class. Quant. Grav.* 33.24, p. 245003. DOI: 10.1088/0264-9381/33/24/245003. arXiv: 1603.04652 [gr-qc].

Clifton, Timothy et al. (2012). "Modified Gravity and Cosmology". In: *Phys. Rept.* 513, pp. 1–189. DOI: 10.1016/j.physrep.2012.01.001. arXiv: 1106.2476 [astro-ph.CO].

Condon, J. J. et al. (1998). "The NRAO VLA Sky Survey". In: *The Astronomical Journal* 115.5, pp. 1693–1716. DOI: 10.1086/300337. URL: https://doi.org/10.1086%2F300337.

Crocce, Martín, Anna Cabré, and Enrique Gaztañaga (June 2011). "Modelling the angular correlation function and its full covariance in photometric galaxy surveys".

In: *Monthly Notices of the Royal Astronomical Society* 414.1, pp. 329–349. ISSN: 0035-8711. DOI: 10.1111/j.1365-2966.2011.18393.x. eprint: http://oup.prod.sis.lan/mnras/article-pdf/414/1/329/3808822/mnras0414-0329.pdf. URL: https://dx.doi.org/10.1111/j.1365-2966.2011.18393.x.

Debono, Ivan and George F. Smoot (2016). "General Relativity and Cosmology: Unsolved Questions and Future Directions". In: *Universe* 2.4, p. 23. DOI: 10.3390/universe2040023. arXiv: 1609.09781 [gr-qc].

Di Dio, Enea et al. (2013). "The CLASSgal code for Relativistic Cosmological Large Scale Structure". In: *JCAP* 1311, p. 044. DOI: 10.1088/1475-7516/2013/11/044. arXiv: 1307.1459 [astro-ph.CO].

Dossett, Jason N. et al. (2015). "Constraints and tensions in testing general relativity from Planck and CFHTLenS data including intrinsic alignment systematics". In: *Phys. Rev. D* 92 (2), p. 023003. DOI: 10.1103/PhysRevD.92.023003. URL: https://link.aps.org/doi/10.1103/PhysRevD.92.023003.

Duncan, Christopher A. J. et al. (Nov. 2013). "On the complementarity of galaxy clustering with cosmic shear and flux magnification". In: *Monthly Notices of the Royal Astronomical Society* 437.3, pp. 2471–2487. ISSN: 0035-8711. DOI: 10.1093/mnras/stt2060. eprint: http://oup.prod.sis.lan/mnras/article-pdf/437/3/2471/18462359/stt2060.pdf. URL: https://doi.org/10.1093/mnras/stt2060.

Durrer, Ruth (2008). *The Cosmic Microwave Background*. Cambridge University Press. DOI: 10.1017/CBO9780511817205.

— (2015). "The cosmic microwave background: the history of its experimental investigation and its significance for cosmology". In: *Class. Quant. Grav.* 32.12, p. 124007. DOI: 10.1088/0264-9381/32/12/124007. arXiv: 1506.01907 [astro-ph.CO].

Eifler, Tim et al. (2014). "Combining Probes of Large-Scale Structure with CosmoLike". In: *Mon. Not. Roy. Astron. Soc.* 440.2, pp. 1379–1390. DOI: 10.1093/mnras/stu251. arXiv: 1302.2401 [astro-ph.CO].

Eisenstein, Daniel J. and Wayne Hu (1998). "Baryonic Features in the Matter Transfer Function". In: 496.2, pp. 605–614. DOI: 10.1086/305424. URL: https://doi.org/10.10862F305424.

Eisenstein, Daniel J. et al. (2005). "Detection of the Baryon Acoustic Peak in the Large-Scale Correlation Function of SDSS Luminous Red Galaxies". In: *The Astrophysical Journal* 633.2, pp. 560–574. DOI: 10.1086/466512. URL: https://doi.org/10.1086%2F466512.

Elvin-Poole, J. et al. (2018). "Dark Energy Survey year 1 results: Galaxy clustering for combined probes". In: *Phys. Rev.* D98.4, p. 042006. DOI: 10.1103/PhysRevD.98.042006. arXiv: 1708.01536 [astro-ph.CO].

Esteban, Ivan et al. (2017). "Updated fit to three neutrino mixing: exploring the accelerator-reactor complementarity". In: *Journal of High Energy Physics* 2017.1. ISSN: 1029-8479. DOI: 10.1007/jhep01(2017)087. URL: http://dx.doi.org/10.1007/JHEP01(2017)087.

February, Sean et al. (2010). "Rendering Dark Energy Void". In: *Mon. Not. Roy. Astron. Soc.* 405, p. 2231. DOI: 10.1111/j.1365-2966.2010.16627.x. arXiv: 0909.1479 [astro-ph.CO].

Feroz, F., M. P. Hobson, and M. Bridges (2009). "MultiNest: an efficient and robust Bayesian inference tool for cosmology and particle physics". In: *Mon. Not. Roy. Astron. Soc.* 398, pp. 1601–1614. DOI: 10.1111/j.1365-2966.2009.14548.x. arXiv: 0809.3437 [astro-ph].

Ferramacho, L. D. et al. (June 2014). "Radio galaxy populations and the multitracer technique: pushing the limits on primordial non-Gaussianity". In: *Monthly Notices of the Royal Astronomical Society* 442.3, pp. 2511–2518. ISSN: 0035-8711. DOI: 10.1093/mnras/stu1015. eprint: http://oup.prod.sis.lan/mnras/article-pdf/442/3/2511/3500067/stu1015.pdf. URL: https://doi.org/10.1093/mnras/stu1015.

Fonseca, José et al. (2015). "Hunting down horizon-scale effects with multi-wavelength surveys". In: *Astrophys. J.* 812.2, p. L22. DOI: 10.1088/2041-8205/812/2/L22. arXiv: 1507.04605 [astro-ph.CO].

Font-Ribera, Andreu et al. (2014). "DESI and other Dark Energy experiments in the era of neutrino mass measurements". In: *Journal of Cosmology and Astroparticle Physics* 2014.05, pp. 023–023. DOI: 10.1088/1475-7516/2014/05/023. URL: https://doi.org/10.1088%2F1475-7516%2F2014%2F05%2F023.

Foreman-Mackey, Daniel et al. (2013). "emcee: The MCMC Hammer". In: *Publ. Astron. Soc. Pac.* 125, pp. 306–312. DOI: 10.1086/670067. arXiv: 1202.3665 [astro-ph.IM].

Gerbino, Martina et al. (2017). "A novel approach to quantifying the sensitivity of current and future cosmological datasets to the neutrino mass ordering through Bayesian hierarchical modeling". In: *Physics Letters B* 775, 239–250. ISSN: 0370-2693. DOI: 10.1016/j.physletb.2017.10.052. URL: http://dx.doi.org/10.1016/j.physletb.2017.10.052.

Giannantonio, Tommaso et al. (2014). "Improved primordial non-Gaussianity constraints from measurements of galaxy clustering and the integrated Sachs-Wolfe effect". In: *Phys. Rev. D* 89 (2), p. 023511. DOI: 10.1103/PhysRevD.89.023511. URL: https://link.aps.org/doi/10.1103/PhysRevD.89.023511.

Gonzalez-Garcia, M.C., Michele Maltoni, and Thomas Schwetz (2016). "Global analyses of neutrino oscillation experiments". In: *Nuclear Physics B* 908. Neutrino Oscillations: Celebrating the Nobel Prize in Physics 2015, pp. 199 –217. ISSN: 0550-3213. DOI: https://doi.org/10.1016/j.nuclphysb.2016.02.033. URL: http://www.sciencedirect.com/science/article/pii/S0550321316000778.

Grasshorn Gebhardt, Henry S. and Donghui Jeong (2018). "Fast and accurate computation of projected two-point functions". In: *Phys. Rev.* D97.2, p. 023504. DOI: 10.1103/PhysRevD.97.023504. arXiv: 1709.02401 [astro-ph.CO].

Guzzo, L. et al. (2008). "A test of the nature of cosmic acceleration using galaxy redshift distortions". In: *Nature* 451.7178, 541–544. ISSN: 1476-4687. DOI: 10.1038/nature06555. URL: http://dx.doi.org/10.1038/nature06555.

Guzzo, Luigi et al. (1997). "Redshift-Space Distortions and the Real-Space Clustering of Different Galaxy Types". In: *The Astrophysical Journal* 489.1, pp. 37–48. DOI: 10.1086/304788. URL: https://doi.org/10.1086%2F304788.

Hannestad, Steen and Thomas Schwetz (2016). "Cosmology and the neutrino mass ordering". In: *Journal of Cosmology and Astroparticle Physics* 2016.11, 035–035. ISSN: 1475-7516. DOI: 10.1088/1475-7516/2016/11/035. URL: http://dx.doi.org/10.1088/1475-7516/2016/11/035.

Harrison, Ian, Michelle Lochner, and Michael L. Brown (2017). "Redshifts for galaxies in radio continuum surveys from Bayesian model fitting of HI 21-cm lines". In: *ArXiv e-prints* submitted to: MNRAS. arXiv: 1704.08278 [astro-ph.CO].

Heavens, A. F. and A. N. Taylor (July 1995). "A spherical harmonic analysis of redshift space". In: *Monthly Notices of the Royal Astronomical Society* 275.2, pp. 483–497. ISSN: 0035-8711. DOI: 10.1093/mnras/275.2.483. eprint: http://oup.prod.sis.lan/mnras/article-pdf/275/2/483/9415535/mnras275-0483.pdf. URL: https://dx.doi.org/10.1093/mnras/275.2.483.

Hildebrandt, H., van Waerbeke, L., and Erben, T. (2009). "CARS: The CFHTLS-Archive-Research Survey* - III. First detection of cosmic magnification in samples of normal high-z galaxies". In: *A&A* 507.2, pp. 683–691. DOI: 10.1051/0004-6361/200912655. URL: https://doi.org/10.1051/0004-6361/200912655.

Hinshaw, G. et al. (Dec. 2012). "Nine-Year Wilkinson Microwave Anisotropy Probe (WMAP) Observations: Cosmological Parameter Results". In: *The Astrophysical Journal Supplement Series* 208. DOI: 10.1088/0067-0049/208/2/19.

Ho, Shirley et al. (2008). "Correlation of CMB with large-scale structure. I. Integrated Sachs-Wolfe tomography and cosmological implications". In: *Phys. Rev. D* 78 (4), p. 043519. DOI: 10.1103/PhysRevD.78.043519. URL: https://link.aps.org/doi/10.1103/PhysRevD.78.043519.

Hoyle, B. et al. (2018). "Dark Energy Survey Year 1 Results: Redshift distributions of the weak lensing source galaxies". In: *Mon. Not. Roy. Astron. Soc.* 478.1, pp. 592–610. DOI: 10.1093/mnras/sty957. arXiv: 1708.01532 [astro-ph.CO].

Hu, Wayne, Daniel J. Eisenstein, and Max Tegmark (1998). "Weighing Neutrinos with Galaxy Surveys". In: *Phys. Rev. Lett.* 80 (24), pp. 5255–5258. DOI: 10.1103/PhysRevLett.80.5255. URL: https://link.aps.org/doi/10.1103/PhysRevLett.80.5255.

Jackson, J.C. (1972). "Fingers of God: A critique of Rees' theory of primordial gravitational radiation". In: *Mon. Not. Roy. Astron. Soc.* 156, 1P–5P. DOI: 10.1093/mnras/156.1.1P. arXiv: 0810.3908 [astro-ph].

Jalilvand, Mona et al. (2019). "Non-linear contributions to angular power spectra". In: *ArXiv e-prints*. arXiv: 1907.13109 [astro-ph.CO].

Jarvis, Matt et al. (2015). "Cosmology with SKA Radio Continuum Surveys". In: *PoS* AASKA14, p. 018. DOI: 10.22323/1.215.0018.

Jelic-Cizmek, Goran et al. (2020). *On the importance of lensing for galaxy clustering in photometric and spectroscopic surveys*. arXiv: 2004.12981 [astro-ph.CO].

Joachimi, B. and S. L. Bridle (2010). "Simultaneous measurement of cosmology and intrinsic alignments using joint cosmic shear and galaxy number density correlations". In: *Astron. Astrophys.* 523, A1. DOI: 10.1051/0004-6361/200913657. arXiv: 0911.2454 [astro-ph.CO].

Johnston, S. et al. (2007). "Science with the Australian Square Kilometre Array Pathfinder". In: *Publications of the Astronomical Society of Australia* 24.4, 174–188. DOI: 10.1071/AS07033.

Johnston, S. et al. (2008). "Science with ASKAP". In: *Experimental Astronomy* 22.3, pp. 151–273. ISSN: 1572-9508. DOI: 10.1007/s10686-008-9124-7. URL: https://doi.org/10.1007/s10686-008-9124-7.

Joudaki, Shahab et al. (2017a). "CFHTLenS revisited: assessing concordance with Planck including astrophysical systematics". In: *Mon. Not. Roy. Astron. Soc.* 465.2, pp. 2033–2052. DOI: 10.1093/mnras/stw2665. arXiv: 1601.05786 [astro-ph.CO].

— (2017b). "KiDS-450: Testing extensions to the standard cosmological model". In: *Mon. Not. Roy. Astron. Soc.* 471.2, pp. 1259–1279. DOI: 10.1093/mnras/stx998. arXiv: 1610.04606 [astro-ph.CO].

Kaiser, N. (Apr. 1992). "Weak gravitational lensing of distant galaxies". In: *apj* 388, pp. 272–286. DOI: 10.1086/171151.

Kaiser, Nick (July 1987a). "Clustering in real space and in redshift space". In: *Monthly Notices of the Royal Astronomical Society* 227.1, pp. 1–21. ISSN: 0035-8711. DOI: 10.1093/mnras/227.1.1. eprint: http://oup.prod.sis.lan/mnras/article-pdf/227/1/1/18522208/mnras227-0001.pdf. URL: https://dx.doi.org/10.1093/mnras/227.1.1.

— (July 1987b). "Clustering in real space and in redshift space". In: *Monthly Notices of the Royal Astronomical Society* 227.1, pp. 1–21. ISSN: 0035-8711. DOI: 10.1093/mnras/227.1.1. eprint: http://oup.prod.sis.lan/mnras/article-pdf/227/1/1/18522208/mnras227-0001.pdf. URL: https://dx.doi.org/10.1093/mnras/227.1.1.

— (Mar. 1992). "Weak gravitational lensing of distant galaxies". In: *The Astrophysical Journal* 388, pp. 272–286. DOI: 10.1086/171151.

Karagiannis, Dionysios et al. (Apr. 2018). "Constraining primordial non-Gaussianity with bispectrum and power spectrum from upcoming optical and radio surveys". In: *Monthly Notices of the Royal Astronomical Society* 478.1, pp. 1341–1376. ISSN: 0035-8711. DOI: 10.1093/mnras/sty1029. eprint: http://oup.prod.sis.lan/mnras/article-pdf/478/1/1341/25027360/sty1029.pdf. URL: https://doi.org/10.1093/mnras/sty1029.

Kim, A. 2004 (2004). "LBNL Report LBNL-56164 ". In:

Kitching, T. D. and A. F. Heavens (2011). "3D Photometric Cosmic Shear". In: *Mon. Not. Roy. Astron. Soc.* 413, p. 2923. DOI: 10.1111/j.1365-2966.2011.18369.x. arXiv: 1007.2953 [astro-ph.CO].

Krause, Elisabeth and Tim Eifler (2017). "cosmolike – cosmological likelihood analyses for photometric galaxy surveys". In: *Mon. Not. Roy. Astron. Soc.* 470.2, pp. 2100–2112. DOI: 10.1093/mnras/stx1261. arXiv: 1601.05779 [astro-ph.CO].

Kwan, J. et al. (2017). "Cosmology from large-scale galaxy clustering and galaxy–galaxy lensing with Dark Energy Survey Science Verification data". In: *Mon. Not. Roy. Astron. Soc.* 464.4, pp. 4045–4062. DOI: 10.1093/mnras/stw2464. arXiv: 1604.07871 [astro-ph.CO].

Laureijs, R. et al. (2011). "Euclid Definition Study Report". In: ESA/SRE, 12. arXiv: 1110.3193 [astro-ph.CO].

Laurent, Pierre et al. (2016). "A 14 h^{-3} Gpc^3 study of cosmic homogeneity using BOSS DR12 quasar sample". In: *JCAP* 11, p. 060. DOI: 10.1088/1475-7516/2016/11/060. arXiv: 1602.09010 [astro-ph.CO].

Lesgourgues, Julien (2011). "The Cosmic Linear Anisotropy Solving System (CLASS) I: Overview". In: CERN-PH-TH/2011-081, LAPTH-009/11. arXiv: 1104.2932 [astro-ph.IM].

Lesgourgues, Julien and Sergio Pastor (2006). "Massive neutrinos and cosmology". In: *Physics Reports* 429.6, pp. 307 –379. ISSN: 0370-1573. DOI: https://doi.org/10.1016/j.physrep.2006.04.001. URL: http://www.sciencedirect.com/science/article/pii/S0370157306001359.

Lewis, Antony, Anthony Challinor, and Anthony Lasenby (2000). "Efficient computation of CMB anisotropies in closed FRW models". In: *Astrophys. J.* 538, pp. 473–476. DOI: 10.1086/309179. arXiv: astro-ph/9911177 [astro-ph].

Liddle, Andrew R. (Jan. 1999). "An Introduction to cosmological inflation". In: pp. 260–295. arXiv: astro-ph/9901124.

Limber, D. N. (Jan. 1953). "The Analysis of Counts of the Extragalactic Nebulae in Terms of a Fluctuating Density Field." In: *apj* 117, p. 134. DOI: 10.1086/145672.

Linder, Eric V. (2003). "Exploring the Expansion History of the Universe". In: *Phys. Rev. Lett.* 90 (9), p. 091301. DOI: 10.1103/PhysRevLett.90.091301. URL: https://link.aps.org/doi/10.1103/PhysRevLett.90.091301.

— (2008). "Redshift distortions as a probe of gravity". In: *Astroparticle Physics* 29.5, pp. 336 –339. ISSN: 0927-6505. DOI: https://doi.org/10.1016/j.astropartphys.2008.03.002. URL: http://www.sciencedirect.com/science/article/pii/S0927650508000418.

Liu, Jia, Alvaro Ortiz-Vazquez, and J. Colin Hill (2016). "Constraining Multiplicative Bias in CFHTLenS Weak Lensing Shear Data". In: *Phys. Rev.* D93.10, p. 103508. DOI: 10.1103/PhysRevD.93.103508. arXiv: 1601.05720 [astro-ph.CO].

Long, Andrew J. et al. (2018). "Neutrino mass priors for cosmology from random matrices". In: *Physical Review D* 97.4. ISSN: 2470-0029. DOI: 10.1103/physrevd.97.043510. URL: http://dx.doi.org/10.1103/PhysRevD.97.043510.

Lorenz, Christiane S., David Alonso, and Pedro G. Ferreira (2018). "Impact of relativistic effects on cosmological parameter estimation". In: *Phys. Rev.* D97.2, p. 023537. DOI: 10.1103/PhysRevD.97.023537. arXiv: 1710.02477 [astro-ph.CO].

LoVerde, Marilena (2014). "Halo bias in mixed dark matter cosmologies". In: *Phys. Rev. D* 90 (8), p. 083530. DOI: 10.1103/PhysRevD.90.083530. URL: https://link.aps.org/doi/10.1103/PhysRevD.90.083530.

— (2016). "Neutrino mass without cosmic variance". In: *Phys. Rev. D* 93 (10), p. 103526. DOI: 10.1103/PhysRevD.93.103526. URL: https://link.aps.org/doi/10.1103/PhysRevD.93.103526.

LoVerde, Marilena and Niayesh Afshordi (2008). "Extended Limber Approximation". In: *Phys. Rev.* D78, p. 123506. DOI: 10.1103/PhysRevD.78.123506. arXiv: 0809.5112 [astro-ph].

LSST Science Collaboration et al. (Dec. 2009). "LSST Science Book, Version 2.0". In: *arXiv e-prints*, arXiv:0912.0201, arXiv:0912.0201. arXiv: 0912.0201 [astro-ph.IM].

Ma, Zhao-Ming, Wayne Hu, and Dragan Huterer (2005). "Effect of photometric redshift uncertainties on weak lensing tomography". In: *Astrophys. J.* 636, pp. 21–29. DOI: 10.1086/497068. arXiv: astro-ph/0506614 [astro-ph].

Maartens, Roy et al. (2015). "Overview of Cosmology with the SKA". In: *PoS* AASKA14, p. 016. DOI: 10.22323/1.215.0016. arXiv: 1501.04076 [astro-ph.CO].

Makarov, Alexey et al. (June 2007). "The clustering of luminous red galaxies in the Sloan Digital Sky Survey imaging data". In: *Monthly Notices of the Royal Astronomical Society* 378.3, pp. 852–872. ISSN: 0035-8711. DOI: 10.1111/j.1365-2966.2007.11593.x. eprint: http://oup.prod.sis.lan/mnras/article-pdf/378/3/852/18665637/mnras0378-0852.pdf. URL: https://dx.doi.org/10.1111/j.1365-2966.2007.11593.x.

Mandelbaum, Rachel et al. (2013). "Cosmological parameter constraints from galaxy-galaxy lensing and galaxy clustering with the SDSS DR7". In: *Mon. Not. Roy. Astron. Soc.* 432, p. 1544. DOI: 10.1093/mnras/stt572. arXiv: 1207.1120 [astro-ph.CO].

Marinoni, C., J. Bel, and A. Buzzi (2012). "The Scale of Cosmic Isotropy". In: *JCAP* 10, p. 036. DOI: 10.1088/1475-7516/2012/10/036. arXiv: 1205.3309 [astro-ph.CO].

Mather, John C. et al. (1994). "Measurement of the Cosmic Microwave Background spectrum by the COBE FIRAS instrument". In: *Astrophys. J.* 420, pp. 439–444. DOI: 10.1086/173574.

McAlpine, Kim et al. (2012). "The Likelihood Ratio as a tool for Radio Continuum Surveys with SKA precursor telescopes". In: *ArXiv e-prints*. arXiv: 1202.1958 [astro-ph.IM].

McDonald, Patrick and Uroš Seljak (2009a). "How to evade the sample variance limit on measurements of redshift-space distortions". In: *Journal of Cosmology and Astroparticle Physics* 2009.10, pp. 007–007. DOI: 10.1088/1475-7516/2009/10/007. URL: https://doi.org/10.1088%2F1475-7516%2F2009%2F10%2F007.

McDonald, Patrick and Uros Seljak (2009b). "How to measure redshift-space distortions without sample variance". In: *JCAP* 0910, p. 007. DOI: 10.1088/1475-7516/2009/10/007. arXiv: 0810.0323 [astro-ph].

Ménard, Brice et al. (2013). "Clustering-based redshift estimation: method and application to data". In: *ArXiv e-prints*. arXiv: 1303.4722 [astro-ph.CO].

Milgrom, Mordehai (2015). "MOND theory". In: *Can. J. Phys.* 93.2, pp. 107–118. DOI: 10.1139/cjp-2014-0211. arXiv: 1404.7661 [astro-ph.CO].

Ménard, Brice et al. (June 2010). "Measuring the galaxy–mass and galaxy–dust correlations through magnification and reddening". In: *Monthly Notices of the Royal Astronomical Society* 405.2, pp. 1025–1039. ISSN: 0035-8711. DOI: 10.1111/j.1365-2966.2010.16486.x. eprint: http://oup.prod.sis.lan/mnras/article-pdf/405/2/1025/4001735/mnras0405-1025.pdf. URL: https://doi.org/10.1111/j.1365-2966.2010.16486.x.

Nicola, Andrina, Alexandre Refregier, and Adam Amara (2016). "Integrated approach to cosmology: Combining CMB, large-scale structure and weak lensing". In: *Phys. Rev.* D94.8, p. 083517. DOI: 10.1103/PhysRevD.94.083517. arXiv: 1607.01014 [astro-ph.CO].

Nolta, M. R. et al. (2004). "First YearWilkinson Microwave Anisotropy ProbeObservations: Dark Energy Induced Correlation with Radio Sources". In: *The Astrophysical Journal* 608.1, pp. 10–15. DOI: 10.1086/386536. URL: https://doi.org/10.1086%2F386536.

Norris, Ray P. et al. (2011). "EMU: Evolutionary Map of the Universe". In: *Publications of the Astronomical Society of Australia* 28.3, 215–248. DOI: 10.1071/AS11021.

Ntelis, Pierros et al. (2017). "Exploring cosmic homogeneity with the BOSS DR12 galaxy sample". In: *JCAP* 06, p. 019. DOI: 10.1088/1475-7516/2017/06/019. arXiv: 1702.02159 [astro-ph.CO].

Nusser, Adi and Prabhakar Tiwari (2015). "THE CLUSTERING OF RADIO GALAXIES: BIASING AND EVOLUTION VERSUS STELLAR MASS". In: *The Astrophysical Journal* 812.1, p. 85. DOI: 10.1088/0004-637x/812/1/85. URL: https://doi.org/10.1088%2F0004-637x%2F812%2F1%2F85.

Overzier, R. A. et al. (2003). "The spatial clustering of radio sources in NVSS and FIRST; implications for galaxy clustering evolution". In: *A&A* 405.1, pp. 53–72. DOI: 10.1051/0004-6361:20030527. URL: https://doi.org/10.1051/0004-6361:20030527.

Peebles, P. J. E. (1980). *The large-scale structure of the universe / by P. J. E. Peebles*. English. Princeton University Press Princeton, N.J, xiii, 422 p. : ISBN: 0691082405 0691082391.

Perlmutter, S. et al. (1998). "Discovery of a supernova explosion at half the age of the Universe". In: *Nature* 391.6662, 51–54. ISSN: 1476-4687. DOI: 10.1038/34124. URL: http://dx.doi.org/10.1038/34124.

Planck Collaboration et al. (2016). "Planck 2015 results - XXI. The integrated Sachs-Wolfe effect". In: *A&A* 594, A21. DOI: 10.1051/0004-6361/201525831. URL: https://doi.org/10.1051/0004-6361/201525831.

Pourtsidou, Alkistis and Thomas Tram (2016). "Reconciling CMB and structure growth measurements with dark energy interactions". In: *Phys. Rev.* D94.4, p. 043518. DOI: 10.1103/PhysRevD.94.043518. arXiv: 1604.04222 [astro-ph.CO].

Raccanelli, A. et al. (Apr. 2008). "A reassessment of the evidence of the Integrated Sachs–Wolfe effect through the WMAP–NVSS correlation". In: *Monthly Notices of the Royal Astronomical Society* 386.4, pp. 2161–2166. ISSN: 0035-8711. DOI: 10.1111/j.1365-2966.2008.13189.x. eprint: http://oup.prod.sis.lan/mnras/article-pdf/386/4/2161/4277788/mnras0386-2161.pdf. URL: https://doi.org/10.1111/j.1365-2966.2008.13189.x.

Raccanelli, Alvise et al. (Aug. 2012). "Cosmological measurements with forthcoming radio continuum surveys". In: *Monthly Notices of the Royal Astronomical Society* 424.2, pp. 801–819. ISSN: 0035-8711. DOI: 10.1111/j.1365-2966.2012.20634.x. eprint: http://oup.prod.sis.lan/mnras/article-pdf/424/2/801/3227638/424-2-801.pdf. URL: https://doi.org/10.1111/j.1365-2966.2012.20634.x.

Raccanelli, Alvise et al. (Sept. 2013). "Testing gravity using large-scale redshift-space distortions". In: *Monthly Notices of the Royal Astronomical Society* 436.1, pp. 89–100. ISSN: 0035-8711. DOI: 10.1093/mnras/stt1517. eprint: https://academic.oup.com/mnras/article-pdf/436/1/89/18500262/stt1517.pdf. URL: https://doi.org/10.1093/mnras/stt1517.

Raccanelli, Alvise et al. (2015). "Probing primordial non-Gaussianity via iSW measurements with SKA continuum surveys". In: *Journal of Cosmology and Astroparticle Physics* 2015.01, pp. 042–042. DOI: 10.1088/1475-7516/2015/01/042. URL: https://doi.org/10.1088%2F1475-7516%2F2015%2F01%2F042.

Raveri, Marco (2016). "Are cosmological data sets consistent with each other within the Λ cold dark matter model?" In: *Phys. Rev.* D93.4, p. 043522. DOI: 10.1103/PhysRevD.93.043522. arXiv: 1510.00688 [astro-ph.CO].

Riess, Adam G. et al. (1998). "Observational Evidence from Supernovae for an Accelerating Universe and a Cosmological Constant". In: *The Astronomical Journal* 116.3, pp. 1009–1038. DOI: 10.1086/300499. URL: https://doi.org/10.1086%2F300499.

Ross, Ashley J., Will J. Percival, and Kelly Nock (Aug. 2010). "The effect of redshift-space distortions on projected two-point clustering measurements". In: *Monthly Notices of the Royal Astronomical Society* 407.1, pp. 520–532. ISSN: 0035-8711. DOI: 10.1111/j.1365-2966.2010.16927.x. eprint: http://oup.prod.sis.lan/mnras/article-pdf/407/1/520/3086640/mnras0407-0520.pdf. URL: https://dx.doi.org/10.1111/j.1365-2966.2010.16927.x.

Rubart, M. and Schwarz, D. J. (2013). "Cosmic radio dipole from NVSS and WENSS". In: *A&A* 555, A117. DOI: 10.1051/0004-6361/201321215. URL: https://doi.org/10.1051/0004-6361/201321215.

Salas, Pablo F. de et al. (2018a). "Neutrino Mass Ordering from Oscillations and Beyond: 2018 Status and Future Prospects". In: *Frontiers in Astronomy and Space Sciences* 5. ISSN: 2296-987X. DOI: 10.3389/fspas.2018.00036. URL: http://dx.doi.org/10.3389/fspas.2018.00036.

Salas, P.F. de et al. (2018b). "Status of neutrino oscillations 2018: 3sigma hint for normal mass ordering and improved CP sensitivity". In: *Physics Letters B* 782,

pp. 633 –640. ISSN: 0370-2693. DOI: https://doi.org/10.1016/j.physletb.2018.06.019. URL: http://www.sciencedirect.com/science/article/pii/S0370269318304672.

Sarkar, Prakash et al. (2009). "The scale of homogeneity of the galaxy distribution in SDSS DR6". In: *Mon. Not. Roy. Astron. Soc.* 399, pp. L128–L131. DOI: 10.1111/j.1745-3933.2009.00738.x. arXiv: 0906.3431 [astro-ph.CO].

Scelfo, Giulio et al. (2018). "GWLSS: chasing the progenitors of merging binary black holes". In: *Journal of Cosmology and Astroparticle Physics* 2018.09, pp. 039–039. DOI: 10.1088/1475-7516/2018/09/039. URL: https://doi.org/10.10882F1475-7516\%2F2018\%2F09\%2F039.

Scharf, Caleb A., Karl B. Fisher, and Ofer Lahav (Jan. 1994). "A spherical harmonic approach to redshift distortion and a measurement of

*Omega*_0

from the 1.2-Jy IRAS Redshift Survey". In: *Monthly Notices of the Royal Astronomical Society* 266.1, pp. 219–226. ISSN: 0035-8711. DOI: 10.1093/mnras/266.1.219. eprint: http://oup.prod.sis.lan/mnras/article-pdf/266/1/219/3577471/mnras266-0219.pdf. URL: https://dx.doi.org/10.1093/mnras/266.1.219.

Scranton, Ryan et al. (2005). "Detection of Cosmic Magnification with the Sloan Digital Sky Survey". In: *The Astrophysical Journal* 633.2, pp. 589–602. DOI: 10.1086/431358. URL: https://doi.org/10.1086%2F431358.

Seljak, Uro š (2009). "Extracting Primordial Non-Gaussianity without Cosmic Variance". In: *Phys. Rev. Lett.* 102 (2), p. 021302. DOI: 10.1103/PhysRevLett.102.021302. URL: https://link.aps.org/doi/10.1103/PhysRevLett.102.021302.

Simpson, Fergus et al. (2017). "Strong Bayesian evidence for the normal neutrino hierarchy". In: *Journal of Cosmology and Astroparticle Physics* 2017.06, 029–029. ISSN: 1475-7516. DOI: 10.1088/1475-7516/2017/06/029. URL: http://dx.doi.org/10.1088/1475-7516/2017/06/029.

Singh, Sukhdeep, Rachel Mandelbaum, and Joel R. Brownstein (2017). "Cross-correlating Planck CMB lensing with SDSS: Lensing-lensing and galaxy-lensing cross-correlations". In: *Mon. Not. Roy. Astron. Soc.* 464.2, pp. 2120–2138. DOI: 10.1093/mnras/stw2482. arXiv: 1606.08841 [astro-ph.CO].

Smith, Kendrick M., Oliver Zahn, and Olivier Doré (2007). "Detection of gravitational lensing in the cosmic microwave background". In: *Phys. Rev. D* 76 (4), p. 043510. DOI: 10.1103/PhysRevD.76.043510. URL: https://link.aps.org/doi/10.1103/PhysRevD.76.043510.

Song, Yong-Seon and Will J Percival (2009). "Reconstructing the history of structure formation using redshift distortions". In: *Journal of Cosmology and Astroparticle Physics* 2009.10, pp. 004–004. DOI: 10.1088/1475-7516/2009/10/004. URL: https://doi.org/10.1088%2F1475-7516%2F2009%2F10%2F004.

Spergel, David N., Raphael Flauger, and Renée Hložek (2015). "Planck Data Reconsidered". In: *Phys. Rev.* D91.2, p. 023518. DOI: 10.1103/PhysRevD.91.023518. arXiv: 1312.3313 [astro-ph.CO].

Szalay, Alexander S., Takahiko Matsubara, and Stephen D. Landy (1998). "Redshift-Space Distortions of the Correlation Function in Wide-Angle Galaxy Surveys". In: *The Astrophysical Journal* 498.1, pp. L1–L4. DOI: 10.1086/311293. URL: https://doi.org/10.1086%2F311293.

Sánchez, Ariel G. et al. (Sept. 2012). "The clustering of galaxies in the SDSS-III Baryon Oscillation Spectroscopic Survey: cosmological implications of the large-scale two-point correlation function". In: *Monthly Notices of the Royal Astronomical Society* 425.1, pp. 415–437. ISSN: 0035-8711. DOI: 10.1111/j.1365-2966.2012.21502.x. eprint: https://academic.oup.com/mnras/article-pdf/425/1/415/3201657/425-1-415.pdf. URL: https://doi.org/10.1111/j.1365-2966.2012.21502.x.

Tegmark, Max, Andy Taylor, and Alan Heavens (1997). "Karhunen-Loeve eigenvalue problems in cosmology: How should we tackle large data sets?" In: *Astrophys. J.* 480, p. 22. DOI: 10.1086/303939. arXiv: astro-ph/9603021 [astro-ph].

The Planck Collaboration (Apr. 2006). "The Scientific Programme of Planck". In: *arXiv e-prints*, astro-ph/0604069, astro–ph/0604069. arXiv: astro-ph/0604069 [astro-ph].

Thiele, Leander, Christopher A. J. Duncan, and David Alonso (2019). "Disentangling magnification in combined shear-clustering analyses". In: *ArXiv e-prints*. arXiv: 1907.13205 [astro-ph.CO].

Thomas, Brian C. et al. (2004). "Quantifying the Bull's-Eye Effect". In: *The Astrophysical Journal* 601.1, pp. 28–36. DOI: 10.1086/380434. URL: https://doi.org/10.1086%2F380434.

Upadhye, Amol et al. (2016). "Redshift-space distortions in massive neutrino and evolving dark energy cosmologies". In: *Phys. Rev. D* 93 (6), p. 063515. DOI: 10.1103/PhysRevD.93.063515. URL: https://link.aps.org/doi/10.1103/PhysRevD.93.063515.

Vagnozzi, Sunny et al. (2017). "Unveiling nu secrets with cosmological data: Neutrino masses and mass hierarchy". In: *Physical Review D* 96.12. ISSN: 2470-0029. DOI: 10.1103/physrevd.96.123503. URL: http://dx.doi.org/10.1103/PhysRevD.96.123503.

Vagnozzi, Sunny et al. (2018). "Bias due to neutrinos must not uncorrect'd go". In: *Journal of Cosmology and Astroparticle Physics* 2018.09, pp. 001–001. DOI: 10.1088/1475-7516/2018/09/001. URL: https://doi.org/10.1088%2F1475-7516%2F2018%2F09%2F001.

Van Waerbeke, L. (2010). "Shear and Magnification: Cosmic Complementarity". In: *Mon. Not. Roy. Astron. Soc.* 401, p. 2093. DOI: 10.1111/j.1365-2966.2009.15809.x. arXiv: 0906.1583 [astro-ph.CO].

Vanessa Böhm, Chirag Modi and Emanuele Castorina (2019). "Lensing corrections on galaxy-lensing cross correlations and galaxy-galaxy auto correlations". In: *ArXiv e-prints*. arXiv: 1910.06722 [astro-ph.CO].

Verlinde, Erik P. (2011). "On the Origin of Gravity and the Laws of Newton". In: *JHEP* 04, p. 029. DOI: 10.1007/JHEP04(2011)029. arXiv: 1001.0785 [hep-th].

Villa, Eleonora, Enea Di Dio, and Francesca Lepori (2018). "Lensing convergence in galaxy clustering in ?CDM and beyond". In: *JCAP* 1804.04, p. 033. DOI: 10.1088/1475-7516/2018/04/033. arXiv: 1711.07466 [astro-ph.CO].

Wald, Robert M. (1984). *General Relativity*. Chicago, USA: Chicago Univ. Pr. DOI: 10.7208/chicago/9780226870373.001.0001.

Weinberg, David H. et al. (2013). "Observational Probes of Cosmic Acceleration". In: *Phys. Rept.* 530, pp. 87–255. DOI: 10.1016/j.physrep.2013.05.001. arXiv: 1201.2434 [astro-ph.CO].

Witzemann, Amadeus et al. (2019). "Simulated multitracer analyses with H i intensity mapping". In: *Mon. Not. Roy. Astron. Soc.* 485.4, pp. 5519–5531. DOI: 10.1093/mnras/stz778. arXiv: 1808.03093 [astro-ph.CO].

Xia, Jun-Qing et al. (Sept. 2011). "A cross-correlation study of the Fermi-LAT gamma-ray diffuse extragalactic signal". In: *Monthly Notices of the Royal Astronomical Society* 416.3, pp. 2247–2264. ISSN: 0035-8711. DOI: 10.1111/j.1365-2966.2011.19200.x. eprint: http://oup.prod.sis.lan/mnras/article-pdf/416/3/2247/2861634/mnras0416-2247.pdf. URL: https://doi.org/10.1111/j.1365-2966.2011.19200.x.

Yahya, S. et al. (2015). "Cosmological performance of SKA HI galaxy surveys". In: *Mon. Not. Roy. Astron. Soc.* 450.3, pp. 2251–2260. DOI: 10.1093/mnras/stv695. arXiv: 1412.4700 [astro-ph.CO].

Yoo, Jaiyul (2010). "General Relativistic Description of the Observed Galaxy Power Spectrum: Do We Understand What We Measure?" In: *Phys. Rev.* D82, p. 083508. DOI: 10.1103/PhysRevD.82.083508. arXiv: 1009.3021 [astro-ph.CO].

Yoo, Jaiyul and Uros Seljak (2012). "Joint Analysis of Gravitational Lensing, Clustering and Abundance: Toward the Unification of Large-Scale Structure Analysis". In: *Phys. Rev.* D86, p. 083504. DOI: 10.1103/PhysRevD.86.083504. arXiv: 1207.2471 [astro-ph.CO].

Zhao, Gong-Bo et al. (2010). "Probing modifications of General Relativity using current cosmological observations". In: *Phys. Rev.* D81, p. 103510. DOI: 10.1103/PhysRevD.81.103510. arXiv: 1003.0001 [astro-ph.CO].

Zuntz, Joe et al. (2015). "CosmoSIS: modular cosmological parameter estimation". In: *Astron. Comput.* 12, pp. 45–59. DOI: 10.1016/j.ascom.2015.05.005. arXiv: 1409.3409 [astro-ph.CO].